



GEOFORSCHUNGSZENTRUM POTSDAM
STIFTUNG DES ÖFFENTLICHEN RECHTS

Scientific Technical Report

ISSN 1610-0956

DISS. ETH No. 15265, 2003

Engineering geological rock mass characterisation of granitic gneisses based on seismic in-situ measurements

A dissertation submitted to the
SWISS FEDERAL INSTITUTE OF TECHNOLOGY ZURICH
for the degree of
Doctor of Sciences

presented by
Christian Klose
Diplom-Geologe
born 4. November 1974
citizen of Germany

Prof. Dr. Simon Löw (ETH Zürich), examiner
Prof. Dr. Günter Borm (GFZ Potsdam), co-examiner
Dr. Hansruedi Maurer (ETH Zürich), co-examiner

To my parents.

Zwei Dinge sollen Kinder
von ihren Eltern bekommen:
Wurzeln und Flügel.

J. W. v. Goethe

Acknowledgments

I would like to express my deepest and sincere appreciation to my thesis advisors Prof. Simon Löw and Prof. Günter Borm. Without their continuous support, guidance, and patience throughout the 44 months in Potsdam and Zürich, this work would have been impossible.

Especially I am obliged to my colleagues at GFZ Potsdam, Dr. Rüdiger Giese, Peter Otto, Silvio Mielitz, Bernd Maushake and Christian Selke for their endless efforts performing seismic measurements of excellent quality under dangerous conditions in the Faido tunnel.

I am grateful to Dr. Hansruedi Maurer and Prof. Wolfgang Rabbel for their helpful suggestions, their advice, and for sharing their excellent knowledge on tomographic imaging and shear-wave splitting.

I am greatly indebted to Dr. Corrado Fidelibus, Dr. Rüdiger Giese, Marcel Naumann, Dr. Christiane Trela, Dr. Nathalie Van Meir, Dr. Andrew Kos, Dr. Christian Zangerl, Dr. Keith Evans, Dr. Erik Eberhardt, Dr. Kurosch Thuro, Prof. Michael Alber and Prof. Ove Stephansson for their fruitful discussions, their support, and their efforts to improve my style writing English.

Special thank goes to Birgit Schöbel for her help to improve my figures in my thesis, to Katrin Wiczorek for her help to extract the shear-wave data from the seismograms, and to Dr. Till Popp who provided the results of the laboratory measurements. I thank Amberg AG and Rinaldo Volpers for their help providing me with geological data of the Faido tunnel. Last but not least, I am thankful to GFZ Potsdam and ETH Zürich for their financial support.

Contents

Summary	xv
Zusammenfassung	xvii
1 Introduction	1
1.1 Motivation	1
1.2 Overview of current literature	1
1.3 Thesis organisation	2
1.4 Field and laboratory investigations	3
2 Determination of fracture set and fabric orientations in granitic gneisses by characterising S_1-wave polarisation ellipsoids	7
2.1 Introduction and objectives	8
2.2 Shear-wave particle motion	10
2.3 Geological settings	16
2.4 Seismic data acquisition	26
2.4.1 Overview	26
2.4.2 Laboratory measurements	26
2.4.3 In-situ measurements	27
2.5 Discussion and conclusion	43
3 Classification by conventional methods	49
3.1 Introduction and objectives	50
3.2 Geology of the Faido tunnel	52
3.2.1 Overview	52

3.2.2	Geological rock mass properties	55
3.3	Seismic data acquisition	60
3.3.1	Seismic in-situ measurements	60
3.3.2	Seismic data processing	61
3.4	Relationships between geological and seismic rock mass properties	66
3.4.1	Total fracture spacing s_t	66
3.4.2	Uniaxial compressive strength σ_c	67
3.4.3	Fracture persistence p and aperture e	67
3.4.4	Schistosity dipping ss	67
3.4.5	Seismic velocities v_P and v_S	76
3.4.6	Poisson's ratio ν	76
3.4.7	Shear-wave anisotropy ξ	76
3.4.8	Shape measure S and shape intensity I of the S_1 -wave polarisation ellipsoids	77
3.5	Conclusion	80
4	Classification by Self-Organising Maps SOM	83
4.1	Introduction and objectives	84
4.2	Data acquisition	85
4.2.1	Acquisition of the seismic data	85
4.2.2	Acquisition of the geological data	85
4.3	Self-Organising maps	86
4.3.1	Theoretical background	86
4.3.2	SOM interpretation	89
4.4	Observations	91
4.4.1	Characterisation of rock mass properties	91
4.4.2	Characterisation of homogeneous rock mass units	98
4.5	Discussion and conclusion	103
5	Final Conclusions	107

6	References	109
A	A New Clustering Method for Partitioning Directional Data	113
A.1	Abstract	114
A.2	Introduction	114
A.3	Clustering of Directional Data	116
A.3.1	Derivation of the Clustering Method	116
A.3.2	Summary of the Clustering Algorithm	119
A.4	Results	120
A.5	Conclusion	122
A.6	Appendix	123
B	Seismic Tomograms	125

List of Figures

2.1	Polarisation phenomenon in structural anisotropic rock with respect to different propagation directions of the S -waves	9
2.2	Illustration of the orientation of the ellipsoid, which is defined by the direction of its largest axe λ_1	11
2.3	Transformation functions to describe the ratio between two polarisation ellipsoid axes	12
2.4	Flattening-stretching diagram to classify the S_1 -wave polarisation.	13
2.5	2-class separation of a probability distribution of a real world example by a linear discriminant function	14
2.6	Quality and reliability of the polarisation ellipsoid	15
2.7	Geographical and geological overview of the Faido tunnel in southern Switzerland	17
2.8	Geological situation along the seismic profile between 881 - 963 m	19
2.9	Geological situation along the seismic profile between 1130 - 1215 m	20
2.10	Geological situation along the seismic profile between 1314 - 1379 m	21
2.11	Geological situation along the seismic profile between 1582 - 1663 m	22
2.12	Geological situation along the seismic profile between 1858 - 1920 m	23
2.13	Geological situation along the seismic profile between 2132 - 2205 m	24
2.14	Geological situation along the seismic profile between 2360 - 2433 m	25
2.15	Shear-wave velocity anisotropies ξ of gneiss rock samples as function of the confining pressure	26
2.16	Schematic illustration of the installed geophysical measurement units and of the tomogram within the tunnel	27
2.17	Example of a seismogram and 3-d particle displacement	28
2.18	Polarisation ellipsoids of the S_1 -waves at tunnel meter 881-963 m	30
2.19	Polarisation ellipsoids of the S_1 -waves at tunnel meter 1130-1215 m	32

2.20	Polarisation ellipsoids of the S_1 -waves at tunnel meter 1314-1379 m . . .	34
2.21	Polarisation ellipsoids of the S_1 -waves at tunnel meter 1582-1663 m . . .	36
2.22	Polarisation ellipsoids of the S_1 -waves at tunnel meter 1858-1942 m . . .	38
2.23	Polarisation ellipsoids of the S_1 -waves at tunnel meter 2132-2205 m . . .	40
2.24	Polarisation ellipsoids of the S_1 -waves at tunnel meter 2360-2433 m . . .	42
2.25	Distribution of the MAs mean shape parameters of the S_1 -waves, measured along the seven seismic profiles in the Faido tunnel	45
2.26	Relations between the total fracture spacing and the mean shape intensities	46
3.1	Geological rock mass properties along the Faido tunnel	58
3.2	Procedure to generate the seismic tomograms	61
3.3	Velocity values around the tunnel and the EDZ	62
3.4	Seismic rock mass properties along the Faido tunnel	65
3.5	Correlations between σ_c and the seismic rock mass features	68
3.6	Correlations between Q and the seismic rock mass features	69
3.7	Correlations between s_t and the seismic rock mass features	70
3.8	Correlations between p and the seismic rock mass features	71
3.9	Correlations between e and the seismic rock mass features	72
3.10	Correlations between r and the seismic rock mass features	73
3.11	Correlations between f and the seismic rock mass features	74
3.12	Correlations between ss and the seismic rock mass features	75
3.13	Geological and seismic detail information along the tunnel profile between 881 - 963 m	78
3.14	Geological and seismic detail information along the tunnel profile between 881 - 963 m	79
4.1	Structure of a SOM neural network	87
4.2	Why is the Poisson's ratio important for classifications?	89
4.3	Classification scheme of a SOM neural network	90
4.4	SOM-classification results based on profile locations	92
4.5	Density kernels and classes of the seismic properties	93

4.6	Density kernels and classes of the geological properties	94
4.7	SOM-classification based on seismic feature classes	95
4.8	SOM-classification based on geological feature classes	97
4.9	Separation quality of the 9 seismic-geological clusters	99
4.10	Seismic-geological clusters along the Faido tunnel	100
4.11	SOM-classification based on seismic-geological feature clusters	101
4.12	Uncertainty map of a SOM-classification	102
A.1	Definition of a fracture orientation	117
A.2	An example of fracture orientations	121

List of Tables

2.1	Mean orientations of the S_1 -wave polarisation ellipsoids and the related geological rock mass structures at tunnel meter 881-963 m	31
2.2	Mean orientations of the S_1 -wave polarisation ellipsoids and the related geological rock mass structures at tunnel meter 1130-1215 m	33
2.3	Mean orientations of the S_1 -wave polarisation ellipsoids and the related geological rock mass structures at tunnel meter 1314-1379 m	35
2.4	Mean orientations of the S_1 -wave polarisation ellipsoids and the related geological rock mass structures at tunnel meter 1582-1663 m	37
2.5	Mean orientations of the S_1 -wave polarisation ellipsoids and the related geological rock mass structures at tunnel meter 1858-1942 m	39
2.6	Mean orientations of the S_1 -wave polarisation ellipsoids and the related geological rock mass structures at tunnel meter 2132-2205 m	41
2.7	Mean orientations of the S_1 -wave polarisation ellipsoids and the related geological rock mass structures at tunnel meter 2360-2433 m	43
3.1	Fracture families in the Leventina and Lucomagno gneisses	54
3.2	Empirical standard errors of the seismic properties	63
4.1	Homogeneous seismic-geological rock mass units	100
A.1	Clustering results of the Pecher algorithm	121
A.2	Clustering results of the new algorithm	122

Abbreviations and Symbols

v_P	velocity of the compression-waves
v_S	velocity of the leading shear-waves
S_1	leading shear-waves
S_2	velocity of the second shear-waves
ν	(dyn.) Poisson's ratio
ξ	shear-wave anisotropy
S	shape measure of the polarisation ellipsoid of the leading shear-wave
$S^{discr.}$	discriminant function between two classes in S
I	shape intensity of the polarisation ellipsoid of the leading shear-wave
$\lambda_{1,2,3}$	eigenvectors of a polarisation ellipsoid
$\hat{\lambda}_{1,2,3}$	eigenvectors in the unit sphere
z	ray path density of the seismic waves within a defined grid of a tomogram
U	uncertainty
e	fracture aperture
f	fracture infilling
f_3	fracture family No. 3
p	fracture persistence
Q	water inflow into the tunnel
r	fracture roughness
$s(f_3)$	fracture spacing of fracture family No. 3
s_t	total fracture spacing
ss_1	early schistosity
ss_2	late schistosity
σ_c	uniaxial compression strength
α	dip direction of a plane or line with $0^\circ \leq \alpha \leq 360^\circ$
θ	dip angle of a plane or line with $0^\circ \leq \theta \leq 90^\circ$
$\vec{\Theta}$	orientation vector with $\vec{\Theta} = \{\alpha, \theta\}$

a	average dissimilarity
b	smallest dissimilarity
x	scalar x
\vec{x}	vector x
\vec{x}^T	transposed of vector x
$\ \vec{x} - \vec{w}\ $	Euclidean distance between \vec{x} and \vec{w}
$Corr$	correlation coefficient
d	dissimilarity
R^2	squared residual of a fit function (R^2 regression test)
χ^2	squared errors of a fit function (χ^2 regression test)
$s(i)$	silhouette width of observation i
Δ	statistical standard error
E	geographic East
EDA	Extensive Dilatancy Anisotropy
EDZ	Excavation Disturbed Zone
FA	fold axis
h.	high
l.	low
LeG	Leventina gneiss
LuG	Lucomagno gneiss
max	maximum
MA	Mixture of Anisotropies
min	minimum
N	geographic North
NE	geographic North East
NEAT	N eue A lpen T ransversale (English: New Alp Transversal)
S	geographic South
SOM	Self-Organising Maps
SW	geographic South West
v.h.	very high
v.l.	very low
W	geographic West

Summary

For deep underground excavations, the prediction of locations of small-scale geotechnical hazardous structures such as faults is nearly impossible when exploration is restricted to surface based methods. Therefore, for many base tunnels, exploration ahead of the advancing tunnel face is an essential component of the excavation plan. This PhD thesis aims at improving the technology for geological interpretations of seismic data, collected in underground excavations. For that purpose GeoForschungsZentrum Potsdam carried out a series of seismic measurements along the 2600 m long and up to 1400 m deep Faido access tunnel, an adit to the 57 km long Gotthard base tunnel in Switzerland.

Seismic rock mass properties were acquired from tomograms and seismograms measured along the tunnel wall. The geological features were derived from tunnel mapping. The goal is to find those seismic features like compression and shear wave velocities, dynamic Poisson's ratio, and shear-wave anisotropy and, additionally, shape measure and shape intensity of the polarisation ellipsoids of the leading shear-waves, which are significantly related to important engineering geological rock mass properties. Chapter 2 shows that it is possible to determine the orientations of fracture and fabric induced polarisation ellipsoids within a rock mass region from the two new properties, shape measure and intensity. The mean orientations of the different rock mass anisotropies are determined by a new developed clustering technique.

The clustering technique, which is outlined in appendix A, is the first mathematical self-consistent method for partitioning directional data in spherical statistics. Directional data are grouped into disjunct clusters. Simultaneously the average dip direction and the average dip angle are calculated for each group. The new algorithm is fast and no heuristics is used, because all calculation steps are based on the same objective function and the method does not require the calculation of a contour density plot.

All rock mass properties are statistically analysed by conventional methods (see chapter 3), like correlations and spatial profile descriptions. The complexity and the noise of the seismic in-situ data, their non-linear relations to the geology and the only qualitative measured geological data make interpretations, especially by conventional methods, difficult. In chapter 4 an alternative approach, called *Self-Organising Maps*, is used to classify and to interpret the seismic data. This method, which is based on neural information processing, aims at finding unknown relationships in the 14-dimensional and nonlinear seismic-geological feature space by self-organisation. The results of the SOM-classification are represented in a topological ordered fashion into 2-dimensional images of neurons. Hence, the feature maps can be visually described and

easily interpreted. The SOM technique shows better and more reliable classification results, because more seismic properties are jointly used to characterise the rock mass.

In summary, it is possible to classify engineering geological rock mass properties from in-situ seismic measurements with subject to the following facts: integral character of seismic waves and seismic dependency. The integral character of seismic waves shows that the extensions of small heterogeneities like single fracture sets can not be imaged in detail, when they are smaller than the seismic wave lengths. The seismic dependency describes that seismic properties dependent on the geology. During a classification independent geological properties are determined by dependent seismic properties. A logical reasoning from the dependent seismic properties to the geological properties can lead to ambiguous interpretations. For that reason it is necessary to use as much as possible seismic properties in combination for a classification.

Zusammenfassung

Für tiefliegende Untertagebauwerke ist die Vorhersage von Orten kleinskaliger geotechnisch gefährlicher Strukturen wie Störzonen nahezu unmöglich, wenn die Exploration nur auf Methoden von der Erdoberfläche aus beschränkt ist. Deshalb ist die Vorauserkundung vor der Ortsbrust ein grundlegender Bestandteil im Vortriebsplan für viele Gebirgstunnel. Diese Doktorarbeit zielt darauf ab die Technologie zur geologischen Interpretation seismischer Daten zu verbessern. Für diesen Zweck hat das GeoForschungsZentrum Potsdam eine Reihe von seismischen Messungen im 2600 m langen und bis zu 1400 m tief gelegenen Faido Zugangstunnel durchgeführt; ein Stollen zum 57 km langen Gotthard Basis Tunnel.

Die seismischen Gebirgseigenschaften wurden durch Tomogramme und Seismogramme entlang der Tunnelwandung erworben. Die geologischen Daten wurden aus Tunnelkartierungen abgeleitet. Das Ziel ist es jene seismischen Merkmale zu finden, wie Kompressionswellen- und Scherwellengeschwindigkeiten, dynamische Poisson Zahl und Scherwellen-Geschwindigkeitsanisotropie, und zusätzlich das Formmaß und die Formintensität der Polarisationsellipse der führenden Scherwellen, die zuverlässige Beziehungen mit wichtigen ingenieurgeologischen Gebirgseigenschaften zeigen. Kapitel 2 zeigt, dass es durch die neuen Parameter, Formmaß und Formintensität, möglich ist, die Orientierungen von Polarisationsellipsoiden zu bestimmen, die durch Klüfte bzw. das Gefüge gebildet wurden. Die mittleren Orientierungen der verschiedenen Gebirgsanisotropien werden durch ein neu entwickeltes Clustering-Verfahren bestimmt.

Das Clustering-Verfahren, das im Anhang A aufgeführt ist, ist die erste mathematisch selbst-konsistente Methode zur Partitionierung orientierter Daten in der sphärischen Statistik. Die orientierten Daten werden in disjunkte Cluster gruppiert. Gleichzeitig werden von jeder Gruppe die mittlere Fallrichtung und der mittlere Fallwinkel errechnet. Der neue Algorithmus ist schnell und bedarf keiner Heuristik, weil alle Rechenschritte auf einer objektiven Funktion beruhen und die Methode keine Kontur-Dichtedarstellung verlangt.

Alle Gebirgseigenschaften werden durch konventionelle Methoden (siehe Kapitel 3), wie Korrelationen und räumliche Profilvergleiche statistisch analysiert. Die Komplexität und das Rauschen der seismischen in-situ Daten, ihre nichtlinearen Beziehungen zur Geologie und die nur qualitativ gemessenen geologischen Daten machen Interpretationen, besonders für konventionelle Methoden, schwierig. In Kapitel 4 wird ein alternativer Klassifikationsansatz, *Selbst-organisierende Karten* (SOM), verwendet um die seismischen Daten zu klassifizieren und zu interpretieren. Diese Methode, die auf neuronaler Informationsverarbeitung beruht, versucht unbekannt Beziehungen

im 14-dimensionalen und nichtlinearen seismisch-geologischen Merkmalsraum durch Selbstorganisation zu finden. Die Ergebnisse der SOM-Klassifikation werden in einer topologisch geordneten Form in 2-dimensionalen Bildern aus Neuronen präsentiert. Die Merkmalskarten können somit visuell beschrieben und leicht interpretiert werden. Die SOM-Klassifikation zeigt bessere und zuverlässigere Ergebnisse, weil mehrere seismische Eigenschaften gemeinsam verwendet werden um das Gebirge zu charakterisieren.

Zusammenfassend kann gesagt werden, dass es möglich ist ingenieurgeologische Gebirgseigenschaften durch seismische in-situ Messungen zu klassifizieren, in Abhängigkeit der folgenden Fakten: integraler Charakter der seismischen Wellen und seismische Abhängigkeit. Der integrale Charakter der seismischen Wellen besagt, dass kleine Heterogenitäten, wie einzelne Kluffgruppen, nicht detailliert abgebildet werden können, wenn sie kleiner sind als die seismischen Wellenlängen. Die seismische Abhängigkeit besagt, dass die seismischen Eigenschaften von der Geologie abhängen. Während einer Klassifikation werden die unabhängigen geologischen Eigenschaften durch abhängige seismische Eigenschaften bestimmt. Das logische Schlussfolgern von den seismischen auf die geologischen Parameter kann zu mehrdeutigen Interpretationen führen. Aus diesem Grund ist es notwendig so viel wie möglich seismische Eigenschaften in Kombination für eine Klassifikation heranzuziehen.

1 Introduction

1.1 Motivation

Geological characterisation based on seismic measurements for the assistance of underground excavations is an engineering geological task that involves broad multidisciplinary expertise in geology, geoengineering and geophysics. The need of automated decision support systems for risk mitigation for underground excavations requires new techniques to process seismic and geological information for practical application. Engineering geology has been started to include new methods and algorithms of information technology to meet these necessities. This Ph.D. thesis is motivated to contribute improvements on the quality of engineering geological rock mass classifications based on seismic data interpretations. For that purpose GeoForschungsZentrum Potsdam carried out in-situ seismic measurements in the Fadio adit, an access tunnel to the Gotthard base tunnel in southern Switzerland.

1.2 Overview of current literature

Numerical models were developed to understand the seismic-geological relationships by imaging the real-world in an approximate fashion. Some models are used to calculate the seismic velocities (v_P , v_S) and the Poisson's ratio (ν) as a function of crack density parameters. Garbin and Knopoff (1973, 1975), O'Connell and Budiansky (1974), and Henyey and Pomphrey (1982) show self-consistent models of isotropic networks of dry and wet cracks. Crampin (1981), Hudson (1981), and Peacock and Hudson (1990) derived theories for seismic wave propagations in rocks with isotropic and anisotropic crack distributions.

The results of in-situ studies for the characterisation of crystalline rocks with seismic data are available in the literature. Section 3.1 of chapter 3 gives a brief overview about a few studies. Interpretations of seismic data are mostly based on v_P (Sjögren et al., 1979, Moos and Zoback, 1983 or Mooney and Ginzburg, 1986). Other studies take v_S and ν into account, like Barton and Zoback (1992) and Kuwahara et al. (1995). The shear-wave velocity anisotropy ξ can be used additionally for interpretations when seismic data of high quality can be acquired. Recently, it has been suggested that shear-wave anisotropy, caused by wave splitting and polarisation, is diagnostic for rock mass anisotropy. Generally, a primary shear-wave S propagates within an anisotropic region and splits into two polarised shear-waves with different velocities (Christensen, 1971 and Crampin, 1981). The two shear-waves, a leading S_1 -wave and slower S_2 -

wave, are polarised in mutually perpendicular planes. The S_1 -wave shows in most cases a motion direction parallel to the plane of structural anisotropy, like fractures or foliation, whereas the S_2 -wave is perpendicularly oriented to the S_1 -wave.

The shapes of the polarisation ellipsoids of the leading S_1 -waves are analysed in this thesis to determine different directions of rock mass anisotropies. These new introduced amplitude values, shape measure S and shape intensity I , describe the geometry of a polarisation ellipsoid. The ellipsoids are analysed to determine the directions of anisotropies. S and I are expressed by the natural logarithm of the aspect ratios between the ellipsoid axes lengths. The logarithm gives a better understanding of the ellipsoid shapes compared to the three currently used ellipticities. These shape parameters are based on the square root of the axes aspect ratios and are introduced by Samson (1973, 1977), Matsumura (1981) and Cllet and Dubesset (1988).

This thesis outlines a new classification approach, called Self-Organising Maps (SOM), that was developed by Teuvo Kohohnen (i.e. Kohonen, 2001). This powerful method is based on neural information processing and very useful for classification task where no prior knowledge is available.

1.3 Thesis organisation

The thesis consists of four articles. Chapter 2, 3, and 4 are being prepared for submission to international reviews. The three chapters are originated from the research results of the investigations in the Faido tunnel. The article in chapter 2 is self-consistent and can be read independently. The excellent data quality of the seismic investigations made it possible to take modified amplitude values of the leading shear-waves into account for the seismic data interpretation. These introduced amplitude values describe the geometry of a polarisation ellipsoid. Section 2.5 shows that the new shape parameters are helpful to determine different directions of rock mass anisotropies by separating different shape classes within a Mixture of Anisotropies (MA).

Chapter 3 and 4 are constitutive. Both articles describe different interpretation techniques to classify the geology in the Faido tunnel from seismic measurements. The drawback of seismic in-situ data is their complexity, their noise, and their non-linear relation to the geology. Several geological and technical parameters may be related to the noise. These parameters vary simultaneously under in-situ conditions and do not retain constant, like during laboratory experiments and theoretical modelling. In addition, if the geological measurements are less qualitative due to the observers subjectivity or the restriction of the measurement method, interpretations are difficult. Especially conventional methods, like correlations and spatial profile descriptions, lead to uncertain rock mass characterisations of poor quality and less overview. Chapter 3 discusses the seismic data interpretations by conventional methods. Anyhow, the advantage of in-situ data is that they show simultaneously the interdependencies among all measured seismic and geological properties. Chapter 4 shows, that it is possible to automatically classify engineering geological rock mass properties from in-situ seismic measurements. The classifications were performed by a new method, called

Self-Organising Maps (SOM). This method is based on neural information processing and is more powerful compared to conventional methods. The reason is, that all seismic features are jointly used for the classification.

The Appendix A shows an article about a new clustering algorithm of directional data in spherical statistics. The paper was independently developed and is already submitted. The grouping method was applied for the outlined analyses in chapter 2 to partition orientations of polarisation ellipsoids. The different anisotropy orientations are calculated by the new clustering technique.

1.4 Field and laboratory investigations

GeoForschungsZentrum Potsdam carried out seven seismic measurement campaigns along the Faido tunnel. The seismic profiles were realised during tunnel excavations along the adit nearly every second month between September 2000 and June 2001. Giese et al. (2003) gives an overview about the seismic investigations. The tomographic images were calculated by a commercial software package, called ProMAX. This work was done by Dr. Giese from GeoForschungsZentrum Potsdam. The analysed shear-wave trains to derive the new shape parameters and to determine the structural rock mass anisotropies were extracted by the student Katrin Wiczorek at GeoForschungsZentrum Potsdam. Dr. Till Popp provided the results of the laboratory measurements that are outlined in section 2.4.2.

The geological data were mostly semi-quantitatively acquired in the 2600 m long and up to 1400 m deep Faido tunnel. The adit is 12% inclined and has a radius of 5 m. Sections 2.3 of chapter 2 and 3.2 of chapter 3 give an overview about the tunnel location and describe the geological situation in the tunnel. Rinaldo Volpers, the tunnel geologist at the building site of the Faido adit, acquired most of the geological data. He generated sketches of the tunnel faces, called tunnel face maps. The distances of the tunnel locations of the face maps vary between 1 and 20 m. In regions with high rock mass qualities, the distances are larger than in regions with low qualities. The gneiss varieties and the water inflow Q into the tunnel were derived from these tunnel face maps. Other geological parameters were sampled along the left tunnel wall, like fracture spacing and the orientation of the schistosity (dip direction/dip).

The information of the gneiss varieties were used to determine the uniaxial compressive strength σ_c of the gneisses at the specific tunnel positions. σ_c -values measured perpendicular to the schistosity with ($71 \leq 144 \pm 45 \leq 209$) MPa are preferred for further calculations compared to those parallel to the schistosity with ($74 \leq 119 \pm 25 \leq 152$) MPa, because they have a much higher variability and hence contain more information on σ_c in general. Relationships between σ_c and the gneiss varieties were determined during the excavation of 'Piora' exploration tunnel (Schneider, 1997). Here, σ_c was measured as a function of the Leventina (LeG) and Lucomagno (LuG) gneiss varieties: laminated LeG (209 ± 17 MPa), augen-structured to porphyric LeG (114 ± 35 MPa), porphyric to schistic LeG (149 ± 70 MPa), schistic LeG (186 ± 41 MPa) and porphyric biotite-rich LuG (75 ± 20 MPa). The relations are used to estimate σ_c -values

of the rocks in the Faido tunnel as follows (see eq. 1.1). A σ_c -value at an observed location is the harmonic mean of the σ_c -value (defined as σ) of each gneiss variety l ($l = 1, 2, \dots, 5$) and its percentage of occurrence a_l (area in a face map) at this tunnel position:

$$\sigma_c = \frac{\sum_{l=1}^5 a_l \sigma_l}{\sum_{l=1}^5 a_l} \quad (1.1)$$

Thus, only approximated σ_c -values could be derived. For a qualitative rock mass characterisation they are good enough, because the σ_c -values vary slightly in similar gneiss varieties and strongly among different varieties (see section 3.2.2).

Additional information of the gneiss structure were acquired by the spatial orientation of the schistosity. The dip angle ss of the macroscopic schistosity was determined quantitatively along the left tunnel wall within homogeneous regions. Section 3.2 gives a detailed overview about the schistosity and its visualisation in the maps of the left tunnel wall.

The normal fracture spacings s of the three main fracture families within homogeneous regions were continuously determined along the left tunnel wall. But, the data of the fracture families is of less quality - the acquisition was done under in-situ conditions during the excavation process. The normal fracture spacings of each fracture families is used to calculate the total fracture spacing s_t (e.g. Priest, 1994) as follows:

$$s_t = \frac{1}{\sum_{k=1}^3 \frac{1}{s_k}} \quad (1.2)$$

where s_k is the spacing of fracture family $k = 1, 2, 3$, measured along the left segment of the tunnel (homogeneous region). $\frac{1}{s_k}$ describes the linear fracture frequency (e.g. Priest, 1994).

Additional fracture parameters like the fracture persistence p , aperture e , roughness r and infilling f were semi-quantitatively determined along the left tunnel wall. The quality of these parameters is very poor, because these parameters were later determined independently from s_t and the outcrop quality of the advanced tunnelling process was poor too. p is not the absolute length of a fracture, because the length can not be directly determined in a tunnel. In this thesis, p is defined as the average length of the traces (harmonic mean) of the three main fracture families with subject to the fracture frequency $\frac{1}{s_k}$. The average p -value describes a homogeneous region and is determined as follows:

$$p = \frac{\sum_{k=1}^3 p_k \frac{1}{s_k}}{\sum_{k=1}^3 \frac{1}{s_k}} \quad (1.3)$$

where p_k is the persistence of the fracture family $k = 1, 2, 3$ within the segment of the tunnel (homogeneous region) in which s_k is determined as well. The parameters e , r , and f are determined after the same scheme of eq. 1.3. These parameters have to be understood as very roughly approximated values, due to the fact that more detailed data of better quality were not available during the tunneling process. The fracture roughness r could be described by only 2 ("very rough" and "rough") of 5 possible classes ("very rough", "rough", "slightly rough", "smooth", "slickensided"). Two classes could also be determined for the fracture infilling f ("none" and "hard infilling

< 5mm”) of 5 possible classes (“none”, “hard infilling < 5mm”, “hard infilling > 5mm”, “soft infilling < 5mm”, “soft infilling > 5mm”). p , e , r and f can only be used as semi-quantitative properties of the rock mass along the Faido tunnel.

The water inflow Q into the tunnel was directly outlined in the tunnel face map descriptions and was used to determine homogeneous Q -regions. Q can be characterised by 5 classes “dry”, “damp”, “wet”, “dripping” and “flowing”. Only 2 classes (“dry” and “wet”) occurred along the left tunnel wall, whereas more classes were mapped along the rest of the Faido tunnel. For the characterisation of the parameters Q , p , e , r and f the same classes were used as in the characterisation scheme of Bieniawski (1989). Other systems can be used as well but would provide similar results.

In summary, due to the limitations outlined above, all geological properties used in this thesis should be interpreted only qualitatively to identify significant changes of the characteristics between different rock mass units. More information on the geology is given in section [2.3](#) and [3.2](#).

2 Determination of fracture set and fabric orientations in granitic gneisses by characterising S_1 -wave polarisation ellipsoids

Überall geht ein frühes Ahnen
dem späteren Wissen voraus.

(Alexander von Humboldt)

Klose, C.^(1,2), Giese, R.⁽¹⁾, Loew, S.⁽²⁾, Borm, G.⁽¹⁾

⁽¹⁾ GFZ Potsdam, Geoen지니어ing, Telegrafenberg, 14473 Potsdam, Germany

⁽²⁾ ETH Zürich, Chair of Engineering Geology, Hönggerberg, 8093 Zürich, Switzerland

Article in preparation for submission to
Journal of Applied Geophysics

2.1 Introduction and objectives

Shear-wave polarisation is a natural phenomenon that occurs in structurally anisotropic media and can be observed within the upper crust. Recently, it has been suggested that shear-wave anisotropy, caused by wave splitting and polarisation, is diagnostic for rock mass anisotropy. Generally, a primary shear-wave S propagates within an anisotropic region and splits into two polarised shear-waves with different velocities (Christensen, 1971 and Crampin, 1981).

The two shear-waves, a leading S_1 -wave and slower S_2 -wave, are polarised in mutually perpendicular planes. The S_1 -wave shows in most cases a motion direction parallel to the plane of structural anisotropy, i.e. fractures or foliation, whereas the S_2 -wave is perpendicularly oriented to the S_1 -wave. If, in a single fracture model, the angle of incidence of the S -wave propagation along the direction of the fluid filled fractures, is low, the S_2 -wave propagates faster than the S_1 -wave (Crampin 1985). The arrival-time or velocity difference of both shear-waves can be described by the time-delay shear-wave anisotropy $\xi_{(t_{S_1}, t_{S_2})}$ or the velocity shear-wave anisotropy $\xi_{(v_{S_1}, v_{S_2})}$. ξ depends strongly on the propagation direction in an anisotropic medium. Low ξ -values are not necessarily indicative of low rock anisotropy, whereas high ξ -values are diagnostic of strong rock anisotropy, even if it is difficult to know whether the observed ξ -value is the largest possible value (Ji and Salisbury, 1993).

Shear-wave anisotropy occurs in basically three geological regimes:

1. in micro-/macro-scopically fractured rocks, with well oriented cracks, which are likely to be the most common source of effective anisotropy (Crampin 1985),
2. in hard rocks, with preferred foliation or mineral orientations, and
3. in sedimentary rocks, where sequences of thin sedimentary layers exist (Hake, 1993). The first and the second regime could be observed within the observed granitic gneisses of the Penninic gneiss zone in southern Switzerland and are discussed in this paper.

In the first geological regime, under deviatoric stress, cracks and fractures parallel to the maximum compressive stress direction may open. Dilatancy induces open cracks and fractures of small size compared to the seismic wavelengths (Crampin 1985). The fractures are characterised by a transversely isotropic symmetry or hexagonal symmetry (Crampin 1981), provided that only a single fracture family exists. These fractures cause shear-wave anisotropy that is called Extensive Dilatancy Anisotropy (EDA) (Crampin 1987, 1989).

The second geological regime is characterised by ductile shear-deformed metamorphic rocks such as gneisses, schists or mylonites. In laboratory experiments Kern and Wenk (1990) analysed fabric-related velocity anisotropy and shear-wave splitting in granodioritic mylonites and phyllonites under confining pressure up to 600 MPa. They concluded that both micro-fractures and single-crystal properties are additive

and enhance velocity anisotropy. Barruol et al. (1992) described an experimental laboratory study in quartzites, phyllonites, amphibolitic gneisses and acid granulites of ductile shear-zones under different confining pressure (< 600 MPa). They compared quantitatively the velocity distribution of the P-wave and S-waves as subjected to different mineral phases. Ji and Salisbury (1993) outlined and discussed laboratory measurement results of shear-wave velocities, anisotropy, and splitting in high-grade granitic mylonites (< 600 MPa). They discuss the velocity anisotropy of P- and S-waves, and the Poisson's ratio with subject to different mineralogic rock compositions and wave propagation directions.

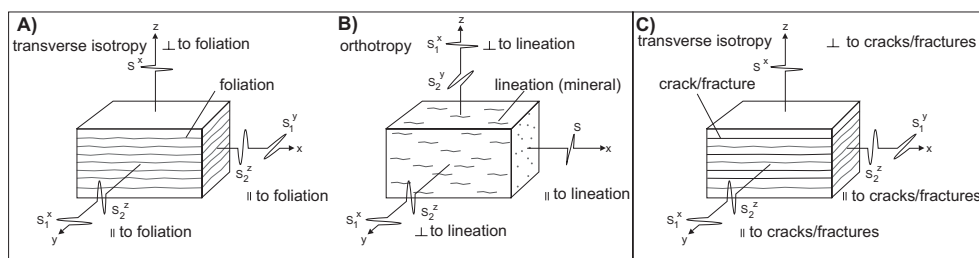


Figure 2.1: *Illustration of the polarisation phenomenon in structural anisotropic rock with respect to different directions x , y , and z of the S_1 and S_2 -wave propagation. Generally, the S_1 -wave shows a motion direction parallel to the anisotropic medium (transverse isotropy or orthotropy), whereas the S_2 -wave is perpendicularly oriented to the leading wave. Picture A) and B) show fabric-induced polarisation and picture C) shows crack/fracture-induced polarisation.*

Figure 2.1 illustrates the principle of the shear-wave motion directions in the two aforementioned geological regimes:

- For wave propagations parallel to a transversely isotropic $x - y$ -plan in figure 2.1 A) and C), the motion direction of the S_1 -wave lies parallel to this plane. In both propagation directions, ξ_x and ξ_y are equal (transversely isotropic).
- For wave propagations in x -direction in the orthotropic medium in figure 2.1 B), the motion direction of the S_1 -wave is undefined. The S_1 -motion direction is parallel to the fabric lineation in the $x - y$ -plane, for propagations in y -direction, perpendicular to the lineation. Wave propagation directions in z -direction in an orthotropic medium cause a motion direction of the S -waves parallel to the fabric lineation (Christensen, 1966, Kern and Wenk, 1990, Barruol et al., 1992, Ji and Salisbury, 1993, and Rabbel, 1994). The anisotropies ξ differ between the y and z propagation direction (orthotropic).

The motion direction and the shape of the displacement trajectories of the S_1 -waves, are controlled by the rock mass anisotropy near the receiver site (Crampin 1985). Particle displacements, recorded by three-component recordings, describe trajectories of particle motion over a short time window. The three-dimensional pictures of particle

motion, called hodograms, show successive predominant directions of the structural anisotropy. Particle trajectories can be represented by an equivalent ellipsoid (Samson 1973, Matsumura 1981, Cllet and Dubesset 1988). The three lengths $\lambda_1 \geq \lambda_2 \geq \lambda_3$ of the ellipsoid axes represent the eigenvalues of the particle trajectories and are the real wave amplitudes. The shape of an ellipsoid can be characterised by the axes-ratios.

This article describes a new simple graphical method to characterise the shapes of S_1 -wave polarisation ellipsoids. New parameters are introduced to describe the ellipsoid shapes. The theoretical background of this method is given in section 2.2. The new parameters are mathematically self-consistent if compared to conventional parameters: main, cross, and transverse ellipticity, the polarisation coefficient, the oblateness coefficient, and the linearity coefficient (Samson 1973, Samson 1977, Matsumura 1981, Cllet and Dubesset 1988). Additionally, the paper outlines a statistical classification approach by using the new shape parameters to determine the orientations of crack/fracture-induced and fabric-induced S_1 -polarisation ellipsoids, based on in-situ data in granitic gneisses in the Penninic gneiss zone in southern Switzerland. The in-situ data describe mixtures of anisotropies (MA) of different S_1 -wave ellipsoids caused by different fracture sets, schistositities, and fabric lineations, which can be observed along seismic measurement profiles. Hence, MA are a superposition of different rock mass anisotropies that occur in-situ. Seven measurement campaigns along seismic profiles were accomplished during the excavation in the 2600 m long and up to 1400 m deep Faido adit. The Faido adit is a NE oriented and 12% inclined access tunnel to the Gotthard base tunnel, which is a part of the AlpTransit project in Switzerland.

2.2 Shear-wave particle motion

As stated in section 2.1 the particle motion trajectories of a S-wave can be idealised by a displacement ellipsoid. The displacement ellipsoid of a polarised S_1 -wave is characterised by its shape and its predominant direction $\vec{\Theta} = \{\alpha, \theta\}$ (see figure 2.2). The orientation of the S_1 -wave polarisation ellipsoid (orientation of the largest axe λ_1) can be described by two angles, the inclination angle θ and azimuth angle α , where $0^\circ \leq \alpha \leq 360^\circ$ and $0^\circ \leq \theta \leq 90^\circ$. Both angles span up an axial (bi-directional) unit vector $\vec{\Theta}^{\{A\}} = \{\alpha, \theta\}$ within the lower hemisphere of an unit sphere (see figure 2.2). The orientation vector can be represented as a point A on the lower hemisphere surface of the unit sphere. Point A' in figure 2.2 is the projection of point A onto the horizontal stereographic plane (equal area). Thus, the 2-dimensional stereographic plot illustrates the spatial orientation of the S_1 -wave ellipsoid and is used for visualisation.

New shape parameters, which are introduced here, are derived from the natural logarithm of the aspect ratios between the axes lengths $\lambda_1 \geq \lambda_2 \geq \lambda_3$ of the three ellipsoid axes. They are defined as follows:

- the ellipsoids stretching $\ln\left(\frac{\lambda_1}{\lambda_2}\right)$,
- the ellipsoids flattening $\ln\left(\frac{\lambda_2}{\lambda_3}\right)$, and

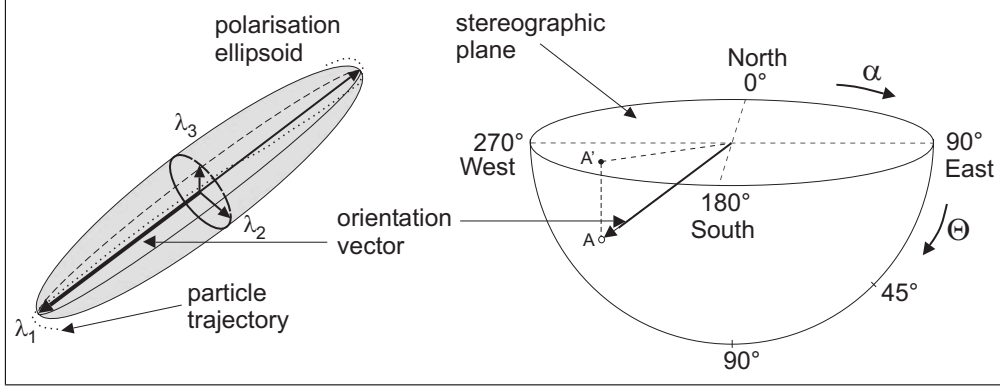


Figure 2.2: *Illustration of a polarisation ellipsoid. The orientation $\{\alpha, \Theta\}$ of the ellipsoid is defined by the direction of its largest axis λ_1 . Additionally, the orientation of an ellipsoid in the 3-dimensional spherical space can be visualised within a stereographic plane (equal area plot).*

- the ellipsoids shape intensity $I = \ln\left(\frac{\lambda_1}{\lambda_3}\right)$ (see eq. (2.3)).

The function $\ln(\cdot)$ fulfills the following conditions (see figure 2.3):

- the three shape parameters are equal to zero when the characteristic properties they describe are weak, e.g. low polarisation - the ratios of the λ s are one,
- the three shape parameters increase when the characteristic properties they describe get stronger, e.g. the ratios of the λ s decrease asymptotically to zero.

The logarithm gives a better understanding of the ellipsoid shapes, if compared to the main ellipticity $e_{21} = \sqrt{\frac{\lambda_2}{\lambda_1}}$, the transverse ellipticity $e_{32} = \sqrt{\frac{\lambda_3}{\lambda_2}}$, and the cross ellipticity $e_{31} = \sqrt{\frac{\lambda_3}{\lambda_1}}$, which are introduced and described by Samson (1973, 1977), Matsumura (1981) and Cllet and Dubesset (1988). The function $\sqrt{\cdot}$ does not fulfill the conditions outlined above (see figure 2.3). The ellipticities are used to calculate complicated coefficients to characterise ellipsoid shapes during stochastic processes (see Samson 1973, 1977):

- the global polarisation coefficient: $\tau^2 = \frac{(1-e_{21}^2)^2 + (1-e_{31}^2)^2 + (e_{21}^2 - e_{31}^2)^2}{2(1+e_{21}^2+e_{31}^2)^2}$.
It is equal to zero when polarisation is null and close to 1 when the polarisation approaches rectilinear behaviour.
- the oblateness coefficient: $p = 1 - \frac{3e_{31}}{(1+e_{21}+e_{31})}$.
It is equal to zero for a sphere and equal to one for any planar trajectory.
- the linearity coefficient $l = \frac{3}{2(1+e_{21}+e_{31})} - \frac{1}{2}$.
It equals to 1 for a straight line and zero for a sphere.

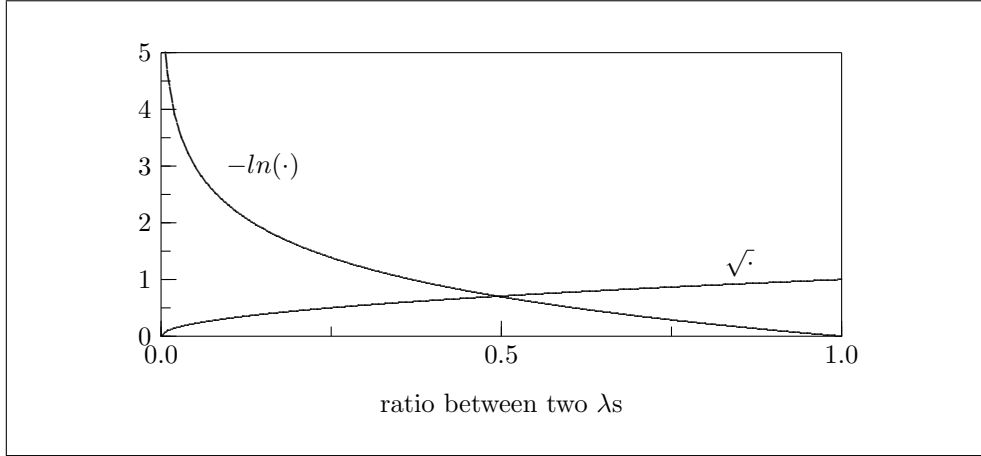


Figure 2.3: Transformation functions to describe the ratio between two λ s. The ratio is 1 when the λ s are equal (non-polarised wave). The ratio decreases with increasing polarisation. From the semantic point of view, a proper transformation function should fulfill the conditions, that its function values are low for low polarisation and they are high for high polarisation. $\ln\left(\frac{\lambda_1}{\lambda_3}\right) = -\ln\left(\frac{\lambda_3}{\lambda_1}\right)$ fulfills this conditions compared to $\sqrt{\frac{\lambda_3}{\lambda_1}}$.

There are three reasons why the new introduced shape parameters $\ln\left(\frac{\lambda_1}{\lambda_2}\right)$, $\ln\left(\frac{\lambda_2}{\lambda_3}\right)$, and $\ln\left(\frac{\lambda_1}{\lambda_3}\right)$ should be used to describe the shape of a displacement ellipsoid:

- It seems to be advantageous that τ^2 , p , and l range between 0 and 1. Nevertheless, from the mathematical point of view, an ellipsoid can be for example infinitely long stretched. Thus, the parameters that describe the ellipsoids stretching should range in the interval $[0, \infty)$. This condition is fulfilled by $\ln\left(\frac{\lambda_1}{\lambda_2}\right)$, $\ln\left(\frac{\lambda_2}{\lambda_3}\right)$, and $\ln\left(\frac{\lambda_1}{\lambda_3}\right)$. From the practical point of view, the length scales of the three shape parameters are naturally bounded with subject to the geological situation.
- The second reason is related to the graphical analyses of the ellipsoid shapes. In a simple cross-plot of the flattening $\ln\left(\frac{\lambda_2}{\lambda_3}\right)$ vs. the stretching $\ln\left(\frac{\lambda_1}{\lambda_2}\right)$, the shape intensity $\ln\left(\frac{\lambda_1}{\lambda_3}\right)$ occurs as a linear function (see figure 2.4 and eq. 2.3). But, in a cross plot of $\sqrt{\frac{\lambda_3}{\lambda_2}}$ vs. $\sqrt{\frac{\lambda_2}{\lambda_1}}$, the cross ellipticity $\sqrt{\frac{\lambda_3}{\lambda_1}}$ occurs as an exponential function. Thus, it is easier to visually interpret linear than exponential functions.
- The third reason is related to a method of statistical pattern recognition (Bishop 1995) to identify S_1 -wave orthotropy and transverse isotropy. A simple approach is to recognise polarisation patterns visually by observing the probability density of a single parameter. The goal is to find proper linear discriminant functions

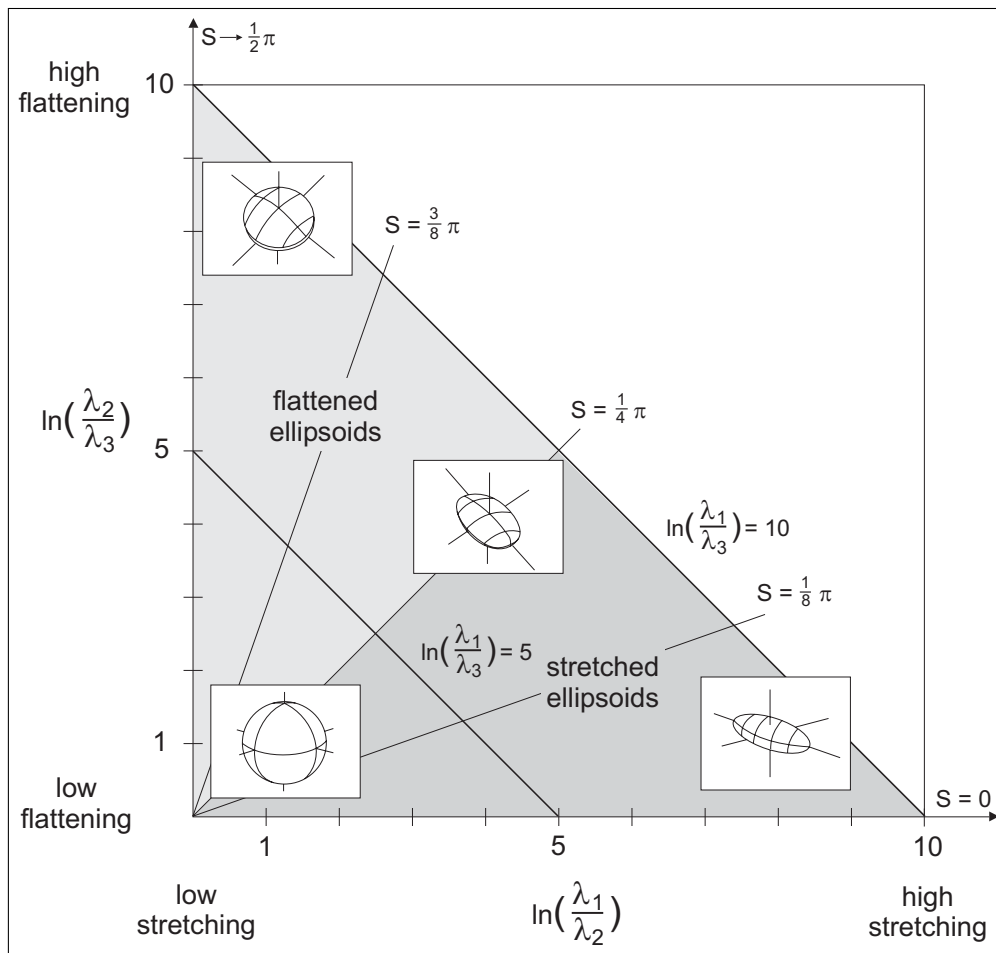


Figure 2.4: Flattening-stretching diagram to classify the S_1 -wave polarisation. The $\ln\left(\frac{\lambda_2}{\lambda_3}\right)$ - $\ln\left(\frac{\lambda_1}{\lambda_2}\right)$ diagram can be used to classify S_1 -wave orthotropy (stretched ellipsoids) and transverse isotropy (flattened ellipsoids) of an observed rock mass region. Both anisotropies built up Mixture of Anisotropies (MA) within the rock mass. The objective classification boundary between flattened and stretched ellipsoids is $S = \frac{1}{4}\pi$.

(decision boundaries) that separate different classes (see figure 2.5). This approach makes it necessary to use uncombined parameters. $\ln\left(\frac{\lambda_1}{\lambda_2}\right)$ or $e_{21} = \sqrt{\frac{\lambda_2}{\lambda_1}}$ are uncombined compared to τ^2 , p , and l , which combines e_{21} and e_{31} . A parameter combination can cause fuzzy probability density distributions and can lead to classification problems in order to find proper linear discriminant functions.

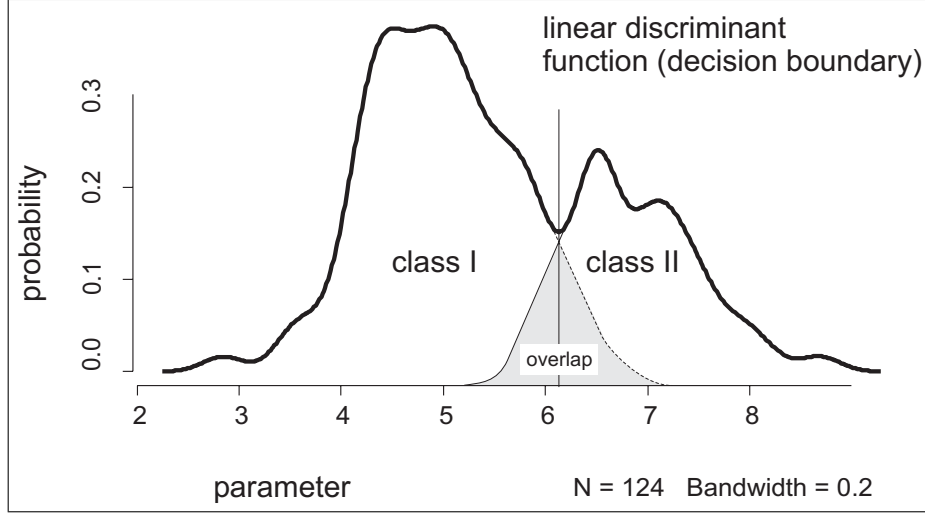


Figure 2.5: 2-class separation of a probability distribution of a real world example by a linear discriminant function. The probability distribution (called kernel density) of 124 data points is determined by a non-parametric technique of probability density estimation (Silverman 1986). The overlap describes a miss-classification area.

Figure 2.4 shows a cross-plot of the flattening $\ln\left(\frac{\lambda_2}{\lambda_3}\right)$ vs. the stretching $\ln\left(\frac{\lambda_1}{\lambda_2}\right)$. The ordinate shows all non-stretched ellipsoid shapes with $\lambda_2 = \lambda_1$ or $\ln\left(\frac{\lambda_1}{\lambda_2}\right) = 0$. The stretching intensity increases continuously with growing $\ln\left(\frac{\lambda_1}{\lambda_2}\right)$ -value. The abscissa shows all non-flattened ellipsoid shapes with $\lambda_3 = \lambda_2$ or $\ln\left(\frac{\lambda_2}{\lambda_3}\right) = 0$. The flattening intensity increases continuously with growing $\ln\left(\frac{\lambda_2}{\lambda_3}\right)$ -value. In the origin of the cross-plot, shear waves are non-polarised (spherical shape). A linear function S is defined by the slope angle or mutual angle between the stretching and flattening:

$$S = \arctan\left(\frac{\ln\left(\frac{\lambda_2}{\lambda_3}\right)}{\ln\left(\frac{\lambda_1}{\lambda_2}\right)}\right) \quad (2.1)$$

This single function, called shape measure S , describes the boundaries of different shape transitions between stretched and flattened polarisation ellipsoids. The shape measure with the slope angle $S = \frac{1}{4}\pi$ (45°) separates the stretched ellipsoids from the flattened ellipsoids.

Linear functions that link the same values on the ordinate and on the abscissa in figure 2.4 and that are orthogonal to $S = \frac{1}{4}\pi$, can be defined as follows:

$$\ln\left(\frac{\lambda_2}{\lambda_3}\right) = -\ln\left(\frac{\lambda_1}{\lambda_2}\right) + I, \quad (2.2)$$

whereby the already introduced shape intensity I is equal to:

$$\begin{aligned} I &= \ln\left(\frac{\lambda_2}{\lambda_3}\right) - \ln\left(\frac{\lambda_2}{\lambda_1}\right) \\ &= \ln\left(\frac{\lambda_2 \lambda_1}{\lambda_3 \lambda_2}\right) \\ &= \ln\left(\frac{\lambda_1}{\lambda_3}\right) \end{aligned} \quad (2.3)$$

Thus, the third shape parameter $\ln\left(\frac{\lambda_1}{\lambda_3}\right)$ determines the intensity I of the ellipsoid shapes and shows the maximum axes-ratio between the shortest axis λ_3 to the longest axis λ_1 of an ellipsoid. The intensity can be read at the sections on the ordinate and on the abscissa in figure 2.4.

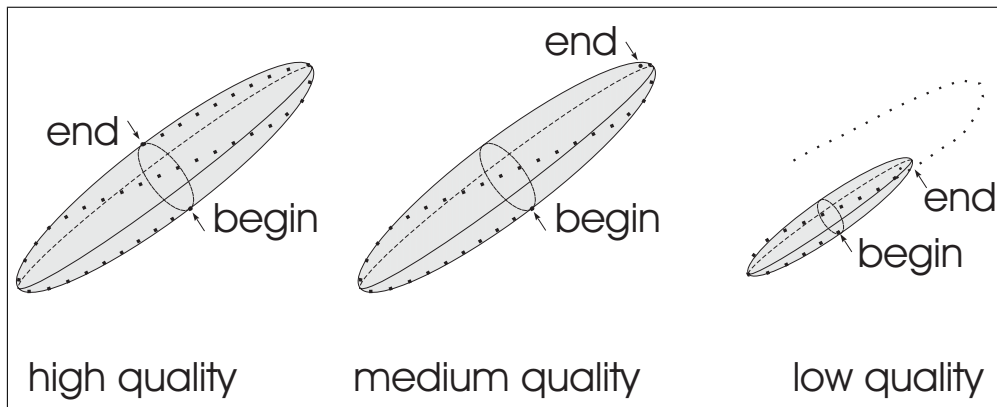


Figure 2.6: *Polarisation ellipsoids that fit the particle motion trajectories of the S_1 -wave depend strongly on the splitting quality between the two S -waves. If the motion of a S_1 -wave is equal to one wave period, the splitting quality is high (left ellipsoid). Hence, the ellipsoid shape can be determined by the total motion information of the S_1 -wave. Portions of wave periods led to lower quality of ellipsoid determination and interpretation.*

Figure 2.6 shows three idealised cases, how the splitting quality between the S_1 - and the S_2 -wave influences S and I of the approximated S_1 -wave polarisation ellipsoids. The less information on the wave motion is available, the less is the interpretation quality of the shape parameters. If the S_1 -wave train is equal to one wave period, the quality of S and I is high. Portions of wave periods led to lower qualities as illustrated in figure 2.6. A representative amount of ellipsoids should be analysed for a geological

interpretation, see section 2.4.3. The statistics of such a data set show the variability due to the geology-induced polarisation and the variability due to the shear-wave splitting (influence of the offset). The latter influence decreases the more ellipsoids of S_1 -waves with different offsets are analysed. For example, S_1 -wave ellipsoids with "short" offsets (here: ≤ 20 m) would lead to a low interpretation quality of S and I .

2.3 Geological settings

The in-situ measurements were carried out in the Penninic gneiss zone in southern Switzerland. It consists of the Leventina gneisses and the Lucomagno gneisses. Figure 2.7 B) shows a geological map and figure 2.7 C) shows a cross section of the geological situation along the Faido tunnel.

The Leventina and the Lucomagno gneisses represent multiple deformed and metamorphically overprinted rocks with complex boundaries (Ettner 1999, Pettke and Klaper 1992). The observed rocks are characterised by gneisses of granitic composition. The Leventina nappe is constituted by orthogneisses with laminated, augen-structured, and plicated fabric structures. Its composition is (Schneider, 1997):

- quartz (25-43%)
- feldspar (38-60%)
- mica (9-24%)
- accessories (1-5%).

Generally, Leventina gneiss varieties show flow structures with well aligned feldspar minerals (Schneider 1993). Two schistositys, called ss_1 and ss_2 , exist within the Leventina gneiss. The older ss_1 -schistosity is generally $10 - 30^\circ$ to the North (0°) oriented. ss_1 is not visible at the macro scale in the Leventina gneisses along the Faido tunnel. During the evolution, ss_2 overprinted and folded the ss_1 irregularly. ss_2 is $10 - 30^\circ$ to the South (180°) oriented. It is characterised by parallel mica minerals in schistic gneiss varieties and by the aligned quartz and feldspar minerals in augen-structured, laminated and plicated gneiss varieties. Casasopra (1939) showed that the feldspar minerals are aligned into the direction of ss_2 . Stretched feldspar minerals occur in laminated, and plicated gneiss varieties. Minerals are less aligned in regions of massive gneisses. Section 2.4.2 shows the influence of this orthotropic rock structure on the shear-wave splitting phenomenon. At the Leventina/Lucomagno nappe boundaries, both the lithological banding and the ss_2 dip angle range from shallow to almost 90° .

The Lucomagno nappe is constituted by coarse and fine grained orthogneisses and paragneisses with augen-structured and plicated fabric structures. The orthogneisses consist of (Schneider, 1997):

- quartz (20-55%)

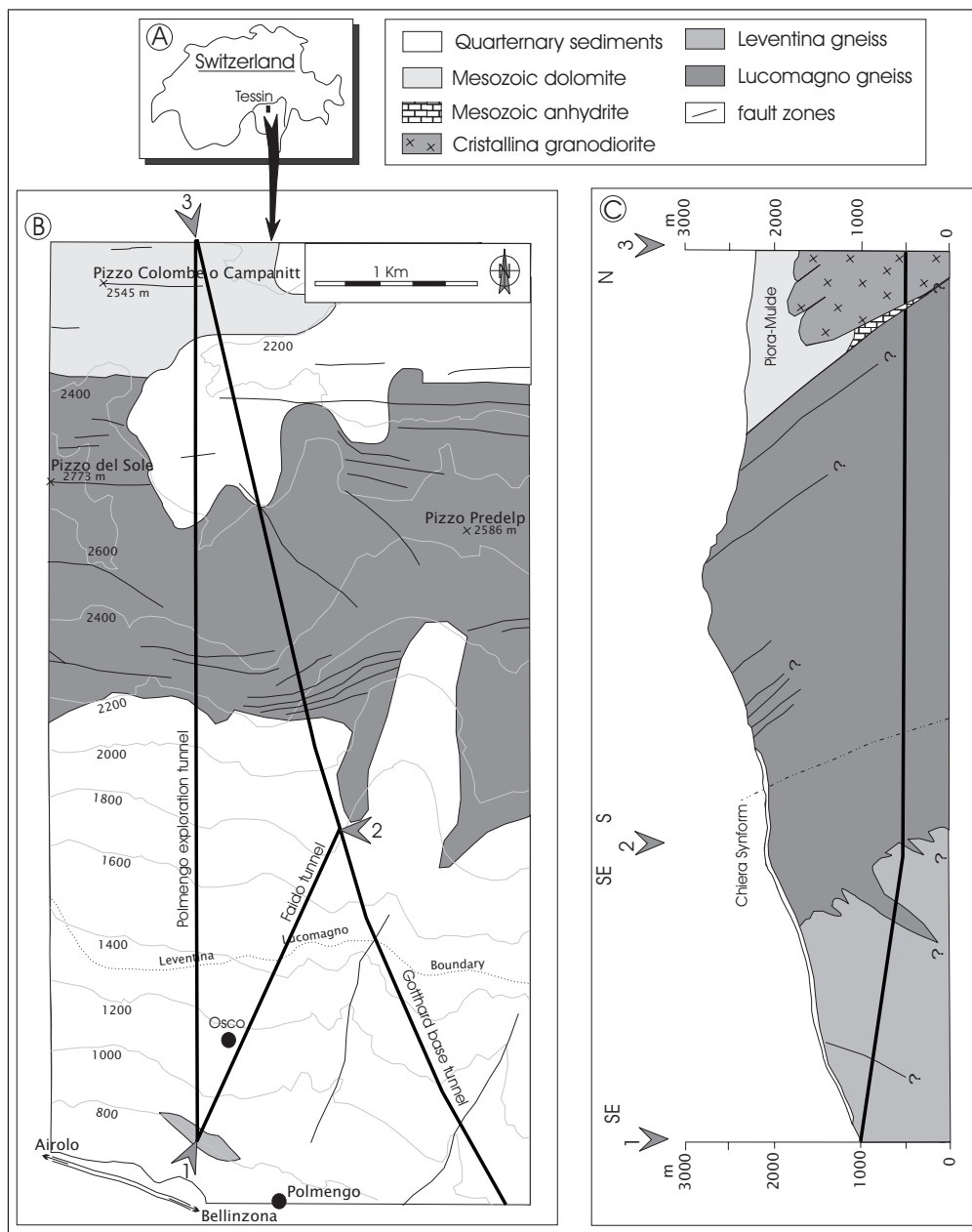


Figure 2.7: Geographical and geological overview of the Faido tunnel in southern Switzerland. Picture A) shows the location of the observed region. Picture B) shows a schematic geological map and picture C) a cross section along the Faido (profile 12) and along a part of the Gotthard base tunnel (profile 23).

- alkali-feldspar (0-45%)
- plagioclase (0-70%)
- muscovite (0-20%)
- biotite (0-6%).

The paragneisses show the following rock composition (Schneider, 1997):

- quartz (20-70%)
- plagioclase (10-35%)
- biotite (3-30%)
- sericite, muscovite (0-30%)
- garnet (0-15%).

In the Faido tunnel, the Lucomagno gneiss shows a ss_2 -orientation with a dip angle of $70-90^\circ$ to the South (180°). The Lucomagno gneiss occurs between tunnel meter 2024 m and 2150 m. It can be assumed, that the interpreted geological tunnel profile, which is schematically illustrated in figure 2.7 C), cuts across a limb of a isoclinal fold. Figure 2.8 to figure 2.14 show seven vertical geological tunnel profiles with the extensions of the seismic profiles.

Due to the multiple and strong overprints of the Alpine evolution, all gneiss varieties are dissected by discordant/concordant, folded/unfolded quartz and biotite lentils and veins. Additionally, the gneisses are interstratified with joint sets, fissured zones, and brittle faults. The latter occur as cataclasites (non-cohesive brittle faults) and fault gouges (cohesive brittle faults) (Passchier and Trouw 1996). Three major fracture families build up the different joint sets and fissured zones. Macroscopic fractures were observed along the Faido access tunnel and compared with the phenomenon of shear-wave anisotropy in section 2.5. The existence of (micro)cracks was not taken into account, which are usually responsible for shear-wave splitting (Crampin, 1985). Nevertheless, Hoagland et al. (1973) and Whittaker et al. (1992) outlined, that under progressive loading micro-cracks and a fracture process zone FPZ may develop around a fracture tip. Then, after further loading a macroscopic fracture is formed by linking some of the microcracks. A new FPZ is developed ahead of the fracture tip. Thus microcracks may coincide with fractures. In a simplified geological situation, the orientations and the spacings of the main fracture families are shown in figure 2.8 to figure 2.14.

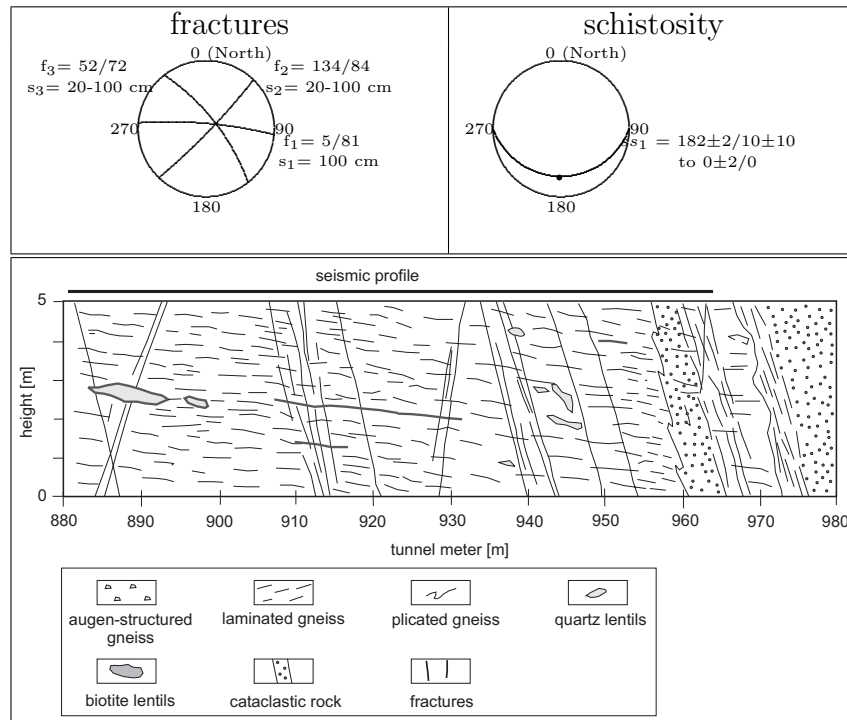


Figure 2.8: Schematic sketch of the geological situation, the orientations (dip direction/dipping) of the fractures with fracture spacing s and the schistosity along the seismic profile between 881 - 963 m. The geological profile is vertically 5 times exaggerated. The geology shows a laminated biotite gneiss (Leventina gneiss), which is fine- to middle-grained, quartz-rich with quartz-lentils (cm- to dm-scale).

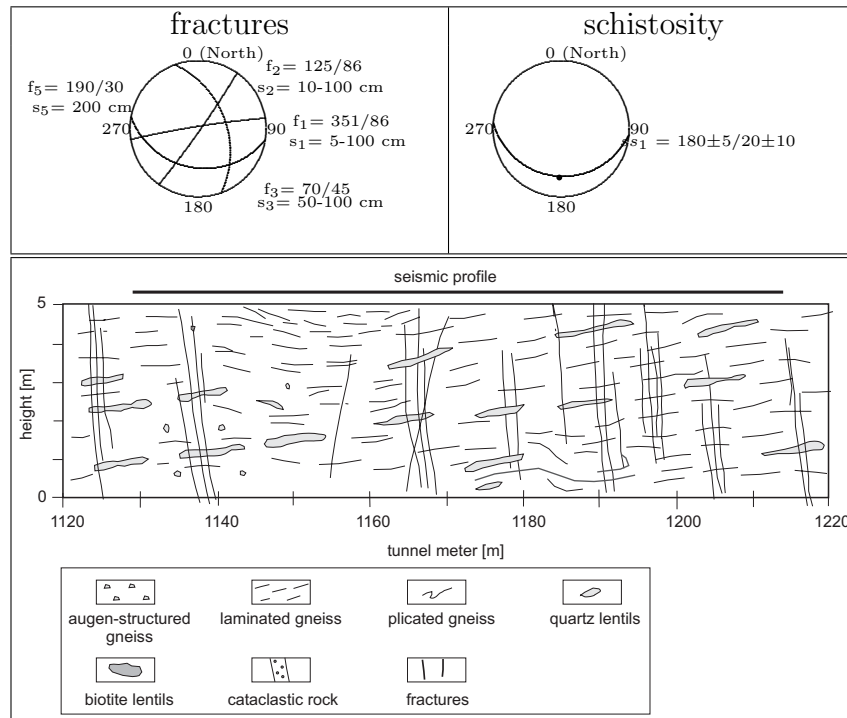


Figure 2.9: Schematic sketch of the geological situation, the orientations (dip direction/dipping) of the fractures with fracture spacing s and the schistosity along the seismic profile between 1130 - 1215 m. The geological profile is vertically 5 times exaggerated. The geology shows a laminated biotite gneiss (Leventina gneiss), which is middle-grained, locally fine-grained, partly quartz-rich with quartz-lentils (cm- to dm-scale), locally schistic and augen-structured. A mylonitic shear-band occurs between 1170 and 1200 m.

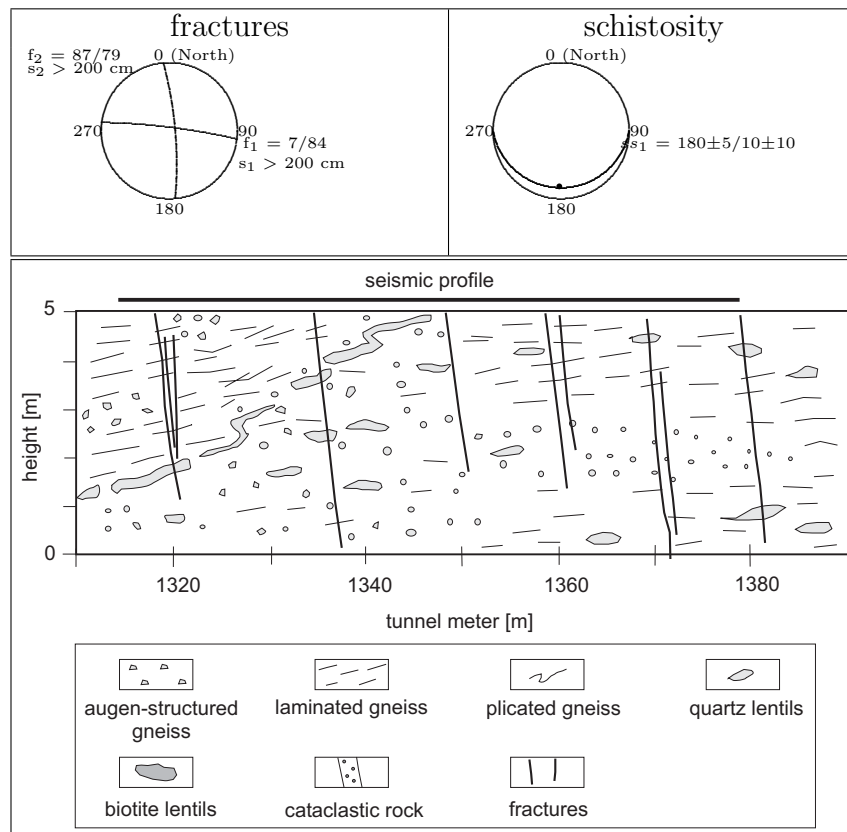


Figure 2.10: Schematic sketch of the geological situation, the orientations (dip direction/dipping) of the fractures with fracture spacing s and the schistosity along the seismic profile between 1314 - 1379 m. The geological profile is vertically 5 times exaggerated. The geology shows a augen-structured massive gneiss (Leventina gneiss), which is middle-grained, partly quartz-rich with quartz-lentils (cm- to m-scale), and locally laminated and plicated.

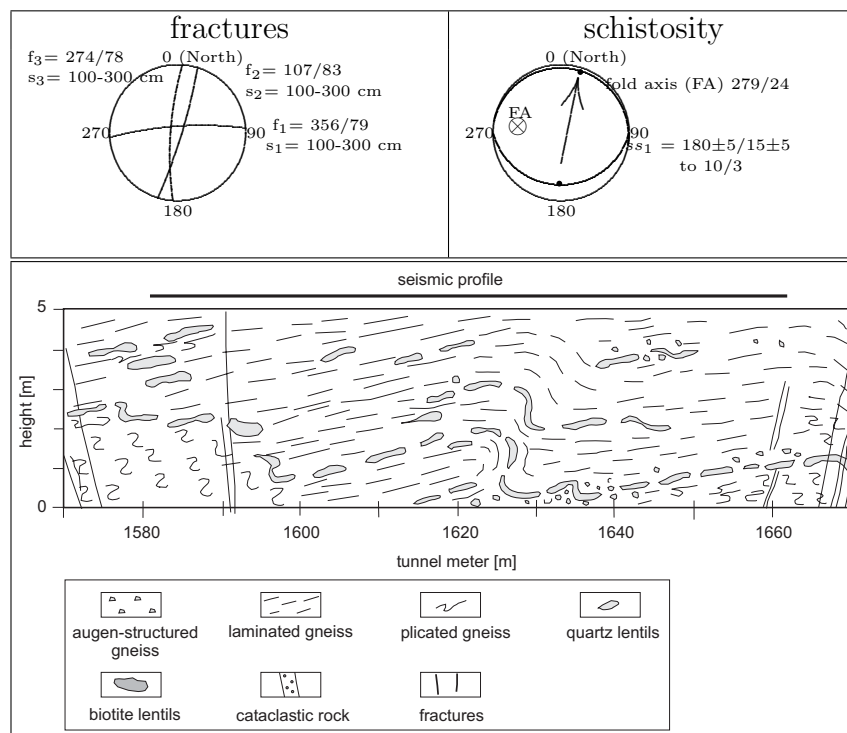


Figure 2.11: Schematic sketch of the geological situation, the orientations (dip direction/dipping) of the fractures with fracture spacing s and the schistosity along the seismic profile between 1582 - 1663 m. The geological profile is vertically 5 times exaggerated. The geology shows a laminated biotite gneiss (Leventina gneiss), which is middle- to fine grained, locally plicated, irregular folded (dm- to m-scale), augen-structured, and weak schistic, partly quartz-rich with quartz-lentils (cm- to dm-scale). Small fold structures (dm- to m-scale) occur and cause a rotation of the schistosity.

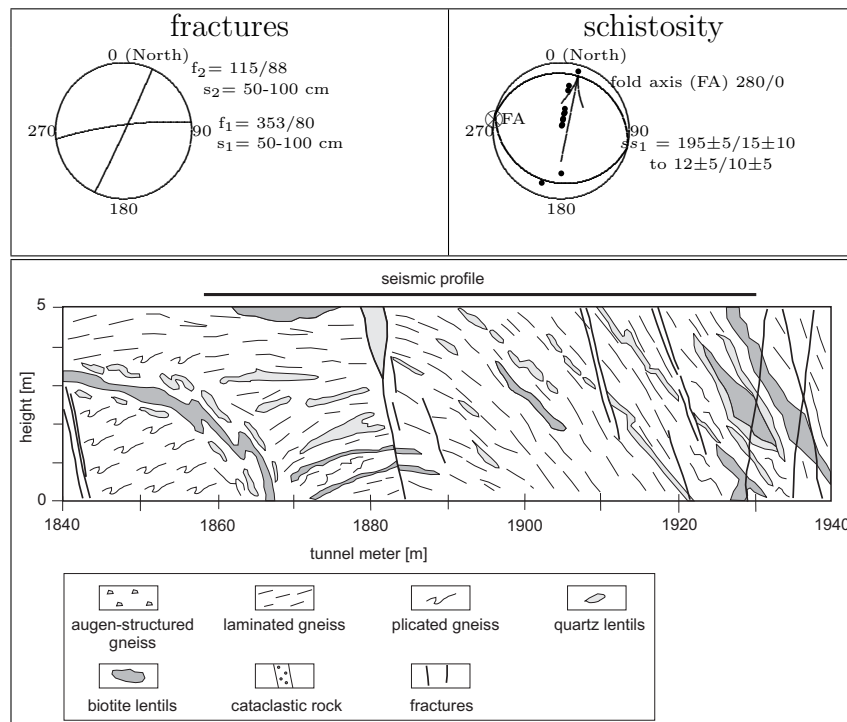


Figure 2.12: Schematic sketch of the geological situation, the orientations (dip direction/dipping) of the fractures with fracture spacing s and the schistosity along the seismic profile between 1858 - 1920 m. The geological profile is vertically 5 times exaggerated. The geology shows a laminated biotite/muscovite gneiss (Leventina and Lucomagno gneiss), which is middle- to fine grained, strong plicated, locally augen-structured, and partly mica-rich with mica-schist (cm- to dm-scale). A fold structure in decameter scale rotates the ss_2 -schistosity from 195/15 to 12/10.

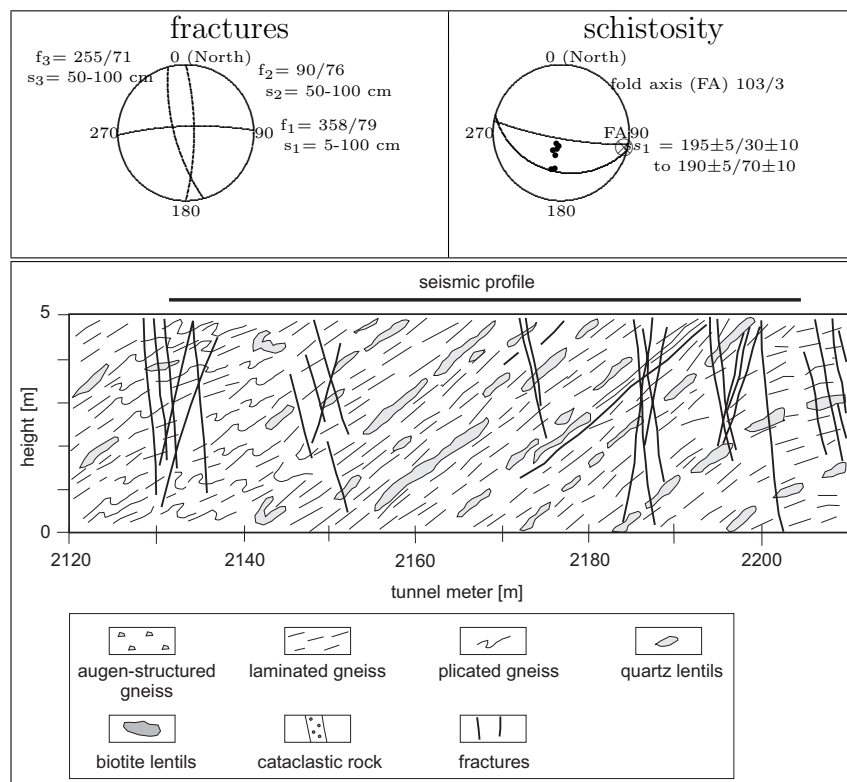


Figure 2.13: Schematic sketch of the geological situation, the orientations (dip direction/dipping) of the fractures with fracture spacing s and the schistosity along the seismic profile between 2132 - 2205 m. The geological profile is vertically 5 times exaggerated. The geology shows a biotite/muscovite gneiss and schist (Lucomagno/Leventina gneiss), which is fine- to middle-grained, strong plicated, locally augen-structured, partly with mica- and quartz-lentils (dm- to m-scale) parallel to schistosity. The ss_2 -schistosity ranges between $195 \pm 5/30 \pm 10$ and $190 \pm 5/70 \pm 10$.

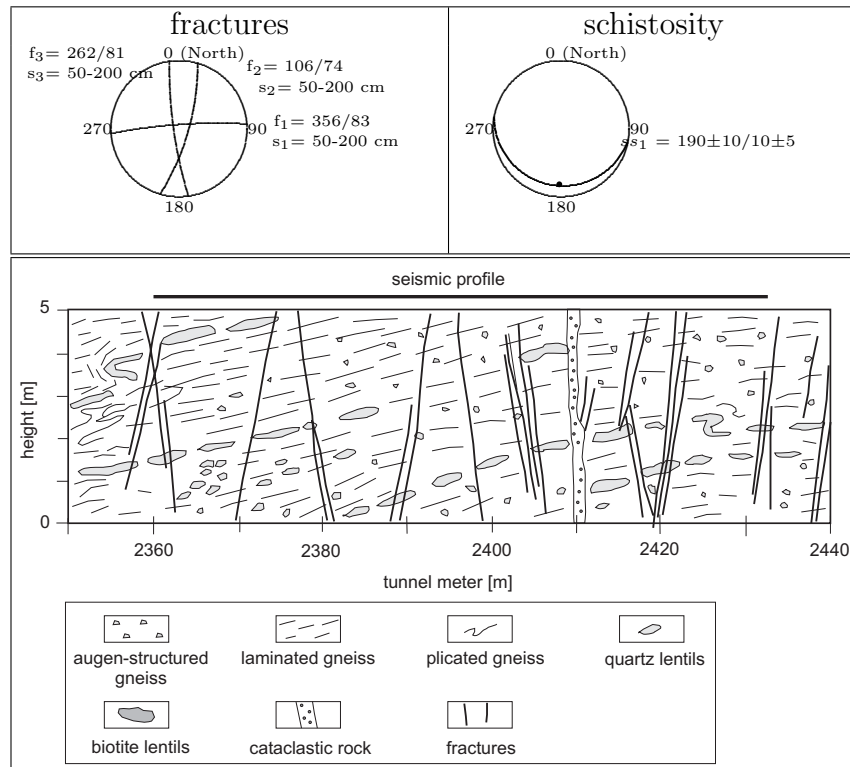


Figure 2.14: Schematic sketch of the geological situation, the orientations (dip direction/dipping) of the fractures with fracture spacing s and the schistosity along the seismic profile between 2360 - 2433 m. The geological profile is vertically 5 times exaggerated. The geology shows a biotite gneiss and schist (Leventina gneiss), which is middle-grained, strong plicated, locally augen-structured and laminated, with quartz-lentils (cm- to dm-scale).

2.4 Seismic data acquisition

2.4.1 Overview

GeoForschungsZentrum Potsdam carried out a series of seismic in-situ measurements in the Faido access tunnel, that is located in southern Switzerland on the main road between Airolo in the North and Bellinzona in the South. Figure 2.7 gives an overview about locations of Faido tunnel, the Piora exploration tunnel, and the Gotthard base tunnel. Seven measurement campaigns along seismic profiles were realised during tunnel excavations in the 2600 m long, up to 1400 m deep and 12% inclined Faido adit with NE-SW orientation.

2.4.2 Laboratory measurements

Laboratory measurements were carried out to analyse the anisotropic rock properties of the Leventina and Lucomagno gneisses. Two types of intrinsic anisotropies are possible, as defined in figure 2.1 A) and B) and outlined in section 2.1. Both, the Leventina and Lucomagno gneisses, exemplify an intrinsic orthotropy of the shear-wave velocities. The S_1 -waves polarise along the direction of the rock lineations, where feldspar and quartz minerals are aligned. In figure 2.15 A) and B), the results of the shear-wave velocity anisotropies $\xi(v_{S1}, v_{S2})$ of a laminated Leventina gneiss and an augen-structured Lucomagno gneiss are plotted versus the confining pressure. In the Faido tunnel, the laminated Leventina gneiss represents the slightest deformed gneiss variety, if compared to the other gneiss varieties and to the Lucomagno gneiss.

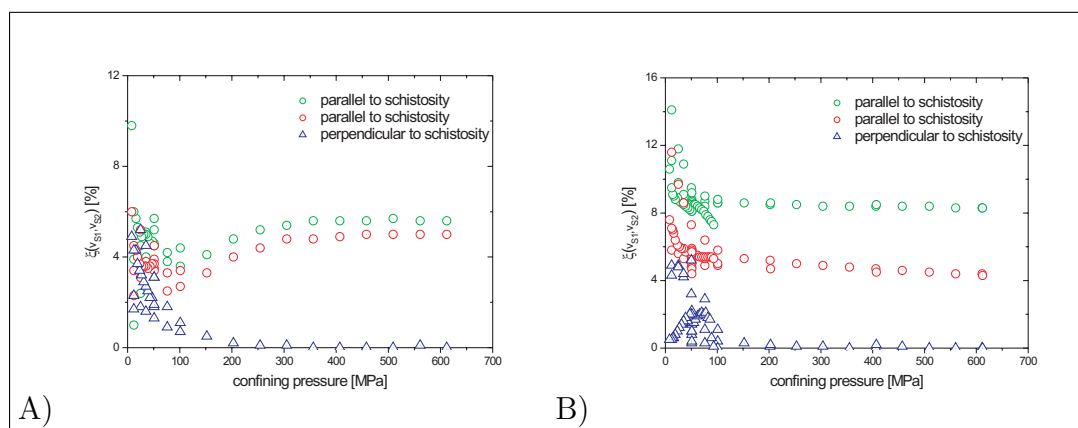


Figure 2.15: Shear-wave velocity anisotropies $\xi(v_{S1}, v_{S2})$ of a laminated Leventina gneiss A) and a laminated Lucomagno gneiss B) rock sample as a function of the confining pressure. The results are based on laboratory measurements. The differences of the ξ -values in all orthogonal wave propagation directions show an intrinsic rock orthotropy of the shear-wave velocities, see figure 2.1 B).

2.4.3 In-situ measurements

Seismic measurements were carried out simultaneously during the tunnel excavation of the Faïdo access tunnel. Figure 2.16 illustrates schematically the seismic profile along the tunnel wall.

Three one-component geophones, mutually orthogonal, record the seismic data and, thus, the 3-dimensional information on the seismic waves. A single seismic profile has an offset between 50 to 70 m. The distance between the geophone-anchors is 9 m. The 1.9 m long anchors are cemented in boreholes with standard two component epoxy resin which guarantees an optimum coupling of the geophones to the surrounding rock, whereby the receivers detect the full seismic wave field up to 3 kHz. Laboratory studies show a statistical error of the geophones of less than 5%. A mechanical hammer is used as acoustic source. The distance between the shot points of the hammer is 1.5 m. The hammer transmits impulse signals up to frequencies of 2 kHz with a repetition rate of 5 s. Therefore, a series of impacts can be generated within a few minutes. The maximum trigger error is less than 0.1 ms. This small time delay, together with the excellent consistency of the transmitted signals at each source points, leads to a significant enhancement of the signal-to-noise ratio by using vertical stacking. This is a well known statistical procedure, useful to enhance correlated signals, like reflections from discontinuities, and to reduce non-correlated signals like drill noise from the drilling process (TBM or Drill/Blast).

The recorded shear-waves propagate along the seismic profiles with velocities between 2.9 and 3.5 km/s and with frequencies between 400 and 600 Hz. Hence, they show wave length between 4.8 and 8.8 m. All measured shear-waves are perfectly splitted - each S_1 -wave is undisturbed by the S_2 -wave and vice versa. Both S -waves are also undisturbed by the P -waves and the high energetic surface waves (see figure

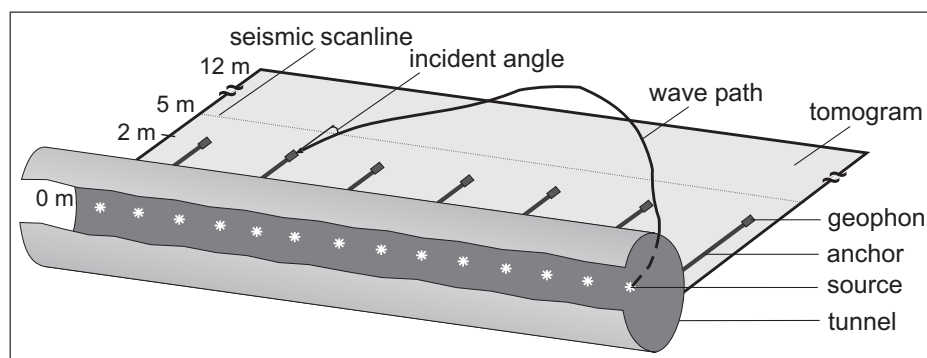


Figure 2.16: Schematic illustration of the installed geophysical measurement units (sources, receivers, and anchors) and of the tomogram within the tunnel. A generated acoustic wave propagates in the interior of the rock and reaches a receiver with an incident angle, which is only a few degrees. The incident angle is the angle between the idealised wave path plane and the tomogram plane.

2.17). The arrival times of the two direct shear-waves t_{S_1} and t_{S_2} , extracted from seismograms, are used to calculate the time delay shear-wave anisotropy $\xi_{(t_{S_1}, t_{S_2})}$, for the 'splitting quality' of the S_1 and the S_2 -waves, i.e. it indicates how much the two waves are separated. 1092 S_1 -waves, almost half of all recorded S_1 -waves, which are used for further observations, propagate at least along a 20 m offset and show an anisotropy between 2.5 % and 20 %. The S_1 -waves show wave trains of at least the half of their wave length. Excellent splitting quality requires a S_1 -wave train of one wave length.

In anisotropic rock masses, the phenomenon of shear wave polarisation leads to a wide range of polarisation patterns, whereas the polarisation ellipsoids of the S_1 -waves differ in shape, intensity, and orientation. 1092 analysed ellipsoids show the following mean length of the axes: $\lambda_1 = (1.2520 \pm 0.0074) 10^{-3} \text{ V/ms}^{-1}$ (0.56 %), $\lambda_2 = (0.0910 \pm 0.003) 10^{-3} \text{ V/ms}^{-1}$ (3.31 %), and $\lambda_3 = (0.0110 \pm 0.0005) 10^{-3} \text{ V/ms}^{-1}$ (0.05 %). The unit of the length is volt per meter per second. Statistical and systematic errors that influence these values can be summarised as follows:

statistical errors: 1) precision of the experimenter (picking error), 2) accidental influence of the environment during the experiment, 3) splitting quality between the two S-waves that depends on the travel time and source receiver distance, 4) time registration rate ($1/32 10^{-3} \text{ s}$), 5) accuracy of the mutually orthogonal geophones

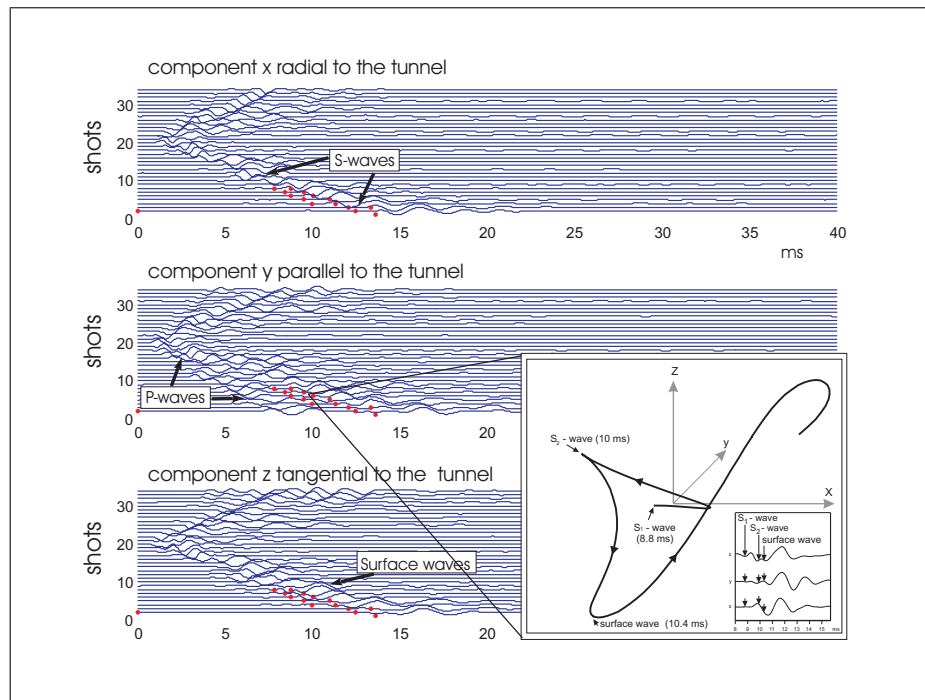


Figure 2.17: Example of a seismogram and 3-d particle displacement of the S_1 -wave, S_2 -wave, and the high energetic surface wave. It can be seen that the S_1 -wave is undisturbed by the S_2 -wave and vice versa. The S_2 -wave is perpendicularly oriented to the S_1 -wave. The dots within the seismograms represent the start and end times of the S_1 -waves.

(influence of the gravity) and 6) variability of structural anisotropies in the rock mass

systematic errors: 1) systematic influence of the environment during the seismic experiment and 2) heterogeneity of structural anisotropies in the rock mass

Statistical errors influence the precision (variability) of the observations, whereas systematic errors influence the accuracy (mean value) and the precision of the observations. The maximum errors of the shape measure S (after eq. 2.1) and the shape intensity I (after eq. 2.3) that result from the measurement precision $\lambda_{1,2,3} = 0.001 \text{ } 10^{-3} \text{ V/ms}^{-1}$ with $\lambda_1 = (1.250 \pm 0.001) \text{ } 10^{-3} \text{ V/ms}^{-1}$, $\lambda_2 = (0.090 \pm 0.001) \text{ } 10^{-3} \text{ V/ms}^{-1}$, and $\lambda_3 = (0.010 \pm 0.001) \text{ } 10^{-3} \text{ V/ms}^{-1}$ are as follows: $\Delta S = 0.0114(1.8\%)$, $\Delta I = 0.0528(1.0\%)$.

The determination of the ellipsoid orientations $\alpha \pm \Delta\alpha$ and $\Theta \pm \Delta\Theta$ is based on the amplitude values λ_1^x , λ_1^y , and λ_1^z of the largest axes 1, with $\lambda_1^x = (0.370 \pm 0.001) \text{ } 10^{-3} \text{ V/ms}^{-1}$, $\lambda_1^y = (0.450 \pm 0.001) \text{ } 10^{-3} \text{ V/ms}^{-1}$, and $\lambda_1^z = (0.17 \pm 0.001) \text{ } 10^{-3} \text{ V/ms}^{-1}$. The vectors $\{\lambda_1^x, \lambda_1^y, \lambda_1^z\}$ have to be transformed into unit vectors $\{\hat{\lambda}_1^x, \hat{\lambda}_1^y, \hat{\lambda}_1^z\}$. The transformation is necessary, because orientations of vectors that are based on two angles $\{\alpha, \theta\}$, as stated in section 2.2, can be simplest described within a unit sphere. $\Delta\alpha$ and $\Delta\theta$ can only be determined with subject to different vector orientations:

- For steep orientations ($\theta \lesssim 90.0^\circ$) is $\Delta\alpha \approx 3.2^\circ$ and $\Delta\theta \approx 2.2^\circ$.
- For oblique orientations ($\theta = 45.0^\circ$) is $\Delta\alpha \approx 0.3^\circ$ and $\Delta\theta \approx 0.3^\circ$.
- For shallow orientations ($\theta \gtrsim 0.0^\circ$) is $\Delta\alpha \approx 0.2^\circ$ and $\Delta\theta \approx 0.2^\circ$.

This error analysis shows, that more statistical errors influence the precision of the shape, intensity, and orientation of the ellipsoids. The determination of steep oriented ellipsoids is less confident than in the case of shallow oriented ellipsoids.

Figure 2.18 to figure 2.24 show the data distributions of the shape parameters of each seismic profile in detail. The related orientations of the shear-wave ellipsoids, shown in figure 2.18 A) to figure 2.24 A), are highly noised. The in-situ data describe mixtures of anisotropies (MA) of different S_1 -ellipsoid shapes and orientations caused by different geological rock mass anisotropies (see figure 2.1). Hence, MA are a superposition of different anisotropies that occur in-situ. MA can be fabric-induced and crack induced (naturally and artificially). Artificially induced cracks and fractures occur within the excavation disturbed zone (EDZ) around the tunnel, which is caused by the changes of the stress field and by the tunnel excavation process (drill/blast). They strongly influence the recognition of natural anisotropies and their orientations.

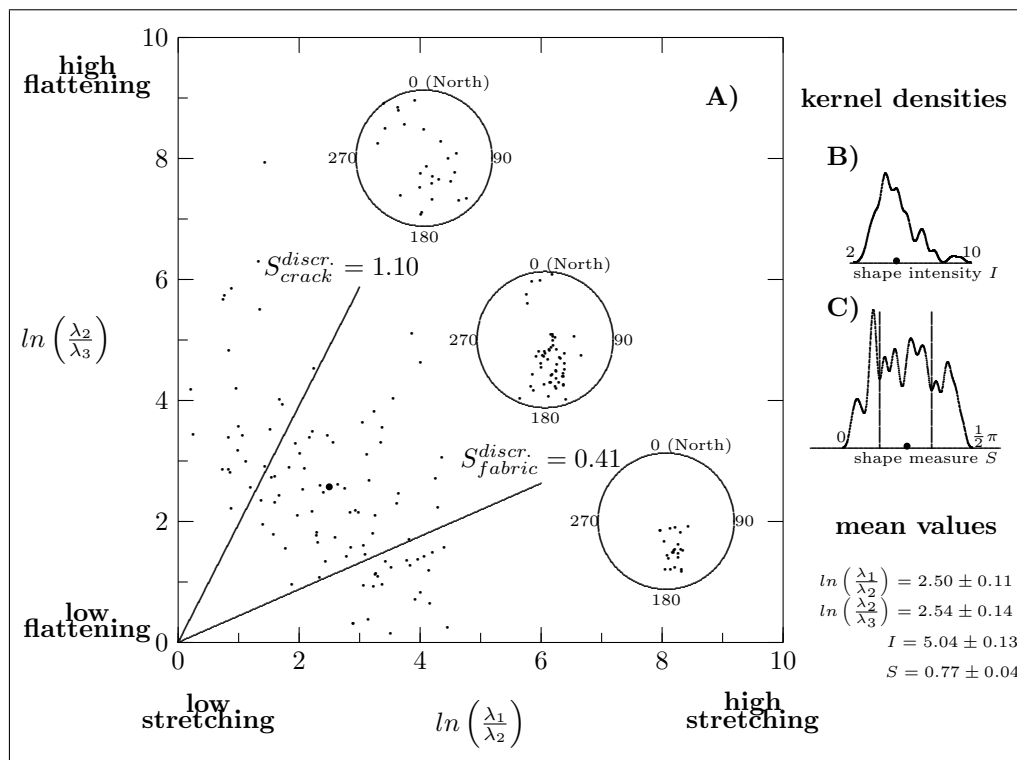


Figure 2.18: Illustration of the polarisation ellipsoids of the S_1 -waves at tunnel meter 881-963 m. Picture A) shows the $\ln\left(\frac{\lambda_2}{\lambda_3}\right)$ vs. $\ln\left(\frac{\lambda_1}{\lambda_2}\right)$ cross-plot with the mean value (\bullet). The two discriminant functions $S^{discr.}$ in picture A) are derived from the kernel density function in picture C). The stereographic plots show the orientations of the separated displacement ellipsoids.

Table 2.1: Comparison of the mean orientations of the separated and clustered S_1 -wave polarisation ellipsoids with the orientations of the related geological rock mass structures along the profile between 881-963 m.

S_1-wave orientations	
transverse isotropy	orthotropy
<p>0 (North) $61 \pm 20 / 70 \pm 6$</p> <p>270 90 180</p>	<p>0 (North) $166 \pm 7 / 32 \pm 4$</p> <p>270 90 180</p>
related geology	
fractures	schistosity and lineation
<p>0 (North)</p> <p>$f_3 = 52/72$ $f_2 = 134/84$ $s_3 = 20-100$ cm $s_2 = 20-100$ cm</p> <p>270 90 $f_1 = 5/81$ $s_1 = 100$ cm</p> <p>180</p>	<p>0 (North)</p> <p>270 90 $s_1 = 182 \pm 2 / 10 \pm 10$ to $0 \pm 2 / 0$</p> <p>180</p>

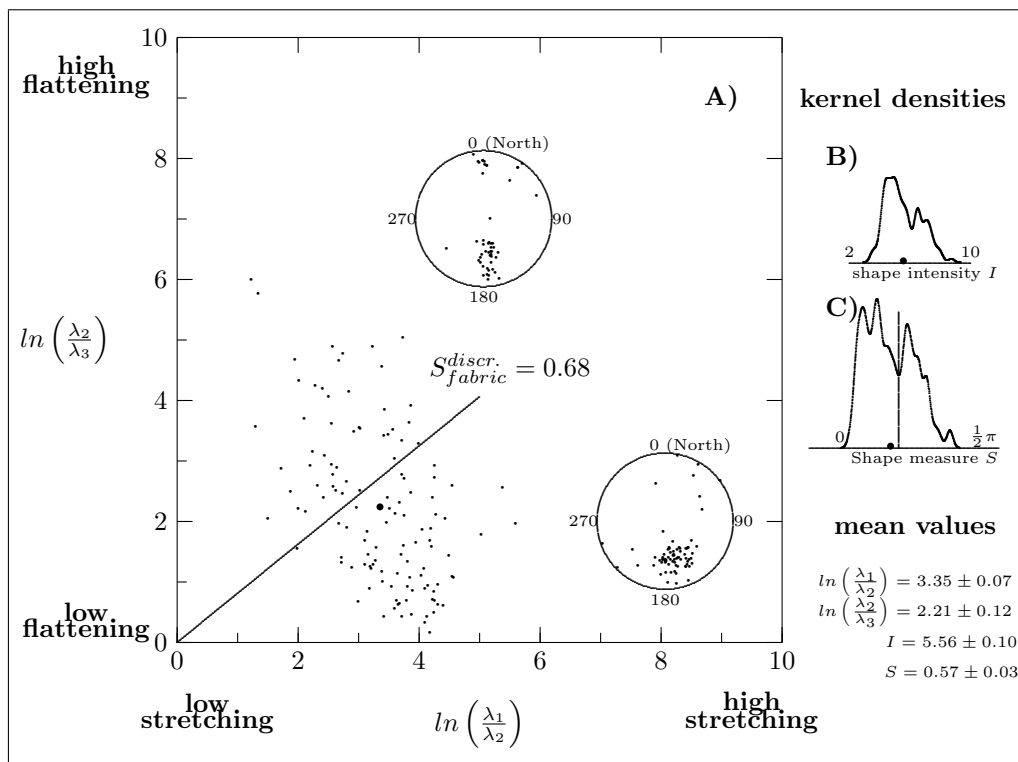
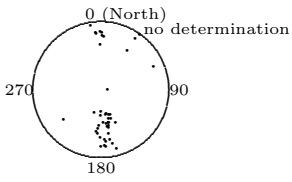
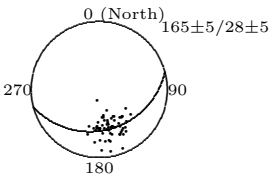
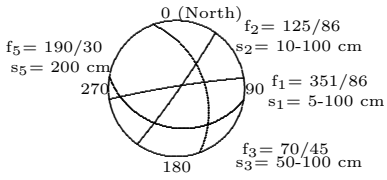
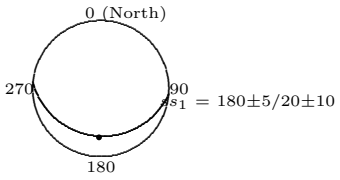


Figure 2.19: Illustration of the polarisation ellipsoids of the S_1 -waves at tunnel meter 1130-1215 m. Picture A) shows the $\ln\left(\frac{\lambda_2}{\lambda_3}\right)$ vs. $\ln\left(\frac{\lambda_1}{\lambda_2}\right)$ cross-plot. The discriminant function $S^{discr.}$ in picture A) is derived from the kernel density function in picture C). The stereographic plots show the orientations of the separated displacement ellipsoids.

Table 2.2: Comparison of the mean orientations of the separated and clustered S_1 -wave polarisation ellipsoids with the orientations of the related geological rock mass structures along the profile between 1130-1215 m.

S_1 -wave orientations	
transverse isotropy	orthotropy
 <p>0 (North) no determination</p> <p>270 90 180</p>	 <p>0 (North) $165 \pm 5 / 28 \pm 5$</p> <p>270 90 180</p>
related geology	
fractures	schistosity and lineation
 <p>0 (North)</p> <p>$f_5 = 190/30$ $s_5 = 200$ cm</p> <p>$f_2 = 125/86$ $s_2 = 10-100$ cm</p> <p>$f_1 = 351/86$ $s_1 = 5-100$ cm</p> <p>$f_3 = 70/45$ $s_3 = 50-100$ cm</p> <p>270 90 180</p>	 <p>0 (North)</p> <p>$s_1 = 180 \pm 5 / 20 \pm 10$</p> <p>270 90 180</p>

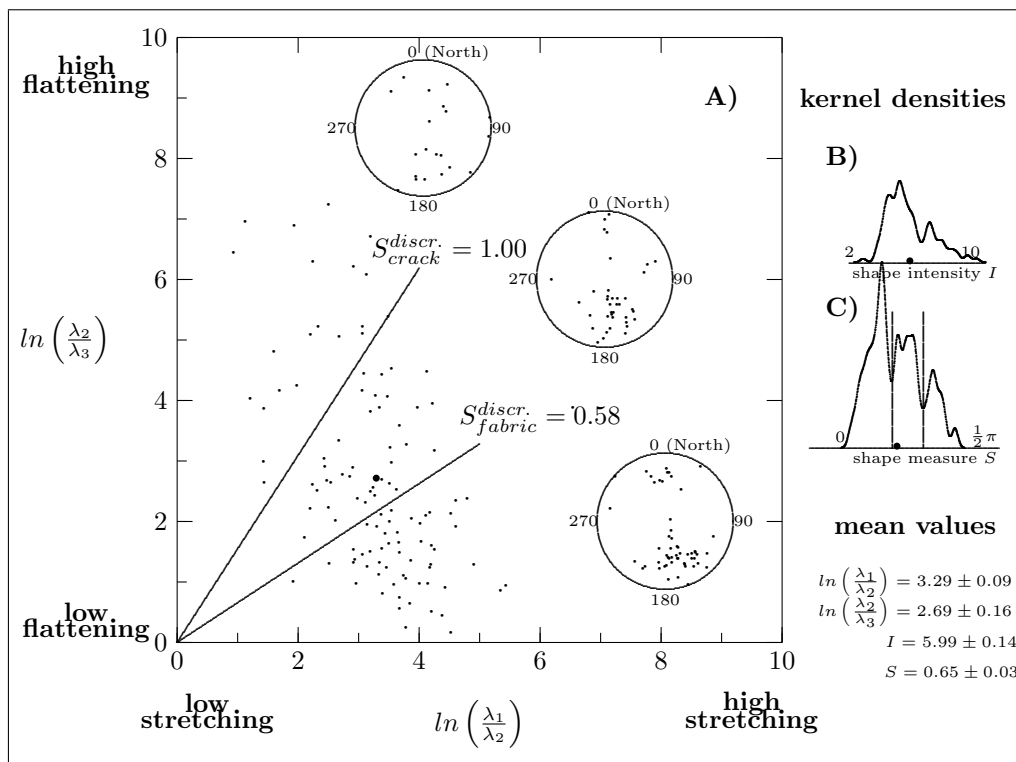


Figure 2.20: Illustration of the polarisation ellipsoids of the S_1 -waves at tunnel meter 1314-1379 m. Picture A) shows the $\ln\left(\frac{\lambda_2}{\lambda_3}\right)$ vs. $\ln\left(\frac{\lambda_1}{\lambda_2}\right)$ cross-plot. The two discriminant functions $S^{discr.}$ in picture A) are derived from the kernel density function in picture C). The stereographic plots show the orientations of the separated displacement ellipsoids.

Table 2.3: Comparison of the mean orientations of the separated and clustered S_1 -wave polarisation ellipsoids with the orientations of the related geological rock mass structures along the profile between 1314-1379 m.

S_1-wave orientations	
transverse isotropy	orthotropy
<p>0 (North) $80 \pm 12 / 70 \pm 6$</p> <p>270 90 180</p>	<p>0 (North) $355 \pm 14 / 22 \pm 6$</p> <p>270 90 180 $161 \pm 10 / 24 \pm 4$</p>
related geology	
fractures	schistosity and lineation
<p>$f_2 = 87/79$ $s_2 > 200 \text{ cm}$</p> <p>0 (North)</p> <p>270 90 $f_1 = 7/84$ $s_1 > 200 \text{ cm}$</p> <p>180</p>	<p>0 (North)</p> <p>270 90 $s_1 = 180 \pm 5 / 10 \pm 10$</p> <p>180</p>

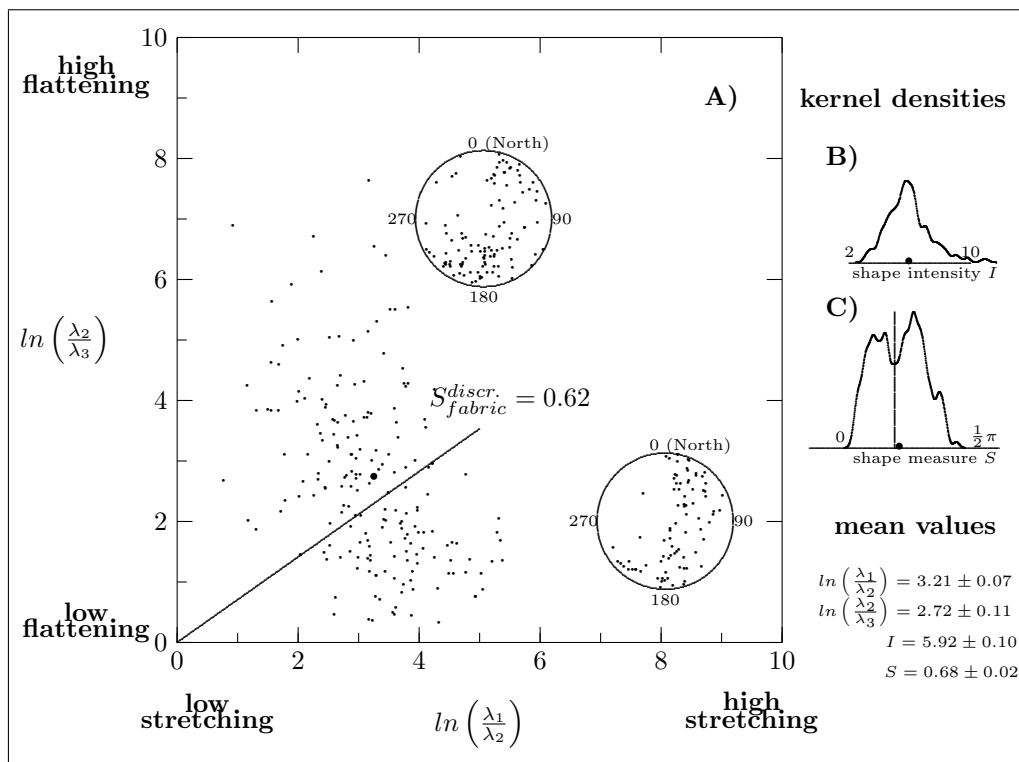
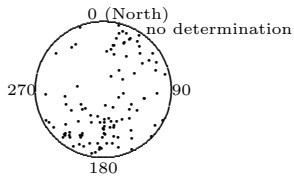
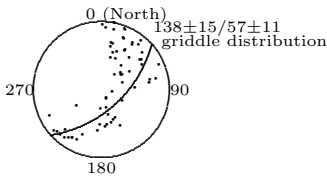
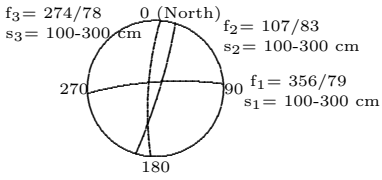
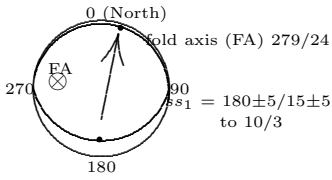


Figure 2.21: Illustration of the polarisation ellipsoids of the S_1 -waves at tunnel meter 1582-1663 m. Picture A) shows the $\ln\left(\frac{\lambda_2}{\lambda_3}\right)$ vs. $\ln\left(\frac{\lambda_1}{\lambda_2}\right)$ cross-plot. The discriminant function $S^{discr.}$ in picture A) is derived from the kernel density function in picture C). The stereographic plots show the orientations of the separated displacement ellipsoids.

Table 2.4: Comparison of the mean orientations of the separated and clustered S_1 -wave polarisation ellipsoids with the orientations of the related geological rock mass structures along the profile between 1582-1663 m.

S_1 -wave orientations	
transverse isotropy	orthotropy
 <p>0 (North) no determination</p> <p>270 90 180</p>	 <p>0 (North) 138±15/57±11 griddle distribution</p> <p>270 90 180</p>
related geology	
fractures	schistosity and lineation
 <p>$f_3 = 274/78$ $s_3 = 100-300$ cm</p> <p>0 (North)</p> <p>$f_2 = 107/83$ $s_2 = 100-300$ cm</p> <p>270 90 $f_1 = 356/79$ 180 $s_1 = 100-300$ cm</p>	 <p>0 (North)</p> <p>fold axis (FA) 279/24</p> <p>270 90 $s_1 = 180±5/15±5$ 180 to 10/3</p>

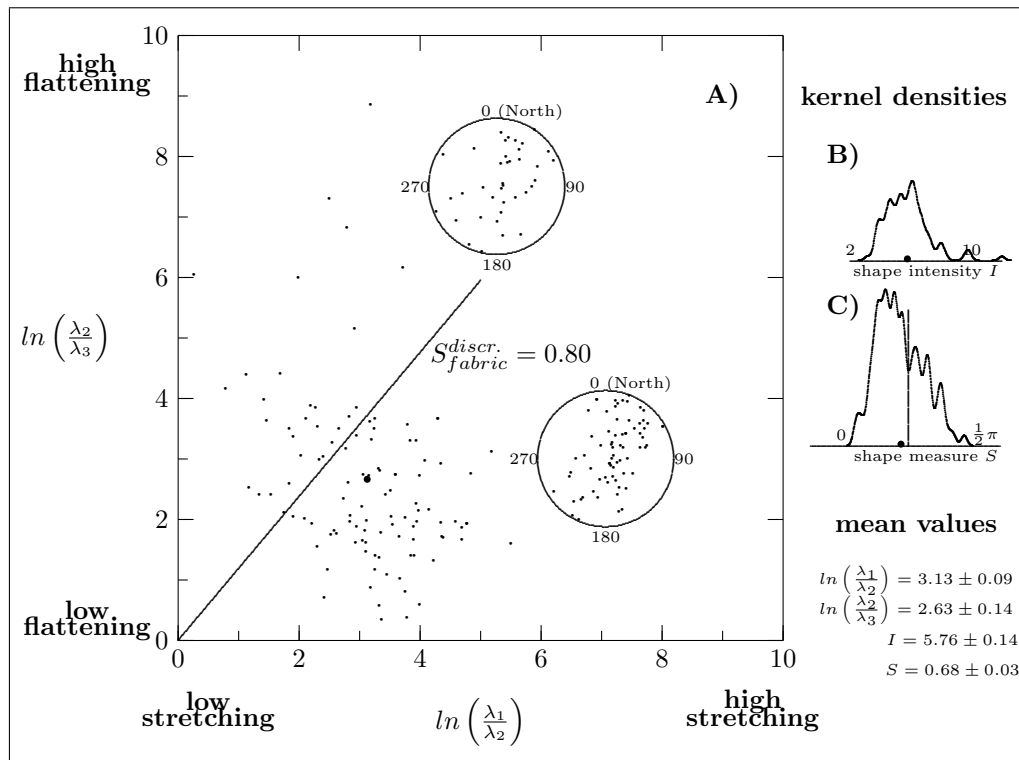
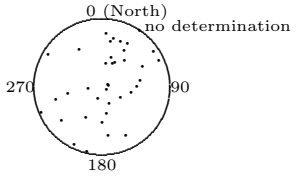
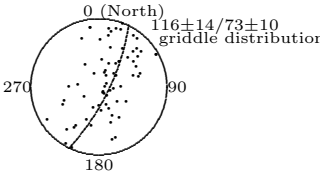
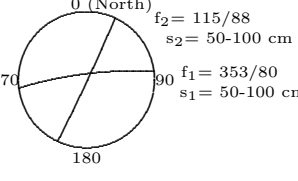
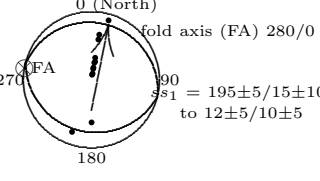


Figure 2.22: Illustration of the polarisation ellipsoids of the S_1 -waves at tunnel meter 1858-1942 m. Picture A) shows the $\ln\left(\frac{\lambda_2}{\lambda_3}\right)$ vs. $\ln\left(\frac{\lambda_1}{\lambda_2}\right)$ cross-plot. The discriminant function $S^{discr.}$ in picture A) is derived from the kernel density function in picture C). The stereographic plots show the orientations of the separated displacement ellipsoids.

Table 2.5: Comparison of the mean orientations of the separated and clustered S_1 -wave polarisation ellipsoids with the orientations of the related geological rock mass structures along the profile between 1858-1942 m.

S_1-wave orientations	
transverse isotropy	orthotropy
 <p>0 (North) no determination</p>	 <p>0 (North) 116±14/73±10 gridlike distribution</p>
related geology	
fractures	schistosity and lineation
 <p>0 (North) $f_2 = 115/88$ $s_2 = 50-100$ cm $f_1 = 353/80$ $s_1 = 50-100$ cm</p>	 <p>0 (North) fold axis (FA) 280/0 $s_1 = 195±5/15±10$ to 12±5/10±5</p>

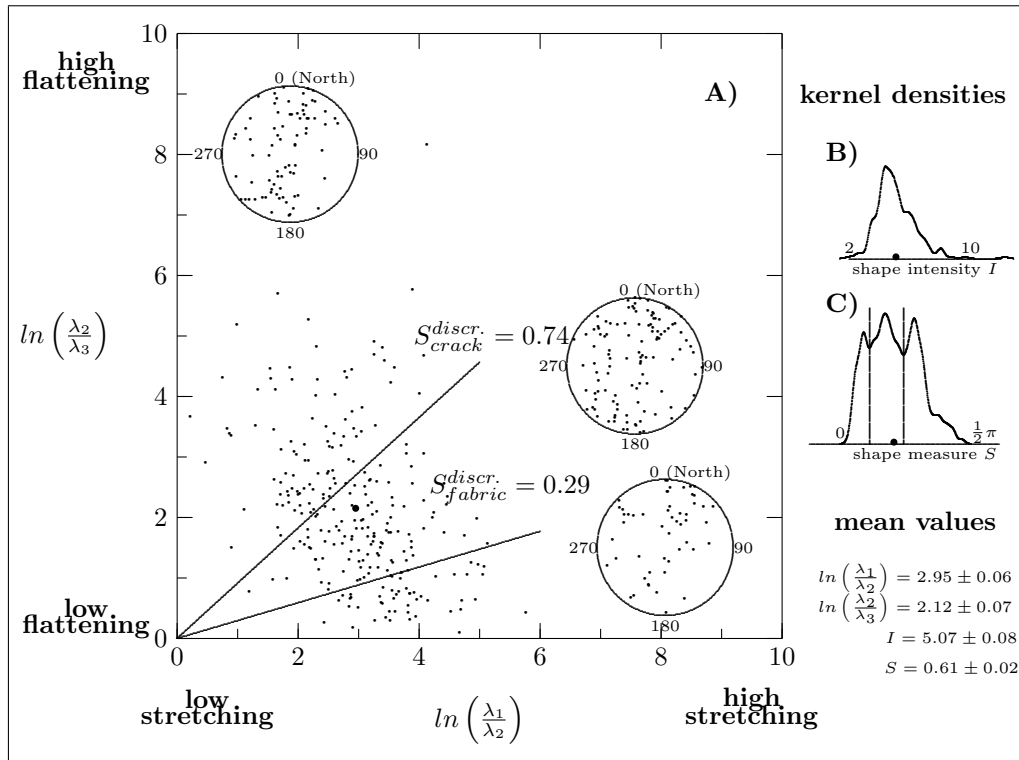
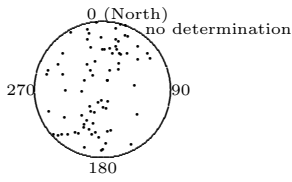
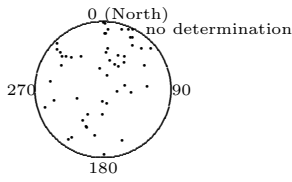
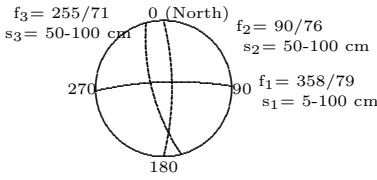
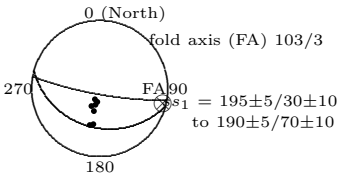


Figure 2.23: Illustration of the polarisation ellipsoids of the S_1 -waves at tunnel meter 2132-2205 m. Picture A) shows the $\ln\left(\frac{\lambda_2}{\lambda_3}\right)$ vs. $\ln\left(\frac{\lambda_1}{\lambda_2}\right)$ cross-plot. The two discriminant functions $S^{discr.}$ in picture A) are derived from the kernel density function in picture C). The stereographic plots show the orientations of the separated displacement ellipsoids.

Table 2.6: Comparison of the mean orientations of the separated and clustered S_1 -wave polarisation ellipsoids with the orientations of the related geological rock mass structures along the profile between 2132-2205 m.

S_1 -wave orientations	
transverse isotropy	orthotropy
	
related geology	
fractures	schistosity and lineation
	

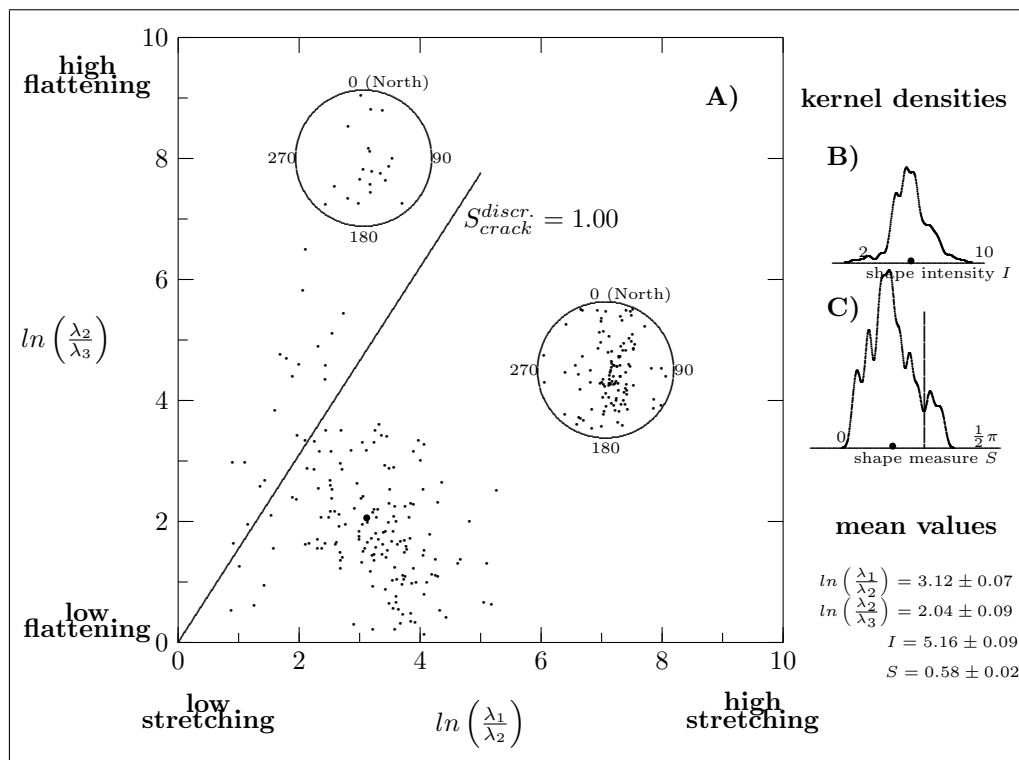


Figure 2.24: Illustration of the polarisation ellipsoids of the S_1 -waves at tunnel meter 2360-2433 m. Picture A) shows the $\ln\left(\frac{\lambda_2}{\lambda_3}\right)$ vs. $\ln\left(\frac{\lambda_1}{\lambda_2}\right)$ cross-plot. The discriminant function $S^{discr.}$ in picture A) is derived from the kernel density function in picture C). The stereographic plots show the orientations of the separated displacement ellipsoids.

Table 2.7: Comparison of the mean orientations of the separated and clustered S_1 -wave polarisation ellipsoids with the orientations of the related geological rock mass structures along the profile between 2360-2433 m.

S_1 -wave orientations	
transverse isotropy	orthotropy
related geology	
fractures	schistosity and lineation

The recognition of the anisotropies depend strongly on the data distributions of the shape measure S . The locations of the classification boundaries $S^{discr.}$ in figure 2.18 A) to figure 2.24 A) are derived from the kernel density distributions of S , as shown in figure 2.18 C) to 2.24 C). The kernel densities are determined by a non-parametric technique of probability density estimation (Silverman 1986). Three or two classes of ellipsoid shapes could be visually extracted for each profile, by finding proper discriminant functions $S^{discr.}$. A predominant anisotropy controls the kernel density function and, hence, the number and the locations of the classification boundaries between different sets of ellipsoid shapes (see figure 2.5). Once a specific class of polarisation ellipsoids is statistically separated from a MA, the mean orientation of the ellipsoids and hence of the structural anisotropy, like fractures and schistositities, can be determined by techniques of spherical statistics (see appendix A). The interpretation of the classification task is outlined in the next section 2.5.

2.5 Discussion and conclusion

It could be shown up in section 2.2, that the shape measure S and the shape intensity I of a shear-wave ellipsoid can be used as good indicators to describe polarised shear-waves.

The classification results of predominant anisotropies and their orientations can be

evaluated by comparing them with the mapped geology. The results of the seismic and geological comparison are summarised in table 2.1 to table 2.7. In the first rows of the tables show the classification results of the observed S_1 -anisotropies. The second rows show the related geology, mapped along the tunnel profiles. The illustrated stereographic plots (equal area) illustrate the mean orientations of the S_1 -wave polarisation ellipsoids, calculated by a grouping method for directional data (see appendix A).

With respect to the in-situ conditions of the measurements within the granitic gneisses, the comparison of the ellipsoid shapes and orientations to the related geology shows generally:

- ductile deformed gneisses with well oriented aligned minerals cause fabric induced shear-wave anisotropy with stretched displacement ellipsoids (orthotropy),
- brittle deformed gneisses with well oriented cracks and fractures cause crack induced shear-wave anisotropy with flattened displacement ellipsoids (transverse isotropy).

That means, the S -values would be low and the I -values would be high in a low fractured and high foliated metamorphic rock with aligned minerals. S increases and I decreases continuously with increasing fracturing in the same rock mass, due to the shear-wave polarisation is disturbed by cracks and fractures, which is physically comprehensible.

Figure 2.25 shows the mean values of the shape parameters of the seven measurement regions, plotted in a $\ln\left(\frac{\lambda_1}{\lambda_2}\right)$ - $\ln\left(\frac{\lambda_2}{\lambda_3}\right)$ cross-plot in figure 2.25 A) and in a S - I cross-plot in figure 2.25 B). The comparison of the mean values is a simple approach to characterise regions of brittle or ductile deformed rock mass. The interpretation of S to characterise the rock mass fracturing is difficult, due to the superposition of all ellipsoid shapes of existent anisotropies, whereas I is stronger influenced by the rock mass fracturing. For example, in low fractured rock mass (mean value of column 3, 4, and 5 of the table in figure 2.25), the S_1 -waves propagate unhindered through the rock and are characterised by high I -values and vice versa (mean value of column 3, 4, and 5 of the table in figure 2.25).

Figure 2.26 shows the relation between the total fracture spacing s_t along the tunnel and the mean I -values, as very rough approximations, of all measured data. $I(s_t)$ converges asymptotically towards an unknown maximum, which is physically reasonable with subject to the scaling effects of the S_1 -wave lengths of approx. 4.8 to 8.8 m, as aforementioned in section 2.4.3. An explanation for this phenomenon is, that if the rock fracturing increases, wave diffractions may increase, which lead to higher λ_3 -values and hence to lower $\frac{\lambda_1}{\lambda_3}$ -ratios and lower I -values of the S_1 -wave motion.

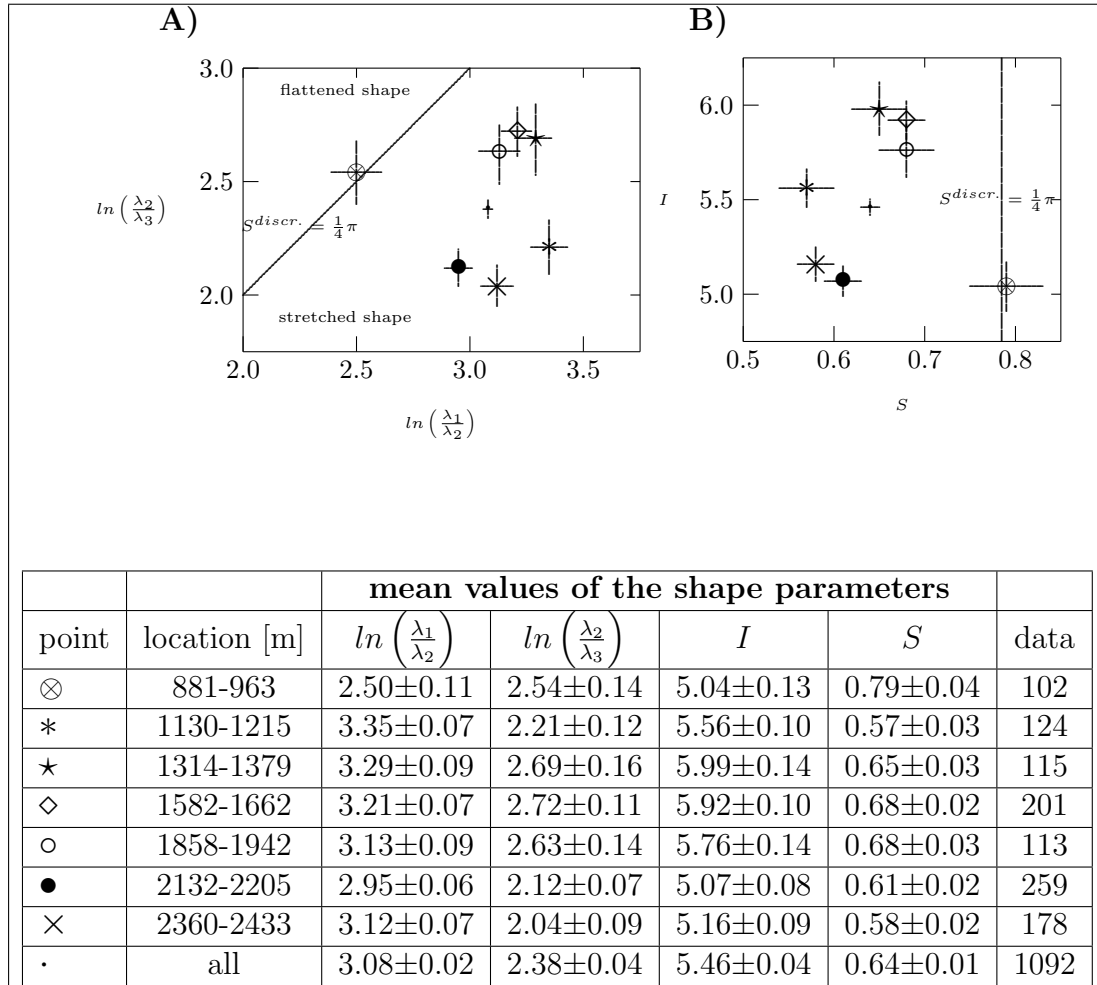


Figure 2.25: Distribution of the MAs mean shape parameters of the S_1 -waves, measured along the seven seismic profiles in the Faido tunnel: picture A) shows the flattening measure $\ln\left(\frac{\lambda_2}{\lambda_3}\right)$ vs. the stretching measure $\ln\left(\frac{\lambda_1}{\lambda_2}\right)$ of the polarisation ellipsoids, picture B) shows the shape intensity I vs. the shaping measure S . Picture B) can be used to determine the predominant anisotropies graphically: high S -values ($S \geq \frac{1}{4}\pi$) and low I -values occur in high fractured and brittle deformed rock mass (⊗), low to moderate S -values and moderate to high I -values occur in very low fractured and/or high ductile deformed rock mass (★, ◇, ○, and *), and low S -values and low I -values occur in partially low fractured rock mass (● and ×).

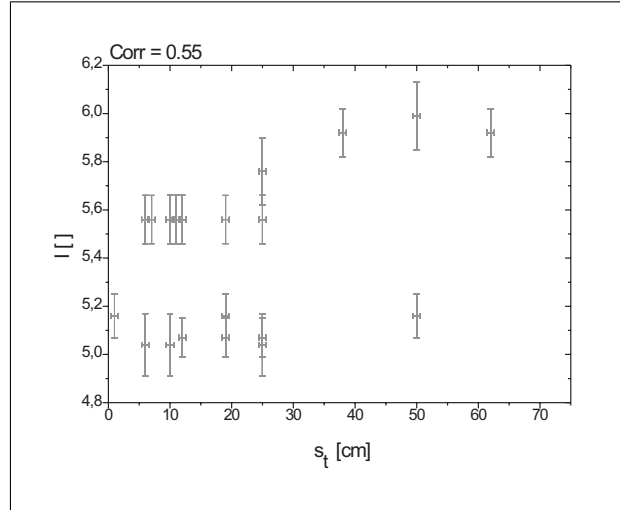


Figure 2.26: Relations (with correlation coefficient $Corr$) between the total fracture spacing s_t and the mean shape intensities I of the S_1 -wave polarisation ellipsoids. The mean I -values are determined along each seismic profile.

Three significant and clear polarisation patterns of different seismic profiles (881-963 m, 1130-1215 m, and 1858-1942 m) will be discussed here.

It can be seen in figure 2.25 B) that the mean value of the shape measure S along the seismic profile between tunnel meter 881 m and 963 m describe qualitatively flattened ellipsoids compared to the stretched ellipsoids along the other seismic profiles. Additionally, the low mean shape intensities I describe weakly polarised shear-waves. This region lies within an approx. 50 m thick fissured zone (damaged zone) of a brittle fault ($\approx 10 - 15$ m thick) with a fracture spacing of $s(f_1) = 5 - 100$ cm, measured along a geological scanline parallel to the seismic profile. The predominant fracture family f_3 influences the S -values and I -values (see figure 2.8 and table 2.1). f_2 occurs with the same fracture spacing $s(f_2) = 20-100$ cm like f_3 . f_1 is equal to the direction of the cataclasite in front of the seismic profile. In figure 2.18 C), the broad kernel density distribution of S (high standard deviation) is remarkable. It accompanies to the high rock mass heterogeneity.

Between 1130 m and 1215 m, the rock mass is moderately fractured, with a fracture spacing of 50 - 100 cm and locally 5 - 50 cm. A mylonitic shear-band occurs with a dipping to 190/30, which is additionally brittle deformed. It has one long open fracture (≥ 7 m) in its center (see figure 2.9). Hence, the distribution of the shape parameters in figure 2.25 shows low mean S -values and moderate mean I -values along this seismic profile. The kernel density distribution of S in figure 2.19 C) is bimodal. Hence, the polarisation pattern of S is separable by a single linear discriminant function $S^{discr.} = 0.68$. It can be seen in table 2.2 that the orientations of the stretched ellipsoids are caused by ductile deformed fine-grained gneiss with well oriented minerals.

Figure 2.25 of the seismic profiles between tunnel meter 1858 m and 1942 m shows a moderate mean S -value, whereas the mean value of I is high. In this area the rock mass is low fractured with a fracture spacing of 100 cm and locally 50 cm, measured along a scanline of the seismic profile. The kernel density distribution of S in figure 2.22 C) is weak bimodal to unimodal. A discriminant function can be defined at $S^{discr.} = 0.80$. The petrology, e.g. the aligned minerals (lineations) parallel to schistosity s_2 , causes the predominant shear-wave polarisation. Thus, the fabric induced polarisation ellipsoids follow the rotation of the schistosity s_2 with the aligned minerals (see figure 2.12) continuously along the profile in the South-limb of a fold in decameter scale, with a fold axis (FA) oriented to 280/0 (see table 2.5). It can be assumed that the two fracture families f_1 and f_2 are responsible for the pattern of the flattened polarisation ellipsoids. The mean ellipsoid orientations can not be determined, due to the high noise of the orientations. This is physically reasonable, because fracture orientations are much more irregular in folded (dm- to m-scale) or plicated (cm-scale and lower) gneisses than in homogeneous gneisses.

The classifications of the ellipsoid shapes to characterise crack and fabric-induced anisotropy are independently done for each of the seven seismic measurements. The separation of the data mainfolds of all MAs show similar discriminant functions. It can be seen that most of the $S^{discr.}$ ranges between 0.62 and 0.8 for 2-class separation (single discriminant function) in figure 2.19, 2.21, and 2.22. The objective linear discriminant function between crack and fabric-induced polarisation ellipsoids is $S = \frac{\pi}{4} = 0.79$ and lies between the determined $S^{discr.}$ -values. For a 3-class separation (two discriminant functions) in figure 2.18, 2.20, and 2.23, $S^{discr.}$ ranges between 1.00 and 1.10 and between 0.41 and 0.58.

It is possible to characterise single crack and fabric-induced shear-wave anisotropies within a mixture of anisotropies (MA) and to determine their orientations, in-situ, in an observed rock mass region by using the new graphical and statistical method, that compares the shape parameters of the S_1 -wave displacement ellipsoids. New shape parameters (stretching $\ln\left(\frac{\lambda_1}{\lambda_2}\right)$, flattening $\ln\left(\frac{\lambda_2}{\lambda_3}\right)$, shape measure S , and shape intensity I) describe the geometry of the polarisation ellipsoids of the S_1 -wave by the axes-ratios. The transformation function $\ln(\cdot)$ is used to define simple and easy understandable parameters to describe ellipsoid shapes. The shape measure S is an essential feature that characterises the shape of an ellipsoid and additionally the geologic-physical reason of the polarisation, i.e. whether shear-waves are fabric-induced polarised with stretched ellipsoids (orthotropy) or crack-induced polarised with flattened ellipsoids (transverse isotropy). The stretched ellipsoids show in direction to the well oriented minerals of the rock mass. The flattened ellipsoids orient in direction parallel to the cracks and fractures. The statistical error of the orientations of crack-induced S_1 -polarisation ellipsoids is much higher than of fabric-induced ellipsoids. In addition, the more homogeneous the rock mass occurs the higher is the shape intensity I . Thus, the mean values of S and I of an observed region characterise whether the geology is homogeneous or heterogeneous and whether the shear-wave anisotropy is crack or fabric-induced or both.

The statistical analysis of the probability distributions of S makes it possible to recognise rock anisotropies. The kernel density distribution of the MA influences

the separation and hence the classification of different anisotropies. The stronger the shape of the bi- or multi-modal density distribution looks like, the better can be found one or more discriminant functions $S^{discr.}$ to separate the two or more classes. Narrow distributions result from homogeneous MA. Broad distributions result from heterogeneous MA, e.g. fracture families that cause high fractured rock mass in broad fissured zones. Hence, the classification quality of different polarisation ellipsoids within a MA depends on the distribution of S . Generally, fabric-induced anisotropy is easier to recognise in the gneissic rock mass than the crack-induced anisotropy. It is a contrary result compared to the arguments of Crampin (1987, 1989) that the EDA mostly dominates. The minerals of the rock fabric support the shape development of S_1 -wave, whereas fractures and cracks disturb the wave propagation.

To evaluate the outlined results, an ongoing research project dealing with finite difference modelling of wave propagations should theoretically confirm the results of this empirical study of in-situ measurements.

3 Classification by conventional methods

The great tragedy of Science -
the slaying of a beautiful
hypothesis by an ugly fact.

(Thomas Henry Huxley)

Klose, C.^(1,2), Loew, S.⁽²⁾, Giese, R.⁽¹⁾, Borm, G.⁽¹⁾

⁽¹⁾ GFZ Potsdam, Geoengineering, Telegrafenberg, 14473 Potsdam, Germany

⁽²⁾ ETH Zürich, Chair of Engineering Geology, Hönggerberg, 8093 Zürich, Switzerland

Article in preparation for submission to
International Journal of Rock Mechanics and Mining Sciences

3.1 Introduction and objectives

Many qualitative characterisations of geological rock mass properties from seismic in-situ measurements are available in the literature. The drawback of seismic in-situ data is that they are complex, noised, and non-linearly related to the geology. Several geological and technical parameters may be related to the noise. These parameters vary simultaneously under in-situ conditions and do not remain controlled, like during laboratory experiments and theoretical modelling. In addition, if the geological measurements are qualitative due to the observers subjectivity or the measurement method, interpretations are difficult. Anyhow, the advantage of in-situ data is that they show up the interdependencies among all measured seismic and geological properties simultaneously. In this article, the metamorphic rock masses of the Penninic gneiss zone in southern Switzerland are characterised from the engineering geological view. The characterisations are based on seismic data interpretations by using conventional methods.

Numerical models have been developed to study the seismic-geological relationships by imaging the real-world in an approximate fashion. Some models are used to calculate the seismic velocities and the Poisson's ratio as a function of the crack density or fracturing. Garbin and Knopoff (1973, 1975), O'Connell and Budiansky (1974) and Henyey and Pomphrey (1982) show self-consistent models of isotropic networks of dry and wet cracks. Garbin and Knopoff and O'Connell and Budiansky outlined, that for dry to partially saturated rock v_P decreases more rapidly with fracturing than v_S . In contrast, for a completely saturated rock, v_S and v_P decrease uniformly, but v_S initially decreases with fracturing about twice as fast than v_P . Additionally, for a saturated rock, Poisson's ratio ν increases when the crack density increases. But ν may go outside the range of reasonable values between 0 and 0.5. In the model of Henyey and Pomphrey, ν is always in this range. Furthermore, the models assume that both the matrix (mineral fabric) and the crack distribution are isotropic and the cracks are smaller than the seismic wavelength. These constraints are not always fulfilled under in-situ conditions.

Crampin (1981), Hudson (1981), and Peacock and Hudson (1990) derived theories for seismic wave propagations in rocks with isotropic and anisotropic distribution of cracks. They outlined that the wave propagation in anisotropic material is fundamentally different from the propagation in isotropic media, although the effects may be subtle and difficult to identify by conventional techniques. Furthermore, there are three body-waves propagating in each direction of phase propagation in anisotropic media: a (quasi) compression-wave (P) and two (quasi) shear-waves (S1 and S2), which have different velocities and mutually orthogonal polarisations and vary with the direction of phase propagation. This phenomenon of the shear-wave splitting in rocks was discovered by Christensen (1966, 1971) and described by the shear-wave velocity anisotropy ξ . ξ is the velocity difference between two shear-waves that are getting splitted and orthogonally polarised from a single initial shear-wave, while propagating along a specific travel path. ξ is minimum if the shear-waves propagate perpendicularly to the plane of structural anisotropy (e.g. single fracture family, foliation). ξ increases in dry rocks to a maximum value, if the shear-waves propagate parallel to the

plane of anisotropy. In saturated rock, ξ increases to a higher value, if the shear-waves propagate with an angle of $\approx 45^\circ$ to the plane of anisotropy and decreases to zero or negative value if the shear-waves propagate parallel to the plane of anisotropy. In addition, ξ increases in dry rock with increasing fracturing and ξ decreases in saturated rock with increasing fracturing.

Many field studies show that interpretations of in-situ data, which are based on one or two seismic parameters, tend to provide results of poor quality. Moos and Zoback (1983) concluded that it is not possible to simply relate fracture density to v_P . Mooney and Ginzburg (1986) could not exhibit a significant reduction of velocities in saturated microcracked and medium fractured rocks. Moos and Zoback (1983) and Stierman (1984) outlined, that also other parameters than the macroscopic fracturing influence the mechanical properties of the rock mass and hence the seismic velocities. Barton and Zoback (1992) and Kuwahara et al. (1995) reported, that only the micro-cracks, which would be non-visible during field work in the tunnel, and not the macroscopic fractures influence v_s . Here, scaling effects should be taken into account. Sjøgren et al. (1979) described that a strong correlation between v_P and fracturing exists within in-situ analysed homogeneous Scandinavian igneous rocks. The correlation quality is better for more competent rock mass. The relationships do not only relate to an average value of fracturing. They also include the effects of other factors such as rock type, mineral content and water content. Greenhalgh et al. (2000) also concluded that engineering geological interpretations of tomograms, which were carried out in the Kambalda nickel mines of western Australia, are problematic, because velocities do not change only due to different rock types and mineralisations. They can also be caused by alteration and weathering. Other relevant influences are Excavation Disturbed Zones (EDZ) due to the disturbance of the ambient stress field (e.g. Wright et al., 2000, Emsley et al., 1996) and disturbances caused by the excavation process (e.g. Bossart et al., 2002).

Two additional seismic parameters are used to characterise the in-situ geological conditions: the shape measure S and the shape intensity I of the S_1 -waves polarisation ellipsoids, which are introduced in chapter 2. The new shape parameters are based on a simple and mathematical self-consistent approach to describe motion ellipsoids graphically and statistically. The shape measure S is a feature that characterises the shape of a polarisation ellipsoid. Stretched ellipsoids, which are predominant in the analysed granitic gneisses, are induced by fabric orthotropy and flattened ellipsoids by the transversal anisotropy caused the cracks. Stretched ellipsoids have the longest axis parallel to the direction of the aligned minerals in the rock mass. Flattened ellipsoids are oriented in direction parallel to the cracks and fractures. The less disturbed the rock mass is, the higher is the shape intensity I . Thus, the mean values of S and I along a seismic profile indicate, whether the geology is homogeneous or heterogeneous and whether the shear-wave anisotropy is crack or fabric induced or both. The technique outlined in chapter 2 is able to detect different anisotropy directions within a Mixture of Anisotropies (MA) that exists in the rock mass.

GeoForschungsZentrum Potsdam has developed an Integrated Seismic Imaging System (ISIS) (Borm et al. 2001 and Giese et al. 2003) which aims at imaging small-scale hazardous geotechnical structures simultaneously during the excavation process in two

different ways: in front of the underground excavation, using reflection seismic techniques and along the excavation walls, using tomographic inversion techniques. The latter provides information of the ambient volume around the tunnel. In this paper, tomographic data are used to classify geological rock mass properties. For this purpose, GeoForschungsZentrum Potsdam carried out seven seismic profiles along the Faido adit of the Gotthard base tunnel, whereby the phase propagations are imaged in 2-dimensional tomograms along scanlines parallel to the left tunnel wall. The Faido adit is an access tunnel to the Gotthard base tunnel, which is a part of the Alp-Transit project. For this in-situ study, the seismic parameters v_P , v_S , ν and ξ are measured along the Faido adit. With the focus to qualitatively understand the seismic data of the Faido tunnel, the interdependencies between seismic and geological rock mass properties are explored with reference to the high noise, the complexity of the data, and to the nonlinear interdependencies of the seismic properties under changing geological in-situ conditions.

The article is organised as follows: section 3.2 and 3.3 give an overview about the in-situ geological conditions and seismic data acquisition and processing. The interdependencies as derived from conventional methods are discussed in section 3.4 and the conclusions are summarised in section 3.5.

3.2 Geology of the Faido tunnel

3.2.1 Overview

The Faido adit is located within granitic gneisses of the Penninic gneiss zone in southern Switzerland. The Leventina gneisses and the Lucomagno gneisses divide the Penninic gneiss zone into a southern and a northern part. The gneisses represent multiple deformed and metamorphically overprinted rocks with complex boundaries (Casasopra 1939, Pettke and Klaper 1992, Ettner 1999). The boundaries between the gneiss complexes are complicated and overprinted by isoclinal folds. Figure 2.7 B) shows a geological map and figure 2.7 C) shows a cross section of the geological situation along the Faido tunnel.

Gneiss varieties of granitic composition characterise both rock complexes. The Leventina nappe is constituted by orthogneisses with laminated, augen-structured, and plicated fabric structures. It consists of (Schneider 1993):

- quartz (25-43%)
- feldspar (38-60%)
- mica (9-24%)
- accessories (1-5%).

Generally, Leventina gneiss varieties show flow structures with well aligned feldspar minerals (Casasopra 1939, Schneider 1993). Two penetrative schistositys, called ss_1

and ss_2 , exist within the Leventina gneiss. The dipping of the older ss_1 -schistosity is generally 10 - 30° to the North (0°). ss_1 is not visible at the macro scale in the Leventina gneisses along the Faido tunnel. During the Alpine evolution, ss_2 , whose dip direction is oriented 10 - 30° to the South (180°), overprinted and folded ss_1 irregularly. ss_2 is characterised by parallel mica minerals in schistic gneiss varieties and by the aligned quartz and feldspar minerals in augen-structured, laminated and plicated gneiss varieties. Casasopra (1939) showed that feldspar minerals ly parallel to the direction of ss_2 . Stretched feldspar minerals occur in laminated, and plicated gneiss varieties, whereas minerals are less aligned in regions of massive gneisses. At the Leventina/Lucomagno nappe boundaries, both the lithological banding and the ss_2 dip angle range from shallow to almost 90°.

The Lucomagno nappe is constituted by coarse and fine grained ortho- and paragneisses with augen-structured and plicated fabric structures. The orthogneisses consist of (Schneider 1993):

- quartz (20-55%)
- alkali-feldspar (0-45%)
- plagioclase (0-70%)
- muscovite (0-20%)
- biotite (0-6%).

The paragneisses show the following rock composition (Schneider 1993):

- quartz (20-70%)
- plagioclase (10-35%)
- biotite (3-30%)
- sericite, muscovite (0-30%)
- garnet (0-15%).

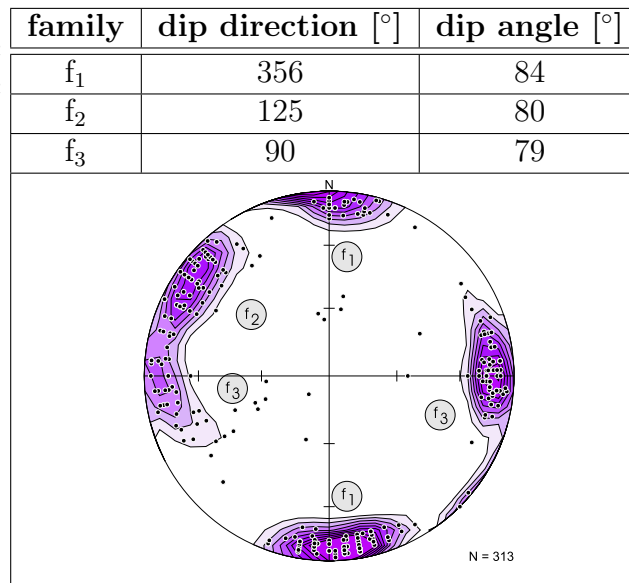
In the Faido tunnel, the Lucomagno gneiss shows a ss_2 -orientation with a dip angle of 70-90° to the South (180°). The Lucomagno gneiss occurs between tunnel meter 2024 m and 2150 m. It can be assumed, that the interpreted geological tunnel profile of the general geology, which is schematically illustrated in figure 2.7 C), cuts across a isoclinic fold. Figure 2.8 to figure 2.14 show seven vertical geological profiles with the extensions of the seismic profiles in the Faido tunnel.

Due to the multiple and strong overprints of the Alpine evolution, the gneiss varieties are dissected by discordant/concordant, folded/unfolded quartz and biotite lentils and veins. Additionally, the gneisses are disturbed by joint sets, fissured zones, and brittle faults. Three major fracture families f_1 - f_3 build up the different joint sets and fissured

zones. Long macroscopic fractures are studied along the Faido access tunnel. The existence of (micro)cracks is not taken into account. The direction of the steep oriented f_1 fracture family is equal to the main direction of geotechnically problematic brittle faults. Table 3.1 shows an equal area contour plot of the major fracture families.

Brittle fault cores occur as cataclasites (coarse grained brittle faults) or fault gouges (fine grained brittle faults) (Passchier and Trouw 1996). Generally, two disturbed zones characterised by low fracture spacing bound a fault core. These disturbed zones are often called damaged zones (Chester and Logan, 1986, 1987, Caine et al., 1996, and Schulz and Evans, 2000). In the Faido tunnel fractures within the disturbed zone form small fissured zones composed of a single joint set. The fracture density increases irregularly from the boundary of a disturbed zone into the direction of the fault core (see figure 3.13 and 3.14). The thickness and the internal structure of brittle faults vary laterally within a wide range. Along the Faido tunnel, one huge fault zone occurs at tunnel meter 960 - 995 m (see figure 2.8 and 3.13). An approx. 30 cm thick cataclasite occurs at 2410 m (see figure 2.14 and 3.14). In general, the smaller the fault core is, the smaller are the disturbed zone characterised by low fracture spacings. Hence, it can be assumed that the larger the disturbed zones is, the earlier the fault core can be detected along a seismic profile crossing the fault. This is an additional important information useful to predict hazardous fault zones ahead the face of an excavated tunnel.

Table 3.1: Contour plot of the three major fracture families (pole vectors) that occur in the Levantina and Lucomagno gneisses. The Faido tunnel is NE-SW oriented.



The brittle fault structures are critical for the water transport within the rock mass and instable tunnel sections (over-breaks, face collapse, squeezing ground). Regions with higher water inflow are related the disturbed zones around brittle faults at 970 m, and 2410 m (see figure 3.13 and 3.14). The inflow reaches maximum values up to 0.1 l/s (720 m, 990 m) and 0.25 l/s (2040 m) (see figure 3.1). Along geological scanlines parallel to the seismic profiles, the water inflow can be characterised mostly as "dry" and partially as "dripping" using the classification scheme of Bieniawski (Bieniawski, 1989).

3.2.2 Geological rock mass properties

The geological data were mostly semi-quantitatively acquired in the 2600 m long and up to 1400 m deep Faido tunnel during the tunnel excavation. The adit is 12% inclined and has a radius of 5 m. Sketches of the tunnel faces, called tunnel face maps, were generated. Phenomenological homogeneous areas of each geological features are determined in direction parallel to the seismic profiles. An homogeneous area of a geological feature is a tunnel segment of a certain length. The distances of the tunnel locations of the face maps vary between 1 and 20 m. The distances are larger in regions with high rock mass qualities than in regions with low qualities. The gneiss varieties and the water inflow Q into the tunnel were derived from the face maps. Other geological parameters were sampled along the left tunnel wall, like fracture spacing and the orientation of the schistosity (dip direction/dip).

Eight geological features that may influence the propagation of seismic waves were used for further analyses. Geological feature vectors $\{\sigma_c, Q, s_t, p, e, r, f, ss\}$ can be defined for a specific tunnel location as follows: σ_c the uniaxial compressive strength measured perpendicular to the schistosity (quantitative), Q the water inflow into the tunnel (semi-quantitative), s_t the total fracture spacing (quantitative), p the fracture persistence (semi-quantitative), e the fracture aperture (semi-quantitative), r the fracture roughness (semi-quantitative), f the fracture infilling (semi-quantitative) and ss the schistosity dip angle (quantitative). All fractures are unweathered along the profiles, so parameter *weathering* is neglected.

The information of the gneiss varieties were used to determine the uniaxial compressive strength σ_c of the gneisses at the specific tunnel positions. σ_c -values measured perpendicular to the schistosity with ($71 \leq 144 \pm 45 \leq 209$) MPa are preferred for further calculations compared to those parallel to the schistosity with ($74 \leq 119 \pm 25 \leq 152$) MPa, because they have a much higher variability and hence contain more information on σ_c in general. Relationships between σ_c and the gneiss varieties were determined during the excavation of 'Piora' exploration tunnel (Schneider, 1997). Here, σ_c was measured as a function of the Leventina (LeG) and Lucomagno (LuG) gneiss varieties: laminated LeG (209 ± 17 MPa), augen-structured to porphyric LeG (114 ± 35 MPa), porphyric to schistic LeG (149 ± 70 MPa), schistic LeG (186 ± 41 MPa) and porphyric biotite-rich LuG (75 ± 20 MPa). The relations are used to estimate σ_c -values of the rocks in the Faido tunnel as follows (see eq. 3.1). A σ_c -value at an observed location is the harmonic mean of the σ_c -value (defined as σ) of each gneiss variety l ($l = 1, 2, \dots, 5$) and its percentage of occurrence a_l (area in a face map) at this tunnel position:

$$\sigma_c = \frac{\sum_{l=1}^5 a_l \sigma_l}{\sum_{l=1}^5 a_l} \quad (3.1)$$

Thus, only approximated σ_c -values could be derived. For a qualitative rock mass characterisation approximations are good enough, because the σ_c -values vary slightly in similar gneiss varieties and strongly among different varieties. Additional information of the gneiss structure were acquired by the spatial orientation of the schistosity. The dip angle ss of the macroscopic schistosity was determined quantitatively along the left tunnel wall within homogeneous regions.

The normal fracture spacings s of the three main fracture families within homogeneous regions were continuously determined along the left tunnel wall. But, the data of the fracture families is of less quality - the acquisition was done under in-situ conditions during the excavation process. The normal fracture spacings of each fracture families is used to calculate the total fracture spacing s_t (e.g. Priest, 1994) as follows:

$$s_t = \frac{1}{\sum_{k=1}^3 \frac{1}{s_k}} \quad (3.2)$$

where s_k is the spacing of fracture family $k = 1, 2, 3$, measured along the left segment of the tunnel (homogeneous region). $\frac{1}{s_k}$ describes the linear fracture frequency (e.g. Priest, 1994).

Additional fracture parameters like the fracture persistence p , aperture e , roughness r and infilling f were semi-quantitatively determined along the left tunnel wall. The quality of these parameters is very poor, because these parameters were later determined independently from s_t and the outcrop quality of the advanced tunnelling process was poor too. p is not the absolute length of a fracture, because the length can not be directly determined in a tunnel. In this thesis, p is defined as the average length of the traces (harmonic mean) of the three main fracture families with subject to the fracture frequency $\frac{1}{s_k}$. The average p -value describes a homogeneous region and is determined as follows:

$$p = \frac{\sum_{k=1}^3 p_k \frac{1}{s_k}}{\sum_{k=1}^3 \frac{1}{s_k}} \quad (3.3)$$

where p_k is the persistence of the fracture family $k = 1, 2, 3$ within the segment of the tunnel (homogeneous region) in which s_k is determined as well. The parameters e , r , and f are determined after the same scheme of eq. 3.3. These parameters have to be understood as very roughly approximated values, due to the fact that more detailed data of better quality were not available during the tunneling process. The fracture roughness r could be described by only 2 ("very rough" and "rough") of 5 possible classes ("very rough", "rough", "slightly rough", "smooth", "slickensided"). Two classes could also be determined for the fracture infilling f ("none" and "hard infilling < 5mm") of 5 possible classes ("none", "hard infilling < 5mm", "hard infilling > 5mm", "soft infilling < 5mm", "soft infilling > 5mm"). p , e , r and f can only be used as semi-quantitative properties of the rock mass along the Faido tunnel.

The water inflow Q into the tunnel was directly outlined in the tunnel face map descriptions and was used to determine homogeneous Q -regions. Q can be characterised by 5 classes "dry", "damp", "wet", "dripping" and "flowing". Only 2 classes ("dry" and "wet") occurred along the left tunnel wall, whereas more classes were mapped along the rest of the Faido tunnel. It is known that the seismic velocities are also a function of water saturation. However, the parameter water inflow Q can only be used to describe the inflow into the tunnel but not the degree of saturation. The rock mass with a "dry" water inflow is only unsaturated or partially saturated close (cm - dm) to the tunnel surface i.e. due to the tunnel ventilation (Marshall et al. 1999). In greater depth, especially where the seismic properties have been determined, the rock mass is totally saturated. For the characterisation of the parameters Q , p , e , r and f the

same classes were used as in the characterisation scheme of Bieniawski (1989). Other systems can be used as well but would provide similar results.

The geological features within each phenomenological homogeneous unit are regionalised with reference to a 50 cm grid point spacing, which is the size of the sampling grids (50×20 cm) in the tomographic images (see section 3.3.2). The regionalisation is a simplification; when specific geological properties describe an homogeneous unit, it can be assumed that all locations in this unit are characterised by this properties as well. Figure 3.1 shows the data distributions of geological features along the tunnel profiles. The vertical lines in figure 3.1 indicate observed fault and fracture zones along the Faido tunnel. The rock mass properties will be discussed in section 3.4 together with the seismic properties that are outlined in the next section 3.3.

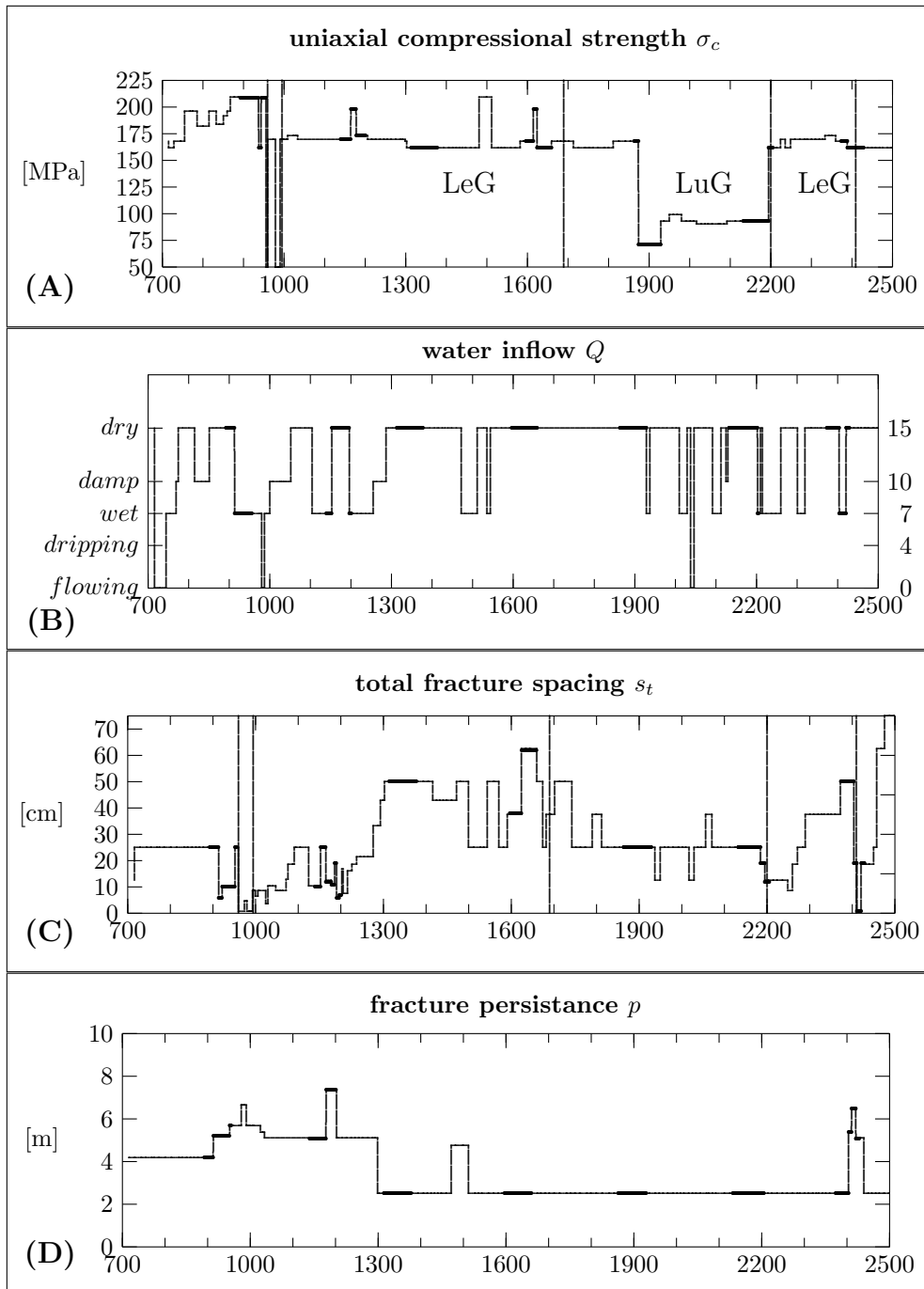


Figure 3.1: Spatial distribution of the geological rock mass properties along in the Faido tunnel. The thicker lines marke the property distribution along the seismic profiles. The vertical lines indicate fault zones between 960-995 m and at 2410 m and fractured zones at 1690 m and 2200 m. Continuation next page.

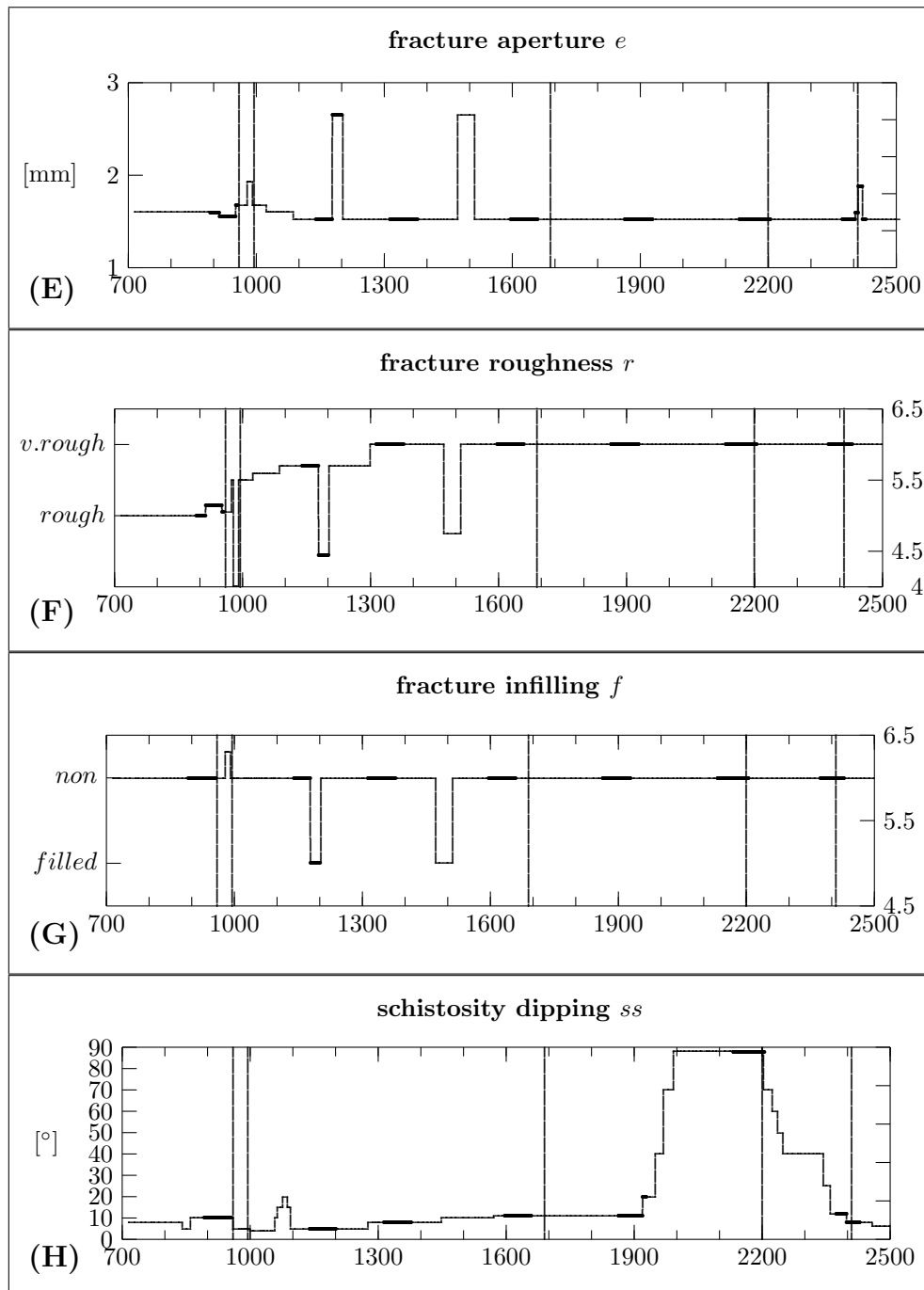


Figure 3.1: Spatial distribution of the geological rock mass properties along in the Faido tunnel. The thicker lines marke the property distribution along the seismic profiles. The vertical lines indicate fault zones between 960-995 m and at 2410 m and fractured zones at 1690 m and 2200 m.

3.3 Seismic data acquisition

3.3.1 Seismic in-situ measurements

The technical equipment of ISIS of the GeoForschungsZentrum consists of mainly two components: three component geophones as seismic receivers and a mechanical hammer as acoustic source.

Receivers

Rock anchors increase the stability of a tunnel opening through strengthening the rock cohesion. Thus, ISIS uses the anchors as safety elements as well as seismic antennas. Geophones, mounted in three orthogonal directions at the head of an anchor, detect the full seismic wave field up to 3 kHz. The 2 m long anchors are cemented in boreholes with standard two component epoxy resin, which guarantees an optimum coupling of the geophones to the surrounding rock. Properly oriented, the receiver rods span a linear horizontal geophone array along the tunnel wall (see figure 2.16).

Acoustic source

ISIS uses a repetitive mechanical hammer as seismic source. The hammer incorporates a pneumatic cylinder. A moving mass of 5 kg supplies the power for the impacts bedded on rollers inside the conduct tube. A programmable steering unit controls the impacts of 1 ms. Prior to the impact, the hammer is prestressed towards the rock with a force equivalent of 200 kg. The prestress guarantees an optimum coupling of the hammer and the rock. The impact hammer could be used in all directions in combination with a tunnel boring machine (TBM) or other construction machines. The hammer transmits impulse signals up to frequencies of 2 kHz with a repetition rate of 5 s. Therefore, a couple of impacts can be shot within a few minutes. The maximum trigger error is less than 0.1 ms. This small time delay, together with the excellent consistency of the transmitted signals at each source point, leads to a significant enhancement of the signal-to-noise ratio by using vertical stacking. Vertical stacking is a known statistical procedure to enhance correlated signals, like reflections from discontinuities, and to reduce non-correlated signals like noise from the drilling process (TBM or Drill/Blast).

Geometry of the seismic profile

Seven approx. 70 m long seismic profiles of source points and geophone anchors were aligned less than 10 m behind the advancing tunnel face with a spacing of about 200 m measured along the tunnel wall simultaneously during the tunnel excavation between 880 m and 2440 m (see figure 2.8 - 2.14). Usually, an array of 8 to 10 geophone anchors with a spacing of 9 m were installed for a single seismic profile. Figure 2.16 illustrates schematically the configuration of the seismic measurements. One of the anchors is positioned at the opposite wall of the tunnel to control several guided waves along and around the tunnel surface. The spacings of source points are usually 1.0 m to 1.5 m. The source points are set at the left hand side of the tunnel.

3.3.2 Seismic data processing

Seismic techniques image only the elastic properties of the rock mass. These properties depend on the rock type, porosity, fracture distribution, and fluid content of the rock mass. As stated previously in section 3.3.1, ISIS uses seismic travel time inversion tomography to image the tunnel near-field during the excavation. Here, the results of the seismic travel time inversion tomography of direct P and S wavefields will be analysed and discussed. Travel time tomographic inversions of the 7 measurement profiles were generated as horizontal planes, spanned between the geophone anchors and the source points, close to the left tunnel wall (see figure 2.16 and appendix B).

The arrival times of the direct compression-waves (P) and the two direct shear waves (S_1 and S_2) are used for calculations of the velocity field tomographic inversions. A ray tracer software of a commercial software package, called ProMAX, is used for the calculation of the tomograms. For the P- and S-waves of each seismic profile, 5 tomograms with 5 different grid sizes (4×1 m, 8×2 m, 12×3 m, 16×4 m, and 20×5 m) were calculated by procedures for travel time inversion. The sampling error for the first arrival times is $1/32 \cdot 10^{-3}$ s. The smaller the grid size of a calculated tomogram is, the higher is the image resolution but the lower is the ray path density of the waves crossing the grids. The near field of the tunnel is better displayed when small grid sizes are used and vice versa. High grid sizes can lead to unstable inversion results. The ray path density z describes the certainty of the velocity v at a grid point. z lies between 0 (uncertain) and 1 (certain).

The procedure to generate the tomographic images for each direct wave field is

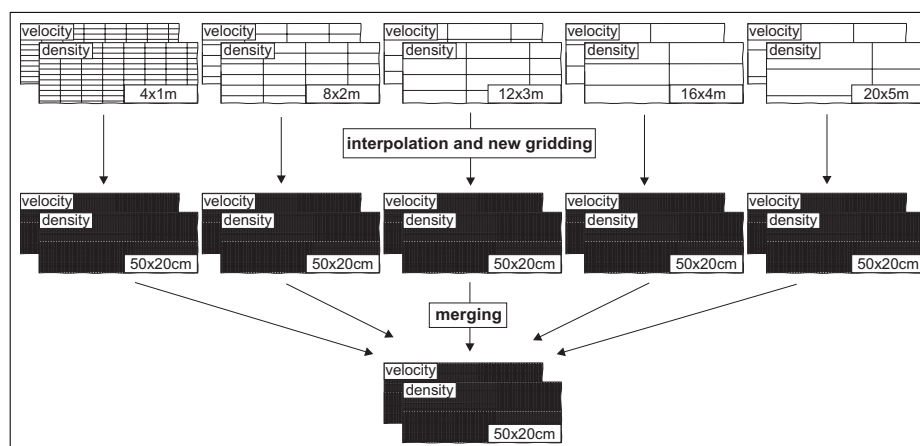


Figure 3.2: Illustration of the procedure to generate the seismic tomograms. First, for both the compression-waves and the two shear-waves, there are five different tomogram-grid sizes with respect to the tomogram resolution and quality. Second, each tomogram is interpolated. The interpolation grid size is equal for all tomograms. The tomograms i can be merged with respect to the velocity values v_i and the path density values z_i .

illustrated in figure 3.2. In order to get a more generalised tomogram, all 5 original tomograms are merged for one wave field as follows:

1. each tomogram is interpolated and the velocity values are extracted from a homogenised lattice with a grid size of 50×20 cm and
2. the harmonic mean of the velocities

$$v = \frac{\sum_i v_i z_i}{\sum_i z_i} \quad | \quad i = 1, 2, \dots, 5 \quad (3.4)$$

is calculated for each grid point within the lattice.

It should be noticed, that "too small" as well as "too large" grid sizes lead to tomographic images with artificial errors (heterogeneities, aliasing), due to numerical instabilities. The outlined generalisation procedure is neglecting the existence of these errors. The procedure only merges different image resolutions with respect to their grid sizes. The influence of the errors can only be reduced by analysing image regions with higher z -values, where numerical instabilities can be neglected. Further, the information on of the rock mass, provided by the refraction tomograms, are limited, because the source/receiver geometry is 2-dimensional and linear. Linear means that the source points and the receivers lie along a line of a 2-dimensional plane (see figure 2.16). Direct waves propagate away from the source points on the tunnel surface into the depth before they reach the receivers. The waves are refracted due to the high radial velocity gradient in the nearfield around the tunnel. The angle between the tomographic plane and the migration direction of a single wave (incident angle), see figure 2.16, is lower than 10° degrees.

The seismic features are acquired from the tomographic images. Appendix B shows the tomograms of the v_P , v_S , ν and ξ for each seismic profile. The Excavation Disturbed Zone (EDZ) around a tunnel causes high velocity gradients (see figure 3.3).

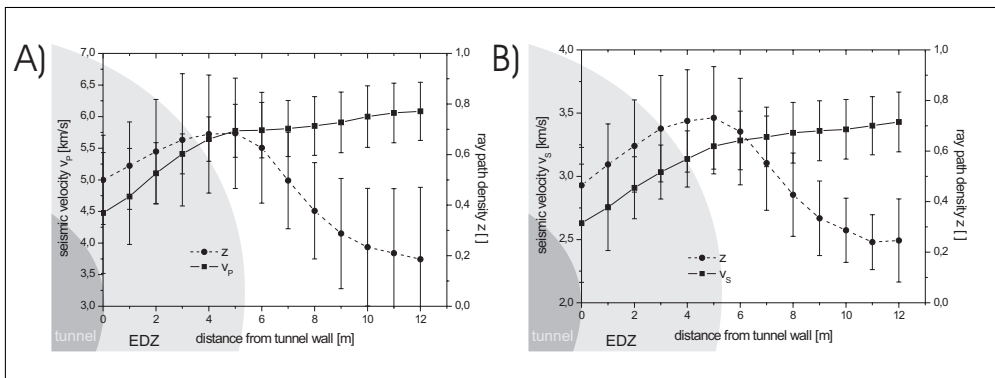


Figure 3.3: Illustration of the spatial radial distribution of real measured velocity values v_P , v_S and the ray path density values z around the tunnel and the Excavation Disturbed Zone (EDZ). z is an indicator for the accuracy and precision of the velocity values v at each grid point. Generally, z reaches its maximum values at a depth of a tunnel radius.

This gradient is a precondition to calculate the tomograms along the seismic profile. The EDZ in the Faido tunnel is mostly generated by opening of existing and new cracks or fractures due the stress redistribution and the excavation process. The EDZ causes the high variability of the seismic velocities, see appendix B.

It is important to find areas of representative data within the tomograms that show undisturbed geological conditions. The influence of the EDZ decreases from the tunnel wall into the interior of the rock mass, see figure 3.3 and appendix B. At a depth of approx. 5 m (one radius of the Faido tunnel) the influence of the EDZ reaches an acceptable low level. Seismic data are selected every 50 cm (tomogram grid size) along 5 m deep tunnel parallel scanlines (figure 2.16 and appendix B), due to following reasons:

- at that depth the ray path density z is very high (see figure 2.16),
- the seismic features describe the elastodynamic properties of the undisturbed geology in at least 5 m deep regions around the tunnel as shown in figure 3.3,
- the velocity errors are higher for short offsets (near to the tunnel surface) than for long offsets (distant to the tunnel surface) and
- the differences are still small between of the geology in 5 m depth and the geology on the tunnel surface.

Table 3.2: Empirical standard errors of the seismic properties. The errors are statistically calculated and depend on the number n of data points, using $\Delta S = \frac{1}{\sqrt{n}} \sqrt{\frac{\sum (S_i - \bar{S})^2}{(n-1)}}$. Each measurement profile has its specific errors subject to the number of data points that result from tomograms as well as from seismograms.

profile [m]	tomogram data					seismogram data		
	n	$\Delta v_P [\frac{km}{s}]$	$\Delta v_S [\frac{km}{s}]$	$\Delta \nu []$	$\Delta \xi [\%]$	data	$\Delta S []$	$\Delta I []$
892-956	86	0.026	0.015	0.001	0.242	102	0.04	0.13
1140-1201	86	0.032	0.013	0.002	0.118	124	0.03	0.12
1314-1378	87	0.021	0.009	0.004	0.083	115	0.03	0.16
1597-1660	85	0.045	0.016	0.003	0.192	201	0.02	0.11
1864-1929	131	0.018	0.012	0.002	0.200	113	0.03	0.14
2133-2205	146	0.019	0.019	0.003	0.166	259	0.02	0.08
2374-2429	111	0.034	0.025	0.005	0.313	178	0.02	0.09

The seismic feature vectors $\{v_P, v_S, \nu, \xi, S, I\}$ contain the following seismic attributes along each seismic profile: compression-wave velocity v_P , velocity of the first shear-wave v_S , Poisson's ratio ν or velocity ratios v_P/v_S , shear-wave velocity anisotropy $\xi_{(v_{S_1}, v_{S_2})}$ and mean values of the shape measure S and shape intensity I of the S_1 -waves polarisation ellipsoids. The shear-wave velocity anisotropy ξ shows the relative

difference between the leading shear-wave and the second shear-wave velocity as follows:

$$\xi_{(v_{S_1}, v_{S_2})} = \left(1 - \frac{v_{(S_2)}}{v_{(S_1)}} \right) \cdot 100 \% \quad (3.5)$$

Figure 3.4 shows the distribution of the 6 seismic properties along the tunnel profiles in 5 m depth. The vertical lines in the pictures of figure 3.4 illustrate the fault and fracture zones. The properties will be discussed and compared with the geological rock mass properties in section 3.4. The empirical standard errors of the seismic properties within 5 m depth are statistically calculated, as shown in table 3.2.

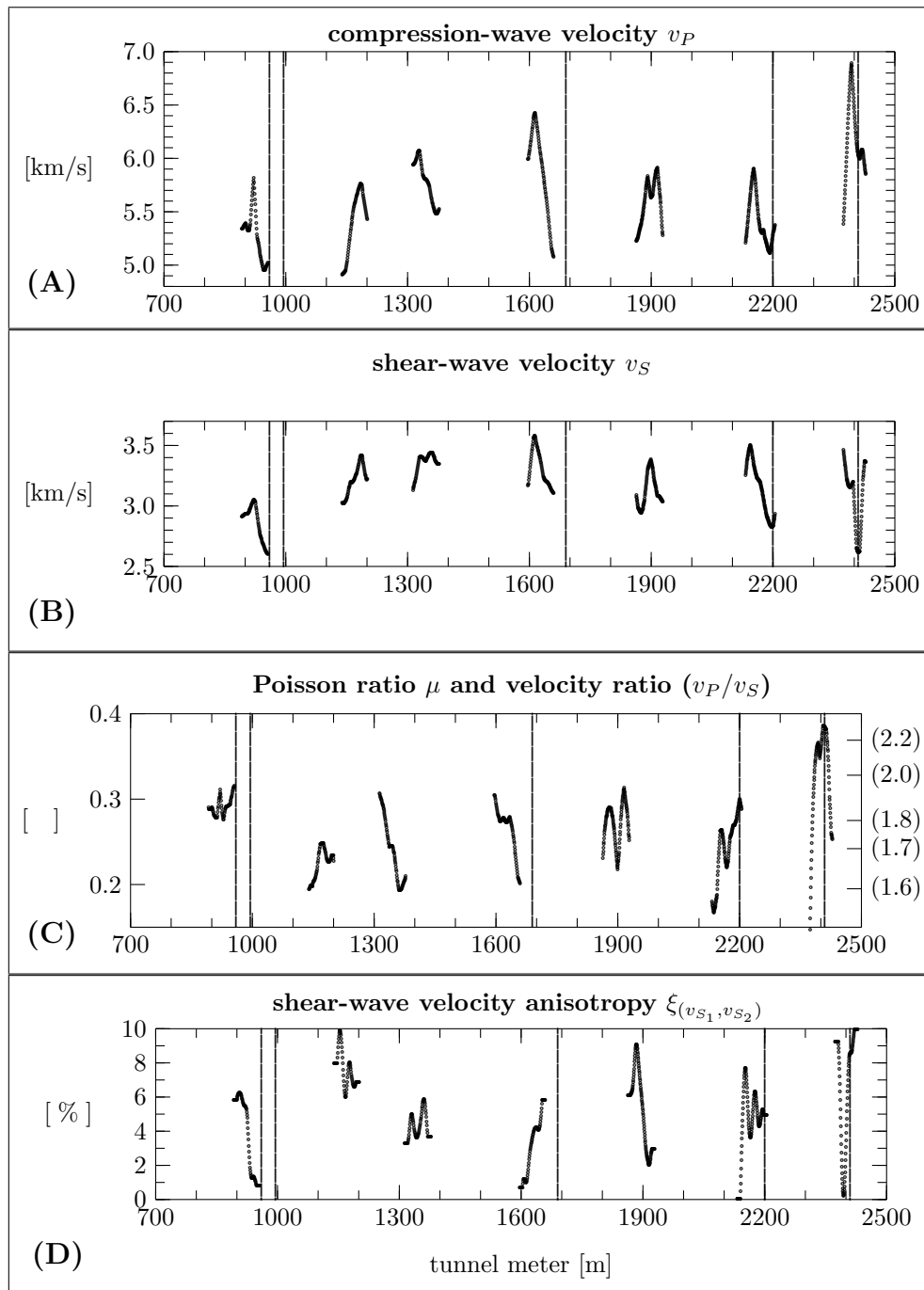


Figure 3.4: *Spatial distribution of the seismic rock mass properties along the 7 seismic profiles in the Faïdo tunnel. The vertical lines indicate fault zones between 960-995 m and at 2410 m and fractured zones at 1690 m and 2200 m. Continuation next page.*

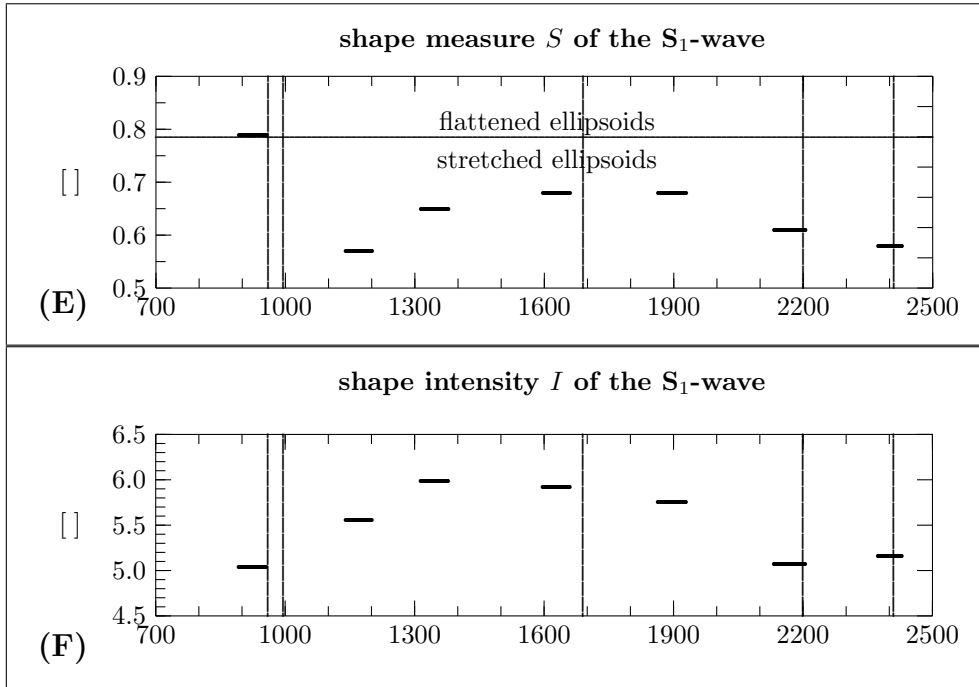


Figure 3.4: Spatial distribution of the seismic rock mass properties along the 7 seismic profiles in the Faido tunnel. The vertical lines indicate fault zones between 960-995 m and at 2410 m and fractured zones at 1690 m and 2200 m.

3.4 Relationships between geological and seismic rock mass properties

Figure 3.1 and figure 3.4 visualise the geological properties and the seismic properties of the rock mass. First, the properties are pairwise compared in cross plots, shown in figure 3.7 to 3.12. Single geological and seismic parameters are discussed in the following sections.

3.4.1 Total fracture spacing s_t

The total fracture spacing s_t is one of the most important geological properties for rock mass characterisation. s_t influences the seismic properties, especially the velocities. The s_t -cross-plots in figure 3.7 show that v_S is more sensitive than v_P , ν , ξ and the shape intensity I (amplitudes) of the S_1 -waves. The velocity values converge asymptotically against maximum values v_S^{max} and v_P^{max} with an increase of s_t . The parameters of the fit functions show, that minimum velocity values $v_{(s_t=0cm)}^{min}$ are $(5.0 \pm 0.3) \frac{km}{s}$ for P-waves and $(2.78 \pm 0.06) \frac{km}{s}$ for S_1 -waves. A similar exponential function can be assumed in the s_t - I cross-plot. It is physically plausible that the intensity of the S_1 -wave

3.4. Relationships between geological and seismic rock mass properties 67

motion ellipsoids decreases with decrease s_t , because the wave polarisation is reduced as the number of discontinuities in the rock mass increase.

Only densely fractured rock masses show significantly reduced velocities proportional to the fracture density as shown between 915 - 950 m and between 2400 - 2420 m in figure 3.4, 3.13, and 3.14. v_S is a better and more robust parameter for in-situ characterisation of the saturated rock mass fracturing than v_P . This can be seen by the correlation coefficients in figure 3.7.

3.4.2 Uniaxial compressive strength σ_c

Further examples show that it is not possible to simply relate s_t to v_P by the in-situ measurements in the Faido tunnel. Other geological parameters may influence the seismic velocities (Moos and Zoback, 1983 and Stierman, 1984). It can be assumed that v_P is influenced by the uniaxial compressive strength σ_c . σ_c -values are very low between tunnel location ≈ 1900 m and ≈ 2200 m, whereas low v_P -values occur in that area. The fractured zone at tunnel location 2200 m with irregularly distributed fracture sets (see figure 2.13), is probably responsible for the decrease of v_P and v_S with very small increases at the end of the seismic profile and an increase of ν (figure 3.4 (A), (B) and (C)), whereas the cross plots of σ_c in figure 3.5 show a weak correlation to v_P and the other seismic parameters. It can be seen, that the interdependencies between σ_c , as a function of the rock composition, and seismic properties are weaker than those between s_t and the seismic properties. Rock parameters like σ_c influences the seismic properties at a larger scale (meters). This can be seen by comparing the tunnel profile of σ_c -values with s_t -values. s_t shows a much higher variability than σ_c , because fracture sets can occur very locally. On the other hand, the mineralogy of the gneisses between 1900 m and 2200 m changes slightly from Leventina gneiss (LeG) to Lucomagno gneiss (LuG) and to LeG again (see 3.1 (A)). The different rock composition influences σ_c .

3.4.3 Fracture persistence p and aperture e

The fracture persistence p and aperture e , which are only semi-quantitatively measured, show low to very low correlation coefficients to the seismic properties (see figure 3.8 and 3.9). The influence of p , e , r , and f to the seismic parameters is much lower than s_t . This can be seen in the cross plots of figure 3.7 and 3.11. The low data quality of p , e , r , and f are most probably a reason of the low correlations.

3.4.4 Schistosity dipping ss

The spatial distribution of the schistosity dipping ss (see figure 3.1 (H)) shows a change from shallow to steep orientation, as mentioned in section 3.2. The mutual angle between S -waves and the orientation of the schistosity influences the wave propagations. The seismic in-situ data do not confirm the results of Crampin (1985, 1990), that the

anisotropy ξ is minimum when the shear-waves propagate perpendicularly to a plane of anisotropy, like schistosity ss , and that ξ increases to a maximum value when the shear-waves propagate parallel to a plane of anisotropy. The schistosity dipping ss besides other geological parameters influences the seismic rock mass properties less than s_t .

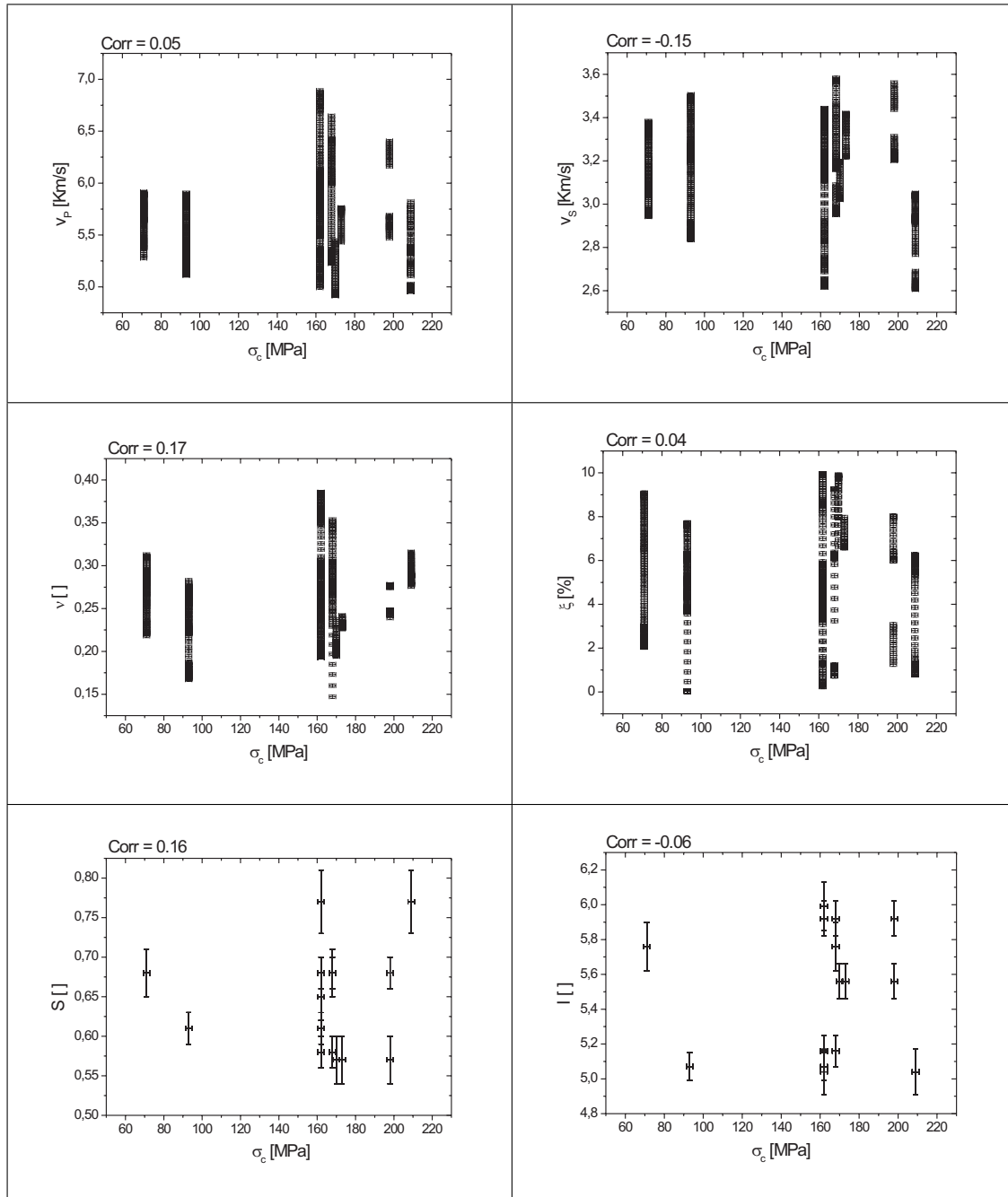


Figure 3.5: Cross plots and correlation coefficients $Corr$ of the seismic rock mass features v_p , v_s , ν , ξ , S and I vs. uniaxial compressional strength σ_c .

3.4. Relationships between geological and seismic rock mass properties 69

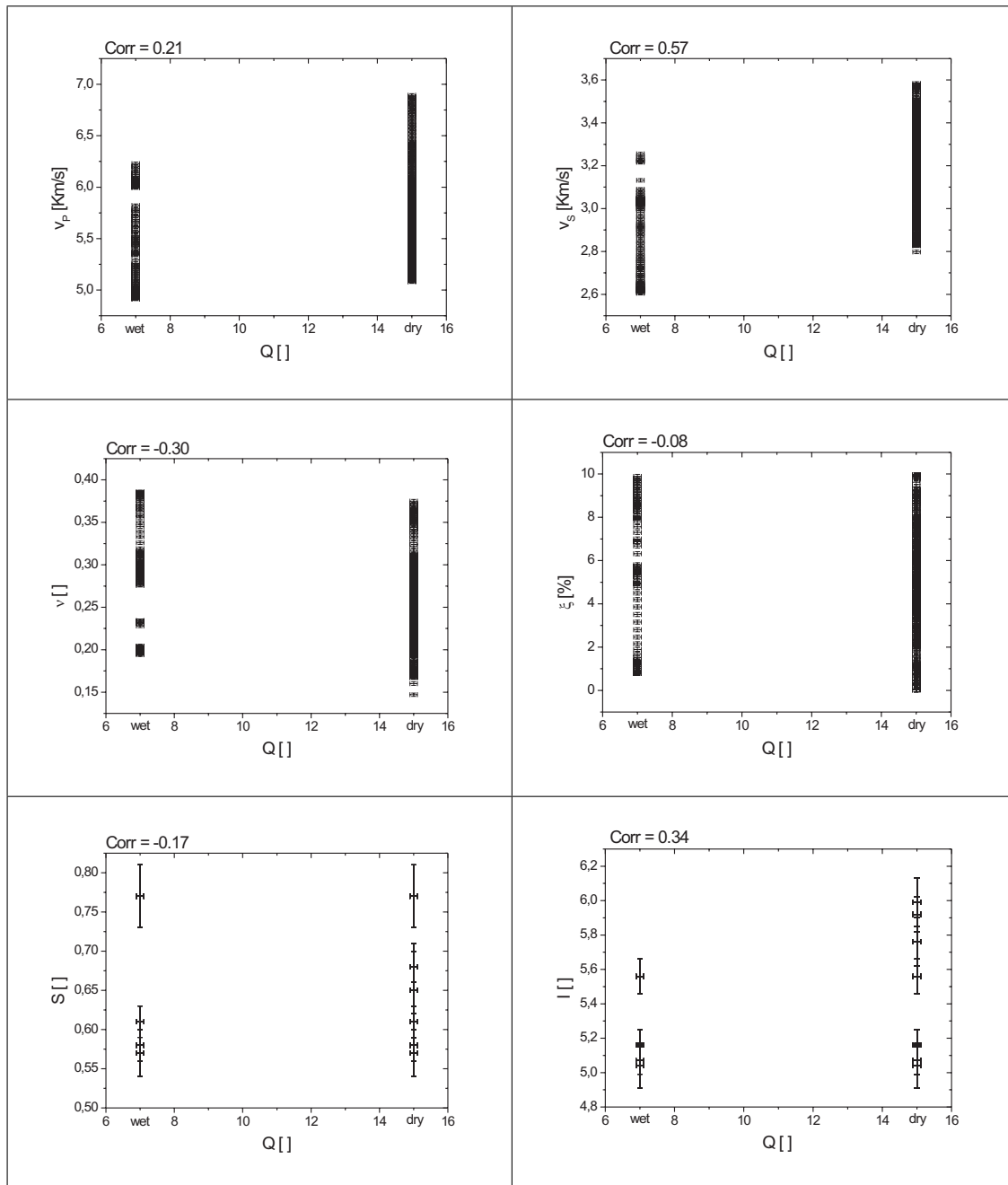


Figure 3.6: Cross plots and correlation coefficients $Corr$ of the seismic rock mass features v_p , v_s , ν , ξ , S and I vs. water inflow Q into the tunnel.

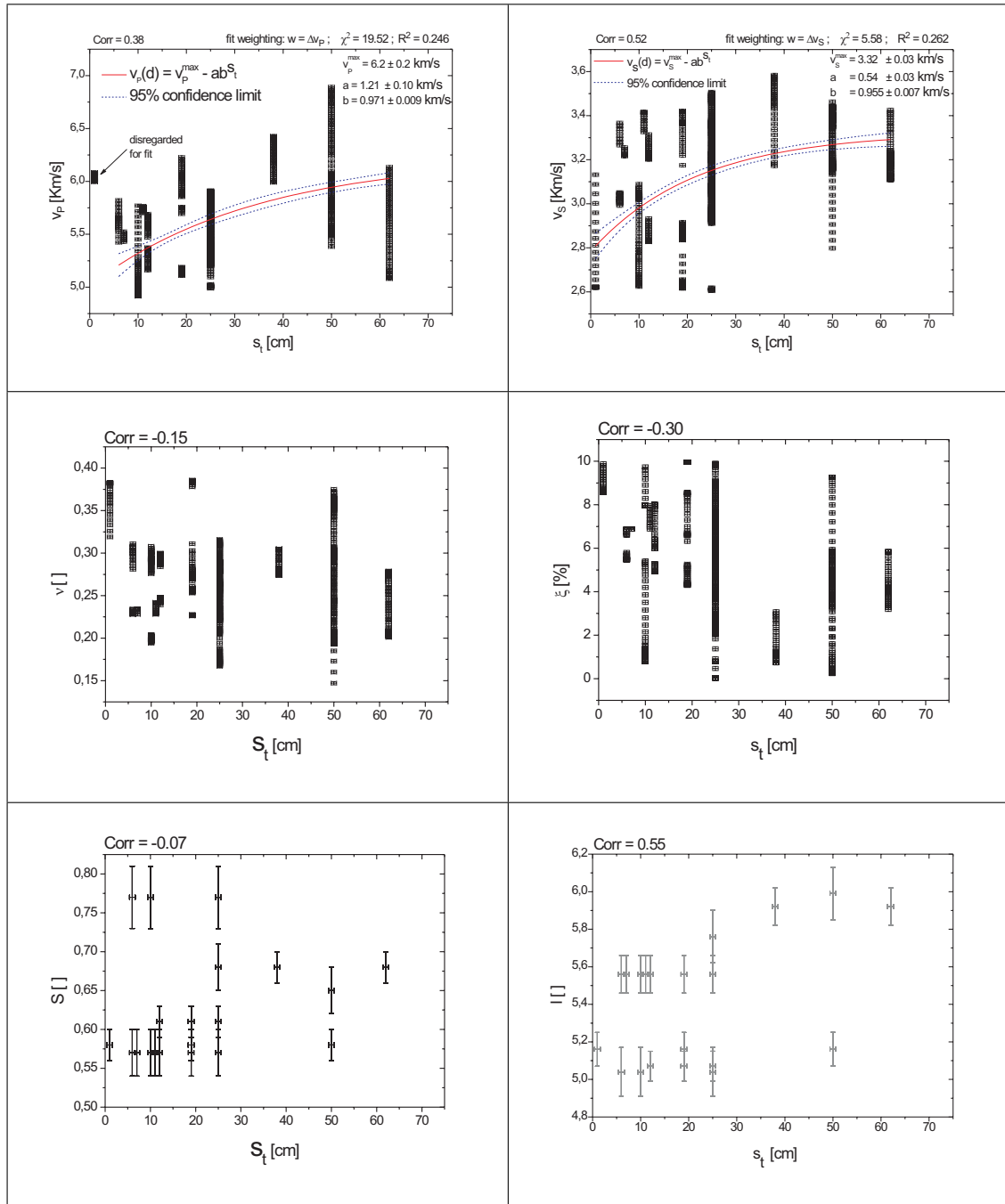


Figure 3.7: Cross plots and correlation coefficients $Corr$ of the seismic rock mass features v_p , v_s , ν , ξ , S and I vs. total fracture spacing s_t . The v_s - s_t -cross plot, v_p - s_t -cross plot, and I - s_t -cross plot show the best correlations. The related exponential fit functions with the 95%-confidence limit can be seen as well. Additional fit parameters are the weighting parameter w of each data point and the two quality parameter like the reduced χ^2 and R^2 .

3.4. Relationships between geological and seismic rock mass properties 71

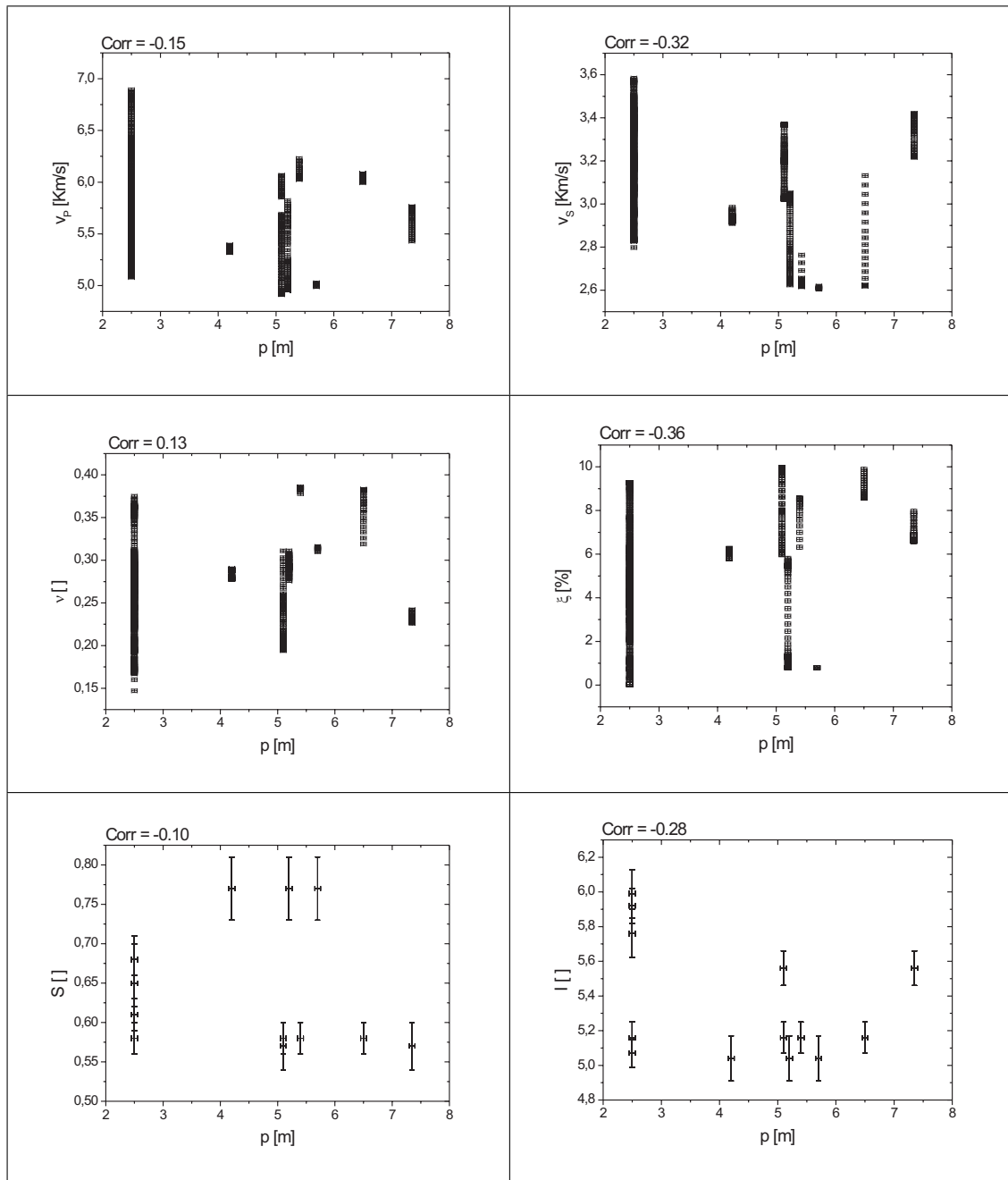


Figure 3.8: Cross plots and correlation coefficients $Corr$ of the seismic rock mass features v_p , v_s , ν , ξ , S and I vs. persistence of fractures p .

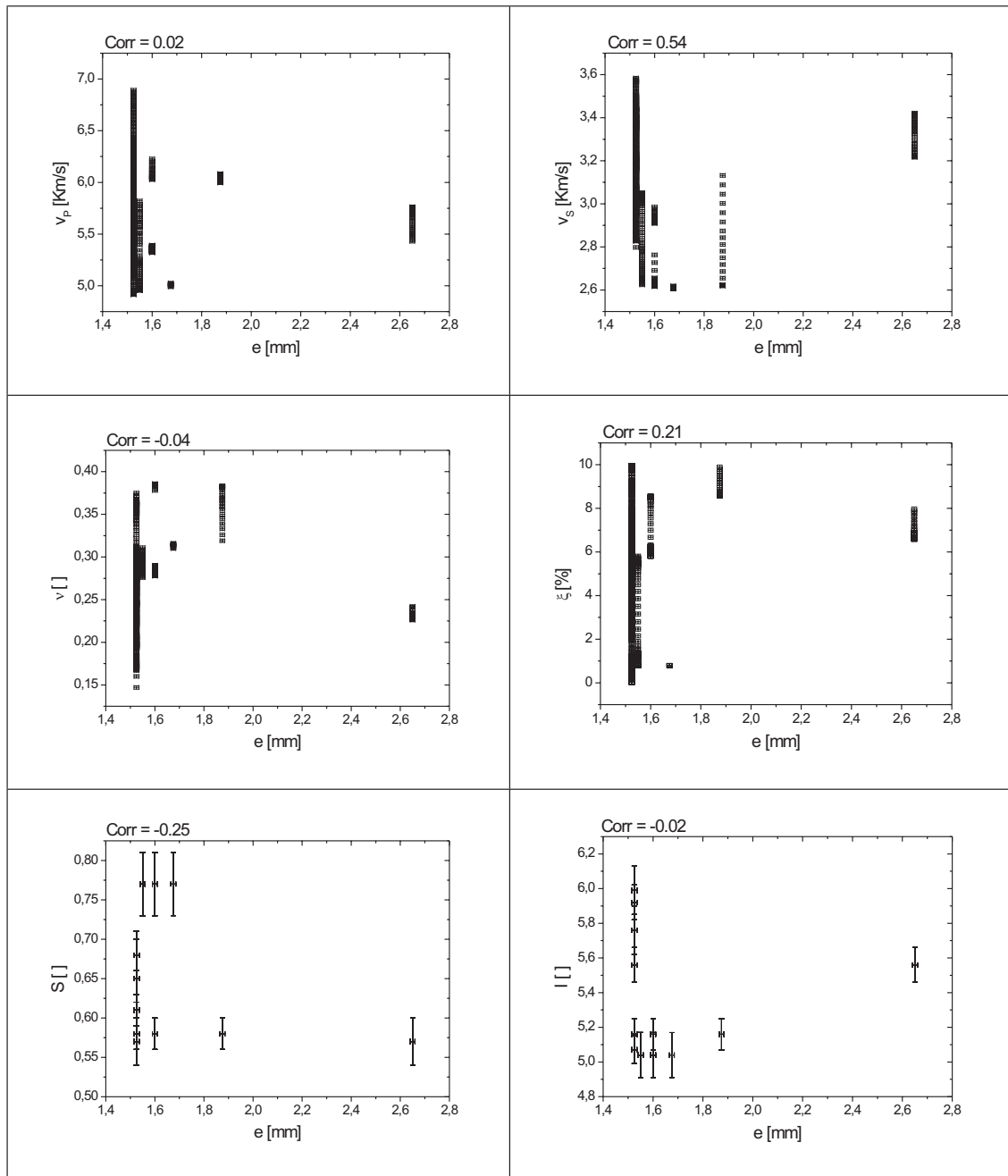


Figure 3.9: Cross plots and correlation coefficients $Corr$ of the seismic rock mass features v_P , v_S , ν , ξ , S and I vs. aperture of fractures e .

3.4. Relationships between geological and seismic rock mass properties 73

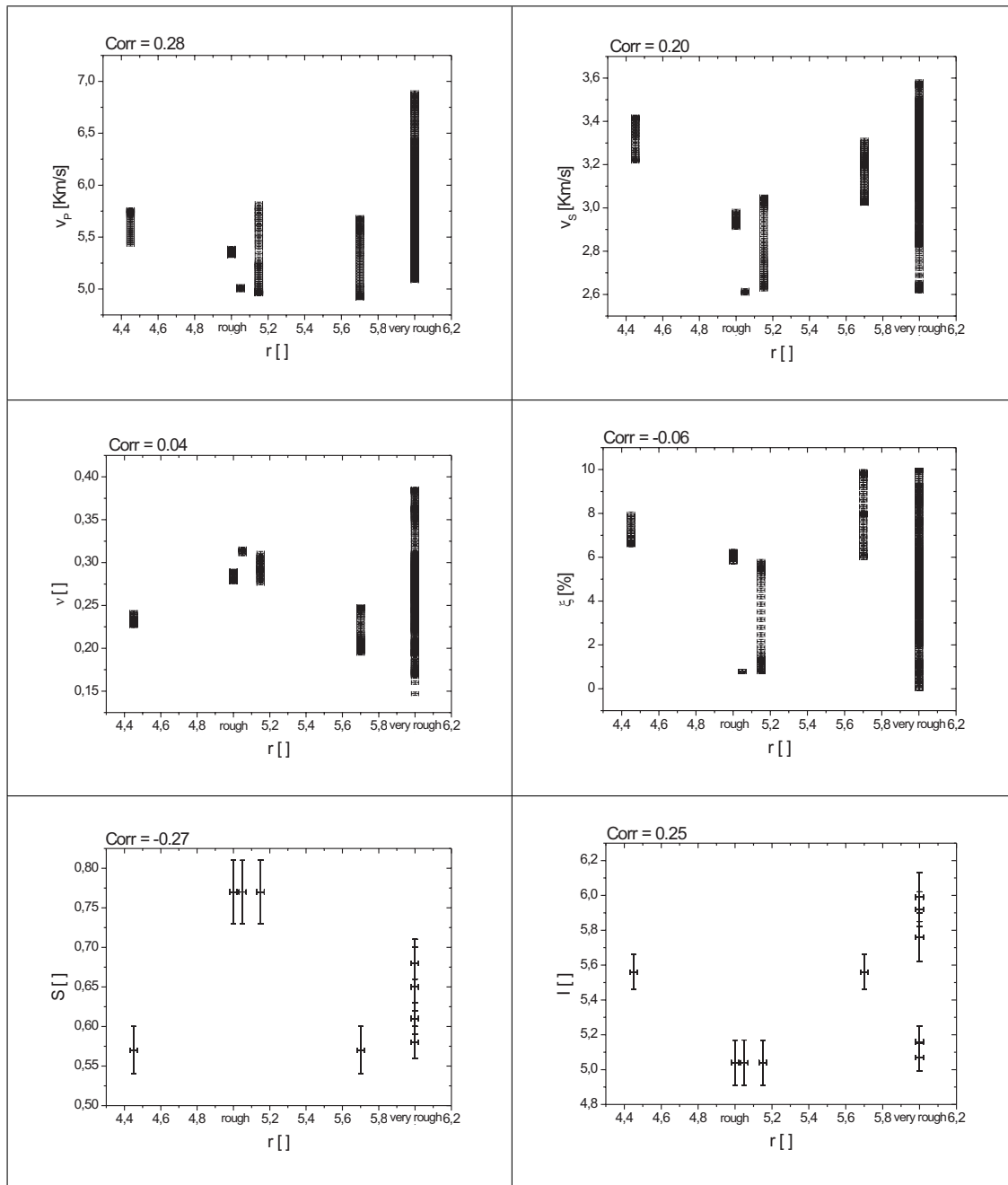


Figure 3.10: Cross plots and correlation coefficients $Corr$ of the seismic rock mass features v_P , v_S , ν , ξ , S and I vs. roughness of fractures r .

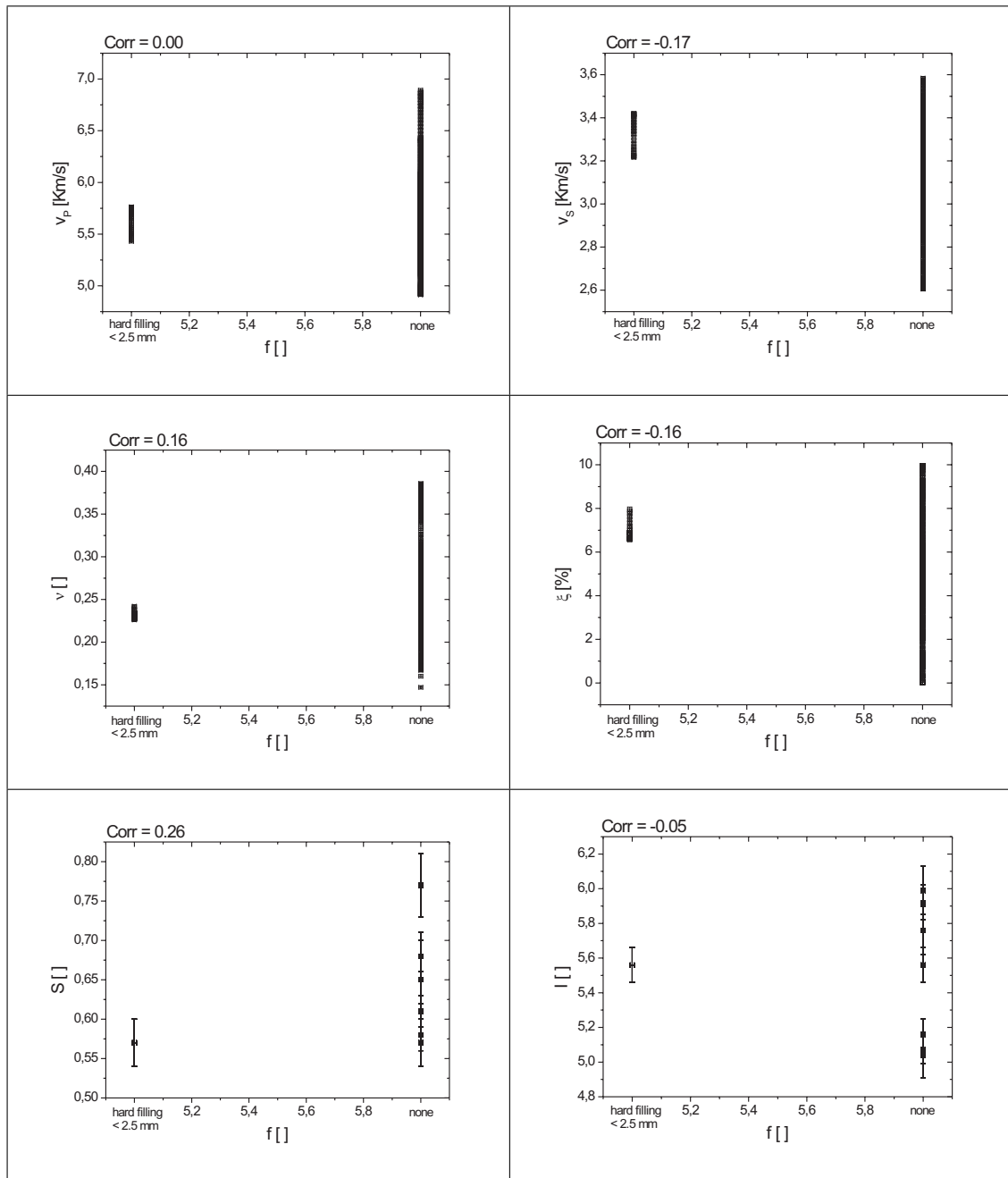


Figure 3.11: Cross plots and correlation coefficients $Corr$ of the seismic rock mass features v_p , v_s , ν , ξ , S and I vs. infilling of fractures f .

3.4. Relationships between geological and seismic rock mass properties 75

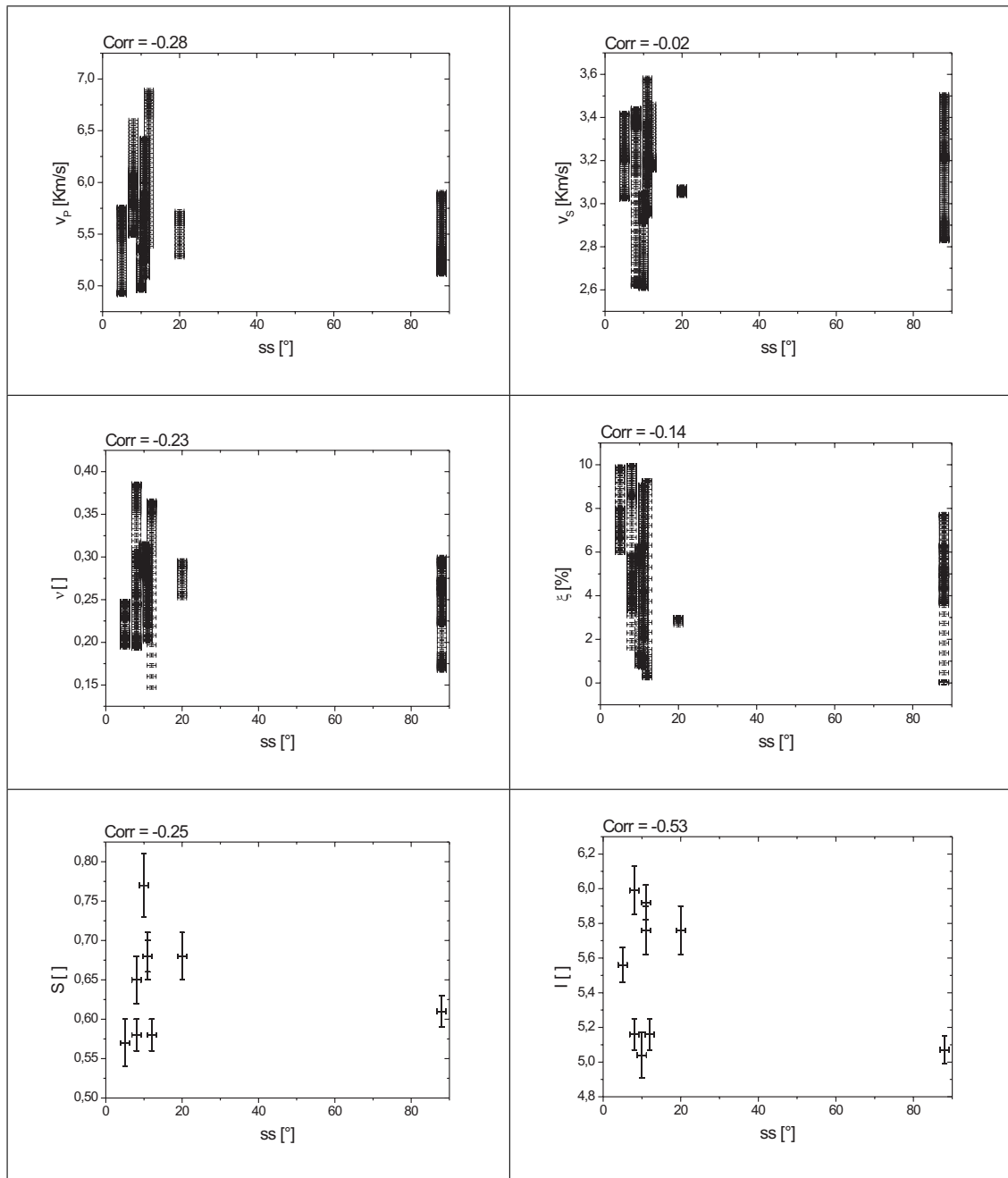


Figure 3.12: Cross plots and correlation coefficients $Corr$ of the seismic rock mass features v_P , v_S , μ , ξ , S and I vs. dipping of the schistosity ss .

3.4.5 Seismic velocities v_P and v_S

For a saturated rock, v_S and v_P decrease uniformly, whereas v_S initially decreases with increasing fracturing much faster than v_P . This can be qualitatively seen between 920 - 955 m in figure 3.13 and between 2395 - 2410 m in figure 3.14 in direction to the fault cores. v_P slightly decreases within the right disturbed zone (≥ 2410 m) of the cataclasite whereas v_P decreases rapidly within the left zone (≤ 2410 m), probably due to numerical reasons, because the P-wave length is too large to display the small low velocity zone within a high velocity medium of protolith. Thus, v_P -values near 7 km/s are too high.

Around brittle faults between 930 - 960 m, 1120 - 1200 m, and around 2410 m (see figure 3.4, 3.13, and 3.14), large or small disturbed zones can be displayed by seismic profiling along the tunnel wall. Thus, it could be possible to estimate the existence and the location of a fault core in front of a disturbed zone, if the seismic profile is sufficiently long and if the minimum velocity values within fault cores are known.

3.4.6 Poisson's ratio ν

The ratio between v_P and v_S expressed in the dynamic Poisson's ratio ν can be used to verify that the fractures related the cataclasite are fluid filled. It could be observed, that the small ≈ 30 cm thick cataclasite is "wet" on the left tunnel wall at 2410 m. It strikes in W-E direction (nearly perpendicular to the tunnel). Indeed, water filled fractures can be assumed in the left part within 5 m depth, because ν -values around 0.38 indicate fluid filled fractures. In saturated fractured rock v_S decreases with increasing fracturing, because $v_S = 0$ km/s in water. In contrast, v_P is constant or increases slightly with increasing fracturing, because $v_P^{water} > v_P^{air}$. Hence, ν increases in saturated rock when the fracture spacing decreases and vice versa (e.g. O'Connell and Budiansky, 1974; Henyey and Pomphrey, 1982), because $\nu \propto \frac{1}{v_S}$, $\nu \propto v_P$, and with decreasing s_t more water fills the fractured rock mass, whereby v_S is being reduced. This argument can be confirmed at ≈ 2430 m in figure 3.4, whereas the cross plot of s_t - ν in figure 3.7 shows a very low correlation, as well as to all mapped geological parameters. It can be assumed that the low ν -values around 0.2 at tunnel location 2375 m represent a higher fractured rock mass than is was mapped, because the anisotropy ξ is very high with 10 % and the velocities are low. Side effects of the tomographic inversion techniques may amplify this effect.

3.4.7 Shear-wave anisotropy ξ

The shear-wave velocity anisotropy ξ , an additional seismic parameter besides v_P , v_S and ν , can be used to characterise the rock mass fracturing. Low ξ -values are not necessarily indicative of high s_t , whereas high ξ -values are diagnostic of low s_t , as mentioned by Ji and Salisbury (1993). ξ -values are low even if the rock mass is unfractured or if the rock mass is fractured by non-fluid filled fractures. Zappone et al. (1996) outlined an anisotropy of the Leventina gneiss between 4.5% and 6.5%

3.4. Relationships between geological and seismic rock mass properties 77

measured by laboratory experiments. The cross plots of ξ show very weak correlations to all geological properties (see figure 3.7 to figure 3.12). It can be seen in figure 3.4, figure 3.13, and figure 3.14 that the in-situ measurements show high anisotropy values with $\xi \geq 6\%$ within fault disturbed or damaged zones distant to the fault and fissured zones (e.g. at 900 m, 1150 m, 1890, 2380 m and 2425 m). Low ξ -values with $\xi \leq 2\%$ could be observed in disturbed zones close to the fault zones (between 930 - 964 m and 2405 - 2420 m), where more water ("wet") occurs at the tunnel wall. It can be confirmed, that the water within open cracks and fractures influence the shear-wave anisotropy as for example mentioned in Crampin (1985).

Further, in figure 3.1 s_t increases within the rock mass at 1600 m, whereby ξ increases together with a dramatic decrease of v_P , a slight decrease of v_S , and a strong decrease of ν . Thus, all seismic parameters show a feature pattern that indicates a decrease of s_t . If the fractured zone at 1690 m is responsible for this seismic feature pattern, only microscopic cracks can cause such significant changes of the seismic parameters. Observations of microcracks were neglected during this in-situ study. Boadu (1997) outlined that shorter fractures will tend to be relatively more sensitive to the variations in the seismic attributes than longer fractures as already mentioned in Barton and Zoback (1992) and Kuwahara et al. (1995).

3.4.8 Shape measure S and shape intensity I of the S_1 -wave polarisation ellipsoids

The mean values of the shape intensity I and the shape measure S of the S_1 -waves polarisation ellipsoids, which are averaged over all ellipsoids along the seismic profiles, contain additional information to characterise the rock mass. I is influenced by the fracture spacing s_t , which can be assumed from in the cross plot of figure 3.7. I contains information about the real amplitudes of the S_1 -waves. σ_c , Q , r , f and ss show low correlation coefficients to I . S describes the shape of the ellipsoids and shows at tunnel location 900 m in figure 3.4 very flattened ellipsoids ($S = 0.79$), which is an indicator of an highly fractured rock mass along the total seismic profile (see chapter 2).

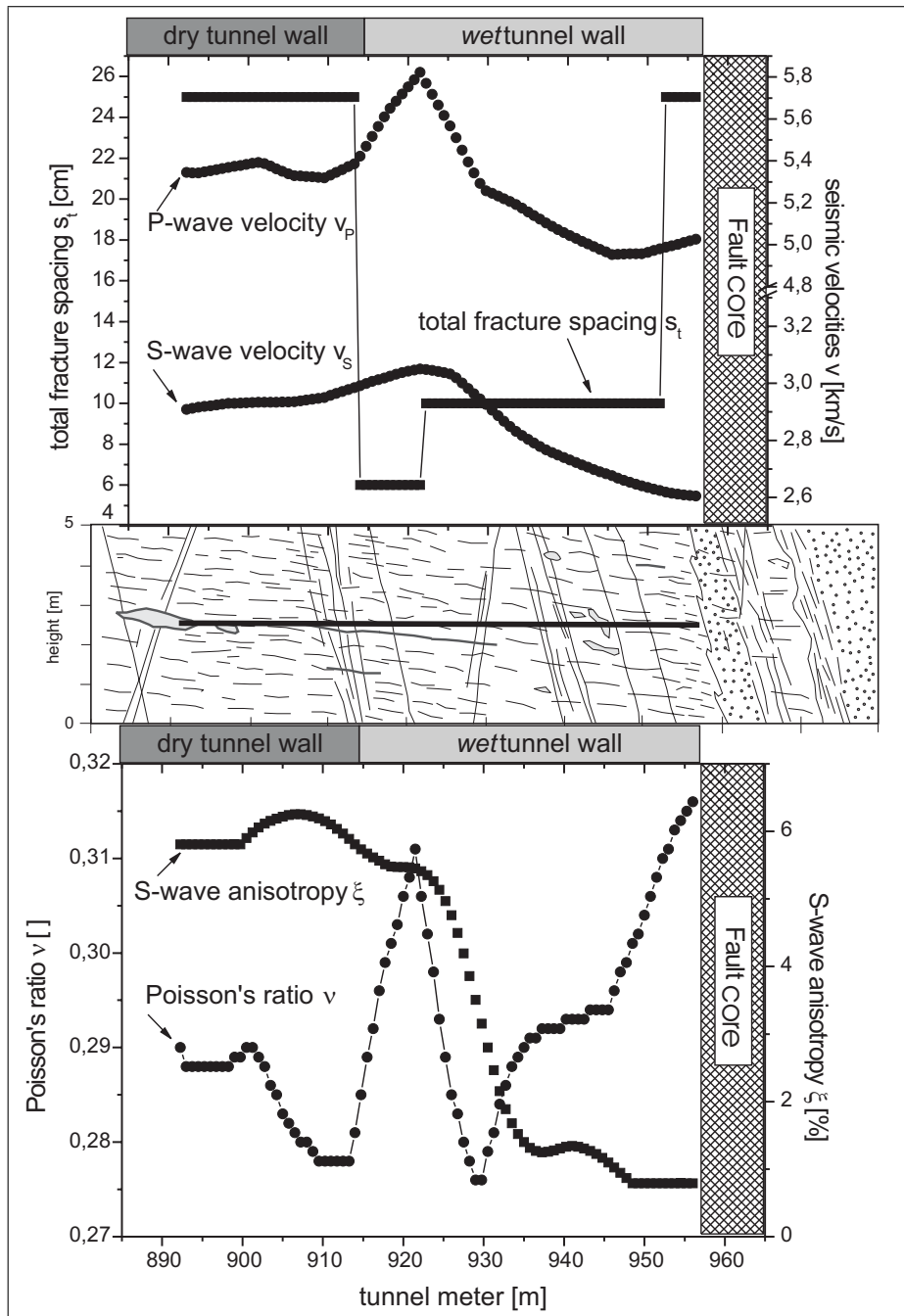


Figure 3.13: Schematic sketch of the geological situation, as shown in figure 2.8, together with the seismic rock mass properties v_P , v_S , ν and ξ and the geological properties s_t and Q along the tunnel profile between 881 - 963 m. The geological profile is vertically 5 times exaggerated.

3.4. Relationships between geological and seismic rock mass properties 79

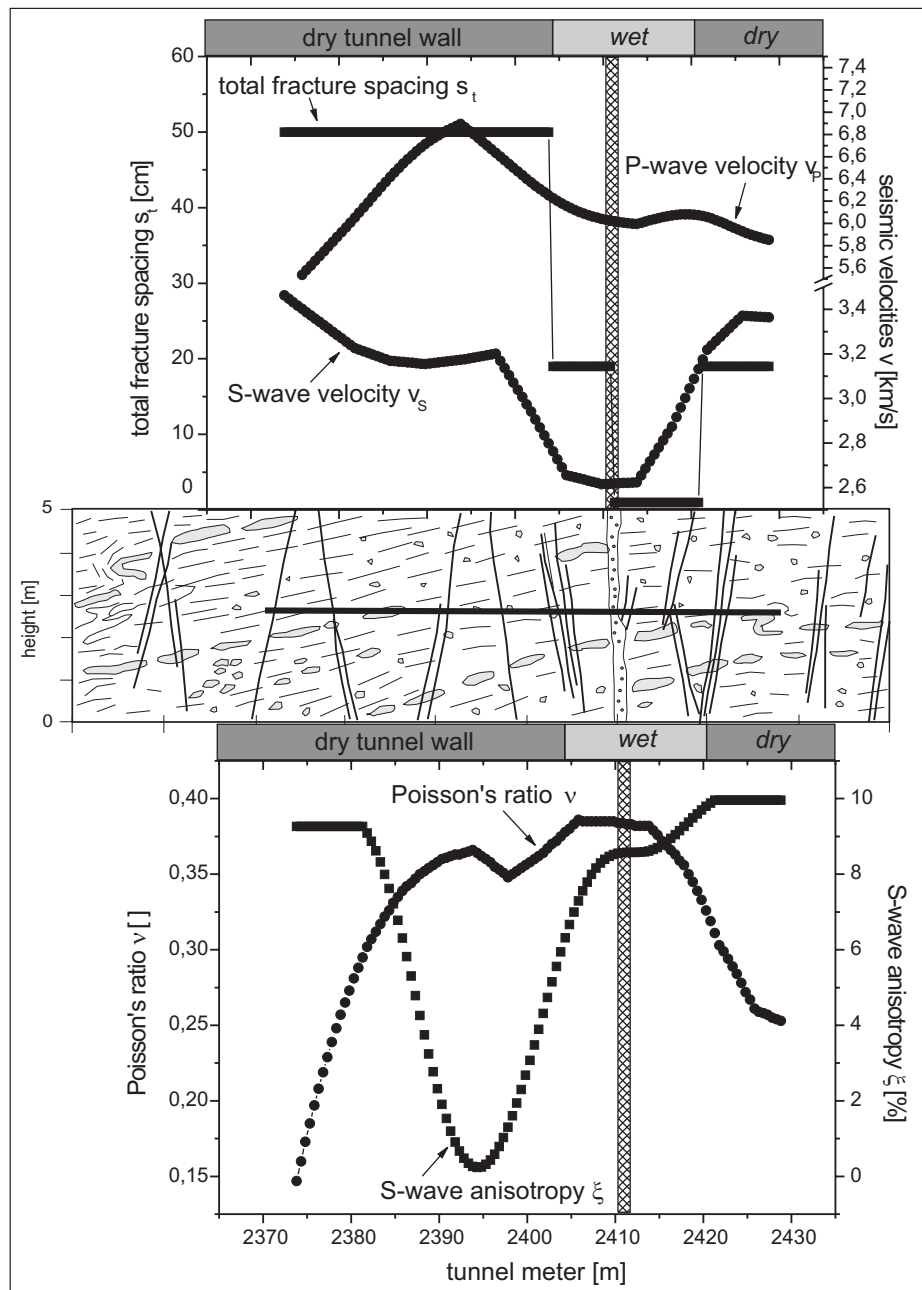


Figure 3.14: Schematic sketch of the geological situation, as shown in figure 2.14, together with the seismic rock mass properties v_p , v_s , ν and ξ and the geological properties s_t and Q along the tunnel profile between 2360 - 2433 m. The geological profile is vertically 5 times exaggerated.

3.5 Conclusion

The seismic investigations within the Faïdo adit show that it is difficult to characterise the geotechnical rock mass behavior of the granitic gneisses with a few and high-noised seismic rock mass properties by conventional methods like pairwise feature comparison. The fracture spacing of the rock mass is one the most significant engineering geological parameters. In this study, rock mass fracturing can only be qualitatively characterised as "low", "medium", and "dense" fracturing, based on shear-wave and compression-wave velocity. All other seismic parameters, i.e. dynamic Poisson's ratio, shear-wave velocity anisotropy and the shape measure S and shape intensity I of the S_1 -waves polarisation ellipsoids, show very low correlations with s_t . One reason can be seen in the ambiguity to interpret e.g. ν or ξ . For example, low ξ -values are not necessarily indicative of high s_t , whereas high ξ -values are diagnostic of low s_t . In addition it has been noticed, that most geological rock mass properties are only semi-quantitatively measured and subjectively approximatively acquired, like p , e , r , and f . For these reasons correlations to the seismic parameters are very weak. This means that it is insufficient to compare the geological and seismic properties pairwise in cross-plot diagrams and partially in spatial diagrams along scanlines.

Further, the seismic data interpretations have drawbacks due to:

- the artificially disturbed geological conditions around the tunnel after the excavation process, that are imaged by the tomograms, and
- by the logical reasoning, that the seismic properties are dependent variables. They depend on the geology. But, during a classification the independent geological properties are determined from the dependent seismic properties. This can lead to ambiguous interpretation results.

The quality of the seismic data which are measured in the Faïdo tunnel is very high, because they are acquired under excellent measurement conditions (3-component geophones with very high impedance matching, coherent and constant source signals, refraction seismic tomograms based on first arrivals of P- and $S_{1,2}$ -waves). The influence of the excavation disturbed zone is reduced by using reliable seismic data along scanline within the tomographic images, which are located 5 m (one tunnel radius) from the tunnel wall. Although the first and second limitation were reduced as good as possible, the seismic data are nevertheless noised.

Anyhow, around brittle faults, small or large disturbed zones can be recognised on the seismic profiles. Thus, it could be possible to estimate the existence and the location of the fault core in front of a disturbed zone, if the seismic profile is sufficiently long and if the minimum velocity values within fault cores are known.

The additional used parameters in this study, the shape measure S and shape intensity I of the S_1 -polarisations ellipsoids show that I decreases the more the rock mass is fractured, because the polarisation is disturbed by the fractures. S describes whether the geology along a seismic profile is dominantly fractured or foliated rock with aligned minerals. S can be an additional seismic parameter for the interpretation but the used

mean values do not show the full information. S should be better used to determine along the seismic profiles orientations of different anisotropies (crack/fracture or fabric induced) within a Mixture of Anisotropies (MA) that exist simultaneously in the rock mass.

Although the seismic measurements were carried out under best conditions, it remained very difficult to characterise the complex geology by interpreting noised seismic data based on the conventional methods, like correlations. Under in-situ conditions, the influences of the geological properties s_t , p , e , σ_c , Q , ss , r , f interfere and cause fuzzy distributions of the seismic data. Thus, the influences can not be easily determined by pairwise feature comparisons in cross plots and along tunnel profiles. The results of rock mass characterisations are of lower quality, especially at locations where s_t remains unchanged or only slightly. Thus, more powerful statistical methods have to be used for the given interpretation task. Statistical approaches based on neural information processing could find more structures behind the 6-dimensional seismic data, because the procedures take into account all seismic properties in combination to classify the geological rock mass properties. One approach, called Self-Organizing Maps SOM, is used to analyse the seismic and geological rock mass properties as outlined in chapter 4.

4 Classification by Self-Organising Maps SOM

Wissen allein ist nicht Zweck
des Menschen auf Erden; das
Wissen muss sich im Leben
auch betätigen.

(Hermann von Helmholtz)

Klose, C.^(1,2), Giese, R.⁽¹⁾, Loew, S.⁽²⁾, Borm, G.⁽¹⁾

⁽¹⁾ GFZ Potsdam, Geoengineering, Telegrafenberg, 14473 Potsdam, Germany

⁽²⁾ ETH Zürich, Chair of Engineering Geology, Hönggerberg, 8093 Zürich, Switzerland

Article in preparation for submission to
International Journal of Rock Mechanics and Mining Sciences

4.1 Introduction and objectives

It is known from laboratory experiments, in-situ measurements, and theoretical modelling studies, that rock fracturing strongly influences seismic velocities and the shear-wave polarisation, besides other rock parameters, like rock strength or water content, as described in chapter 2 of this thesis.

During numerical modelling or laboratory experiments, seismic parameters can be analysed under defined geological conditions, which lead to low-noised seismic data (i.e. O’Connel and Budiansky 1974 and Crampin 1985). Under in-situ conditions, the geological rock mass parameters vary in poorly defined ways and often lead to ambiguous seismic interpretations. For example, Moos and Zoback (1983) conclude: "it is not possible to simply relate fracture density to v_P ". Mooney and Ginzburg (1986) could not demonstrate a significant reduction of velocities in saturated microcracked and medium fractured rocks. Moos and Zoback (1983) and Stierman (1984) outline that other rock parameters besides macroscopic fracturing in saturated or unsaturated rock masses influence the mechanical properties of the rock mass and hence the seismic velocities. A systematic reason for ambiguous seismic interpretations, especially under in-situ conditions, is that analyses between geological and seismic properties are mostly based on pairwise comparisons, which do not show all the information of the high-dimensional geological and seismic feature space. Hence, with focus to understand the geological-seismic relationships under in-situ conditions, the geological rock mass properties should be classified with all seismic features in combination. The high noise of seismic data is considered simultaneously. The noise results from limitations of the seismic measurements and from the spatial variations of the geological rock mass conditions.

The second part of an extensive study within the Faido tunnel, an adit to the Gotthard Base Tunnel of the Swiss AlpTransit project, tries to characterise engineering geological rock mass properties from a large number of combined seismic properties. The considered geological properties are uniaxial compressive rock strength σ_c , water inflow Q , total fracture spacing s_t , persistence p , aperture e , infilling f , roughness r , and schistosity dipping ss . The seismic properties are P- and S-wave velocity v_P and v_S , Poisson’s ratio ν , shear-wave velocity anisotropy ξ , shape measure S and shape intensity I (see chapter 2) of the displacement ellipsoids of the leading shear-waves. The seismic data result from seven 3-component seismograms and 2-dimensional tomographic images ($\approx 70 \text{ m} \times 12 \text{ m}$), generated along the Faido tunnel wall. Detailed information on the seismic data acquisition is outlined in section 4.2 of this chapter, in chapter 3, and in chapter 2.

A new classification approach is used to characterise the geology from all joint seismic rock mass properties. The outlined pattern recognition approach of neural information processing is called Self-Organising Maps (SOM), and was introduced by Kohonen (2001). The classification approach is applied to pairwise (semi-quantitative) respectively non-pairwise comparisons between the 8 geological and the 6 seismic features of homogeneous units (clusters) within the 14-dimensional geological-seismic feature space. All classifications are based on the 6 combined seismic features. Conventional methods, like correlation analyses and feature comparisons along the tunnel

profiles, are less powerful in classifying the geological features from high-noised seismic data, as outlined in chapter 3. The SOM algorithm, based on the *SNNS* software package of Zell et al. (1998), is implemented into an expert system that stores 6 measured seismic properties (seismic memory), and classifies single geological properties and the homogeneous seismic-geological rock mass units as precise as possible.

Section 4.3 introduces the theory of the Self-Organising Maps (SOM) and explains two ways of interpreting the SOM. Section 4.2 gives information on the data acquisition and the observations of measured geotechnical and seismic rock mass properties. Section 4.5 outlines the results of the SOM classification and discusses both ways of interpretation, the logical and the statistical way.

4.2 Data acquisition

GeoForschungsZentrum Potsdam developed an Integrated Seismic Imaging System (ISIS) (Borm et al. 2001), that aims at imaging small-scale hazardous geotechnical structures such as faults simultaneously during the excavation process in two different ways. It measures in front of the excavation face, using diffraction and reflection seismic data and along the tunnel walls, using refraction seismic data for tomographic inversion techniques. A series of seismic measurements were carried out in the tunnel walls during the excavation process in the Faido access tunnel, an adit to the Gotthard Base Tunnel in southern Switzerland. Detailed information on the geology, the location of the Faido tunnel, and the data acquisition are outlined section 3.2. Section 3.3 gives an overview about the ISIS system and the seismic data acquisition.

4.2.1 Acquisition of the seismic data

6-dimensional seismic feature vectors $\{v_P, v_S, \nu, \xi, S, I\}$ are the basis of the geotechnical classification task. The seismic data acquisition is outlined in chapter 3 and 2. Figure 3.4 shows the spatial distributions of the seismic data along the tunnel profiles. It is nearly impossible to visually describe and compare all 6 seismic parameters in detail from location to location. For that reason, Self-Organising Maps (SOM) are first used to characterise the seismic data, and, then, to classify the geological rock mass properties based on the seismic information stored in the SOM.

4.2.2 Acquisition of the geological data

At the same time, geological information are acquired during the tunnel excavation process, as described in chapter 3. Eight geological properties, that influence the seismic properties of the rock mass in different ways and can be used for rock mass classification (i.e Bieniawski 1989), are described and used for the classification task. The geological feature vectors $\{\sigma_c, Q, s_t, p, e, r, f, ss\}$ contain the following geological attributes: uniaxial compressive strength σ_c parallel to the schistosity, water inflow

into the tunnel Q , total fracture spacing s_t , fracture persistence p , fracture aperture e , fracture roughness r , fracture infilling f , and schistosity dip angle ss . Figure 3.1 shows the spatial distributions of the seismic data along the tunnel profiles.

4.3 Self-Organising maps

4.3.1 Theoretical background

Self-Organising Maps (SOM), introduced by Kohonen (e.g. Kohonen 2001), are simple analogues to the brains way to organise information in a logical manner. The main purpose of this information processing is the transformation of a feature vector of arbitrary dimension drawn from the given feature space into simplified, generally 2-dimensional, discrete maps or images. For the given task, the feature space is build up by 6 seismic features (properties). A SOM network performs the transformation adaptively in a topological ordered fashion. This type of neural network utilises an unsupervised learning method, known as competitive learning, and is useful for analysing data with unknown relationships. Figure 4.1 A) shows the structure of a SOM neural network, with two layers: an input layer and a Kohonen layer. The Kohonen layer represents a structure with a single 2-dimensional map consisting of neurons arranged in rows and columns. Each neuron of this discrete lattice is fixed and is fully connected with all source neurons in the input layer. If one neuron in the Kohonen layer is excited by some stimulus, neurons in the surrounding area are excited, too. That means for the given task, each seismic feature vector, which is presented to the 6 neurons of the input layer, typically causes a localised region of active neurons against the quiet background in the Kohonen layer. The degree of lateral interaction between a stimulated neuron and neighbouring neurons is usually described by a "Gaussian function"

$$h_{k,i(\vec{x})} = \exp\left(-\frac{d_{k,i(\vec{x})}^2}{2\sigma^2}\right), \quad (4.1)$$

which can be seen in figure 4.1 B). d is the lateral neuron distance in the Kohonen layer, σ is the "effective width" which changes during the learning process and h is the activity of the neighbouring neurons. Specifications of the feature vectors occur in the Kohonen layer in the same topological order as they are presented by the metric (similarity) relations in the original feature space, while performing a dimensionality reduction of the original feature space.

Before the self-organising procedure begins, the link values, called weights,

$$\vec{w}_k = \{w_{(k,v_P)}, w_{(k,v_S)}, w_{(k,\nu)}, w_{(k,\xi)}, w_{(k,S)}, w_{(k,I)}\}^T \mid k = 1, 2, \dots, m, \dots, l \quad (4.2)$$

are initialised as random values. \vec{w}_k connect the n input layer neurons to the l neurons in the Kohonen layer. n is the dimension of the input space (seismic feature space) and l is number of all Kohonen neurons. Learning occurs during the self-organising procedure as feature vectors

$$\vec{x} = \{v_P, v_S, \nu, \xi, S, I\}^T, \quad (4.3)$$

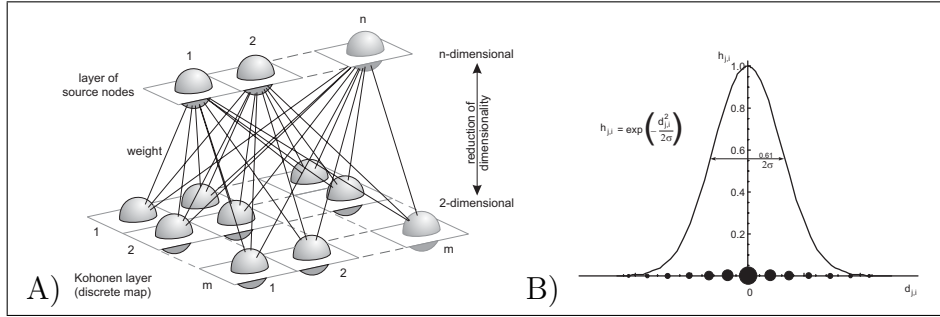


Figure 4.1: *Illustration of a SOM neural network A). The SOM projects the information of a n -dimensional feature space into a 2-dimensional lattice, whereby the dimensions are reduced. n (seismic) features of a feature vector, also called input vector, $\{v_P, v_S, \nu, \xi, S, I\}$ are represented to n source nodes. After training and classification the feature vectors can be seen as active neurons in the Kohonen lattice. The activity is a function of the feature vector and the weights that link the source layer with the Kohonen layer. The Kohonen layer typically consists of a localised region of active neurons against the quiet background, see picture B). The degree of lateral interaction between a stimulated neuron and neighboring neurons is usually described by the outlined "Gaussian function", where d is the neuron distance, σ is the "effective width" and h is the activity of the neighbouring neurons.*

also called input vectors, are presented to the input layer of the network. The neurons of the Kohonen layer compete to see which neuron will be stimulated by the feature vectors \vec{x} . The weights \vec{w}_k are used to determine only one stimulated neuron in the Kohonen layer after the 'winner takes all' principle. This principle can be summarised as follows: for each \vec{x} , the Kohonen neurons compute their respective values of a discriminant function (i.e. Euclidean distance $\|\vec{x}_i - \vec{w}_k\|$). These values are used to define the 'winner' neuron. That means, the network determines the index j of that neuron, whose weight \vec{w}_k is the closest to vector \vec{x}_i by

$$j(\vec{x}_i) = \arg \min_k \|\vec{x}_i - \vec{w}_k\| \quad | \quad k = 1, 2, \dots, m, \dots, l. \quad (4.4)$$

The particular neuron is declared winner of the competition. In other words, during the competition the weights \vec{w}_k change, whereas the neurons in the Kohonen lattice are always fixed and unchanged. Afterwards, the learning procedure modifies the weights w_j of the winner neuron and the winners neighbourhood during the calculation step t .

$$\vec{w}_k(t+1) = \vec{w}_k(t) + \eta(t) h_{k,i(\vec{x})}(t) (\vec{x}_i(t) - \vec{w}_k(t)), \quad (4.5)$$

where $\eta(t)$ is the learning-rate parameter, and $h_{k,i(\vec{x})}(t)$ is the neighbourhood function centered around the winning neuron $j(\vec{x}_i)$. The neighbourhood function or "Gaussian function" in eq. 4.1 determines how much the neighbouring neurons become modified. Only neurons within the winners neighbourhood get to participate in the learning process. During the self-organising process the neighbourhood size σ decreases until

its size is zero, and only the winning neuron is modified each time an input vector is presented to the network. The learning rate η (the amount each weight can be modified) decreases during the learning as well. Once the SOM algorithm has converged, the feature maps display the following important statistical characteristics of the represented feature space, also called input space:

Property 1 *Approximation:* *A feature map represented by a set of weights in the Kohonen layer, provides a good approximation to the input space.*

Property 2 *Topological ordering:* *The 2-dimensional feature map is topologically ordered in the sense that the spatial location of a Kohonen layer neuron corresponds to a particular feature of the higher dimensional input space.*

Property 3 *Density matching:* *The feature map reflects variations in the statistics of the distribution of the original feature space: regions in the input space from which sample vectors are drawn with a high probability of occurrence are mapped onto larger domains in the Kohonen layer, and therefore with better resolution than regions in the input space where sample vectors are drawn with a low probability of occurrence.*

Property 4 *Feature selection:* *The self-organising map is able to select the best feature for approximating the underlying nonlinear distribution of the input space.*

A SOM neural network is generated and trained for the classification. It has the following structure and properties:

represented feature space:	\mathbb{R}^6	$\{v_P, v_S, \nu, \xi, S, I\}^T$
number of feature/input vectors:	729	drawn from all seismic profiles
number of input neurons n :	6	
number of Kohonen neurons m :	100	(10 rows and 10 columns)
number of weights l :	600	
number of iterations t_F :	5000	
initial learning rate $\eta(t = 0)$:	0.5	
final learning rate $\eta(t_F)$:	0.01	
initial neighbourhood size $\sigma(t = 0)$:	5	
final neighbourhood size $\sigma(t_F)$:	1	decreasing every 1000 iterations

The Poisson's ratio ν is taken into account during the classification task, against a wide-spread argument in the geological and geophysical community, that ν or the v_P/v_S -ratio should not be used for seismic data interpretation when v_P and v_S are already available, because they are a function of v_P and v_S . The argument can not stand, due to the fact that the higher the dimensionality of the feature space is, the lower may be the rate of miss-classification. This is illustrated in a simple example in figure 4.2. Lets denote four data points $D = \{v_p, v_S\}$, whereas two data points are related to class \bullet and two data points are related to class \blacksquare as follows:

1. sphere: $D_{\bullet}^1 = \{5.0, 2.5\}$; $D_{\bullet}^2 = \{6.0, 3.0\}$

2. square: $D_{\blacksquare}^1 = \{5.0, 3.0\}$; $D_{\blacksquare}^2 = \{6.0, 2.5\}$

A neuron (within a neural network) tries to separate the data points of the two classes by a linear discriminant function within the $\{v_p, v_s\}$ -space. Figure 4.2 A) shows that it is impossible to separate these data points by a single linear function. Taking e.g. the v_p/v_s -ratio into account, the feature space is expanded by one dimension (see figure 4.2 B)) and the modified data points $D' = \{v_p, v_s, v_p/v_s\}$ can be described as follows:

1. sphere: $D_{\bullet}^{\prime 1} = \{5.0, 2.5, 2.0\}$; $D_{\bullet}^{\prime 2} = \{6.0, 3.0, 2.0\}$
 2. square: $D_{\blacksquare}^{\prime 1} = \{5.0, 3.0, 1.7\}$; $D_{\blacksquare}^{\prime 2} = \{6.0, 2.5, 2.4\}$

It can be seen in figure 4.2 C) that the data points D' can now be separated by a linear hyper-plane within the 3-dimensional feature space. It is illustrated by the gap between the imagined connection lines of the data points of the same class.

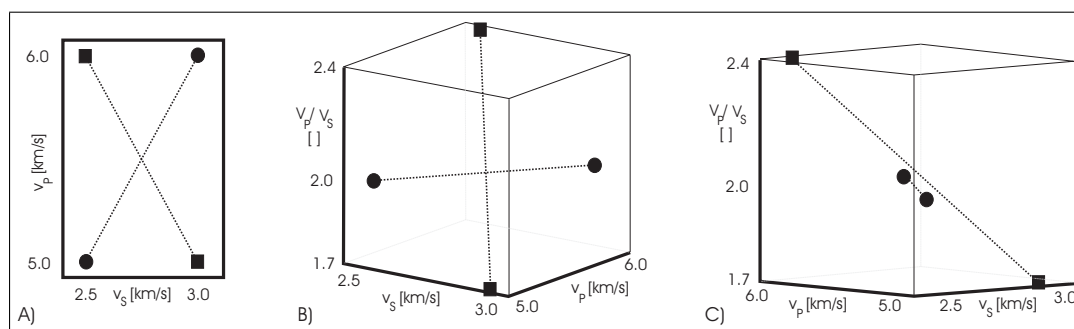


Figure 4.2: *Illustration to show the evidence why the v_p/v_s -ratio or the Poisson's ratio ν are important for classifications, even if v_p and v_s are already used. It can be seen that the data points of the two different classes (\bullet , \blacksquare) can only be separated by a linear hyper-plane within the 3-dimensional feature space $\{v_p, v_s, v_p/v_s\}$, see picture C). It is illustrated by the gap between the imagined connection lines of the data points of the same class. It is impossible to separate the data points by a single linear function in the $\{v_p, v_s\}$ -space, see picture A).*

4.3.2 SOM interpretation

The memory of the trained neural network is based on all 729 6-dimensional seismic feature vectors, that are drawn from all 7 seismic profiles (see figure 3.4). The experiences about all combined seismic features that are stored in the network can be visualised in 'feature maps' in the 2-dimensional Kohonen layer. The feature maps contain statistical information (Property 1 and 4), interdependencies (Property 2 and 4), and probabilities of occurrence (Property 3 and 4) of the seismic feature states.

On each location i along a seismic profile, a feature vector $\vec{x}_i = \{v_p, v_s, \nu, \xi, S, I\}$ is drawn and is presented to the SOM network. Each \vec{x}_i stimulates a specific neuron in

the Kohonen layer. Again, the network determines the index j of that neuron, whose weight \vec{w}_k is closest to vector \vec{x}_i by

$$j(\vec{x}_i) = \arg \min_k \|\vec{x}_i - \vec{w}_k\| \quad | \quad k = 1, 2, \dots, 100. \quad (4.6)$$

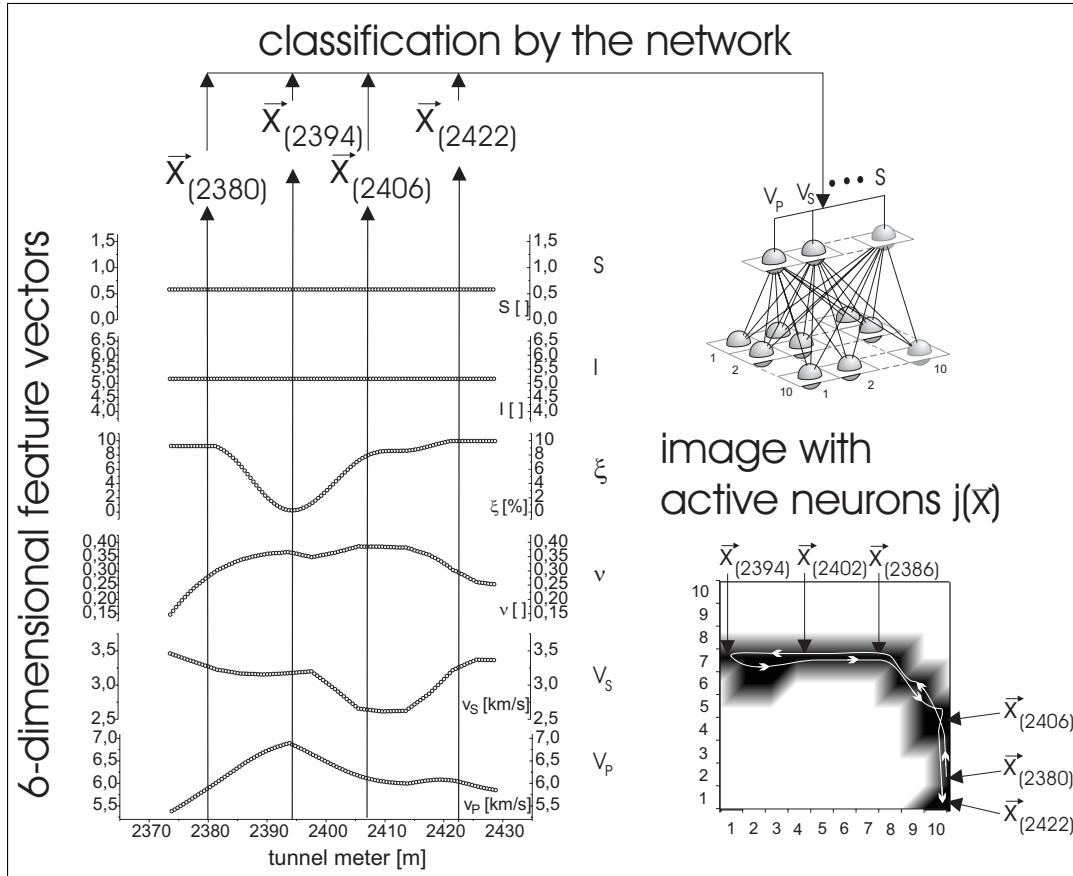


Figure 4.3: Classification scheme of a SOM neural network. 6-dimensional seismic feature vectors \vec{x} were drawn along a seismic profile (here: profile 2360 - 2433 m). Several tunnel locations can be seen: 2380 m, (2386 m), 2394 m, (2402 m), 2406 m and 2422 m. Each \vec{x} is presented to the network. The classification is done, when a neuron in the Kohonen lattice is stimulated. This neuron is active (black) and can be imaged in the lattice. All active neurons can be seen that are related to each \vec{x} . The white trace in the black region shows schematically, which neurons get active when the profile is being crossed.

The neuron j represents \vec{x} as best as possible and becomes active. Figure 4.3 illustrates the classification scheme of the SOM network. The classification is exemplified by sample feature vectors drawn from the seismic profile 2360 - 2433 m. Figure 4.4 shows all active neurons (black) that represent all combined feature vectors of the 7 seismic profiles. It can be seen that the stimulated areas in the SOM occur as separated polymorph regions from seismic profile to seismic profile. The active SOM area of the seismic profile at tunnel meter 881-963 m is close to that of the seismic profile

at 2132-2205 m. It differs from the seismic profiles at tunnel meter 1130-1215 m, 1314-1379 m, 1582-1663 m, and 1858-1929 m, and differs partially from seismic profile at tunnel meter 2360-2433 m. Differences in these areas result from dissimilarities in the seismic data manifold (Property 2 and 4 in section 4.3.1). A manifold is a topological space which is locally Euclidean (i.e., around every point, there is a neighbourhood which is topologically the same as the unit sphere in \mathbb{R}^n). The heterogeneous geological conditions at the measured locations might be responsible for the seismic feature states. The seismic-geological relationships are analysed in section 4.4. Section 4.4.1 shows how geological rock mass properties can be related to seismic data and shows, which geological reasons cause the seismic feature states.

4.4 Observations

4.4.1 Characterisation of rock mass properties

The results of the self-organising process can be visualised as an image in the Kohonen layer of the SOM. One way, which is used to interpret the SOM, is a semi-quantitative approach. The geological and seismic properties, also called features, are divided each into four classes or logical sets: "very low" (v.l.), "low" (l.), "high" (h.), and "very high" (v.h.).

The definition of the classes is based on the probability density distribution, called density kernels, of each parameter. Figure 4.5 and 4.6 show the density kernels of the seismic and geological parameters. The kernel densities are determined by a non-parametric technique of probability density estimation (Silverman 1986). The class boundaries for each seismic and geological feature, which characterise classes with equidistant intervals, result from the following descriptive kernel parameters: minimum (Min), first quartile ($P_{25\%}$), second quartile ($P_{50\%}$), third quartile ($P_{75\%}$), and maximum (Max). These five parameters are outlined in each plot of the kernel densities. Data points lower than $P_{50\%}$ are "low" and lower than $P_{25\%}$ are "very low", whereas data points higher than $P_{50\%}$ are "high" and higher than $P_{75\%}$ are "very high". This type of class definition is subjective but simple and necessary, because no prior knowledge is available about the relationships between the rock mass properties.

Seismic feature maps

Each seismic feature of a feature vector $\{v_P, v_S, \nu, \xi, S, I\}$, that stimulates a neuron in the Kohonen layer, can be visualised by its true or semi-quantitative class value. Figure 4.7 shows the 6 seismic feature maps imaged by their feature classes "very low" (v.l.), "low" (l.), "high" (h.), and "very high" (v.h.) as stated above. Areas within the maps are labeled like vp_2^l consisting of the name of the variable vp , the superscript with name of the class l ., and the subscript with the number of this area 2. The seismic feature maps have the following characteristics:

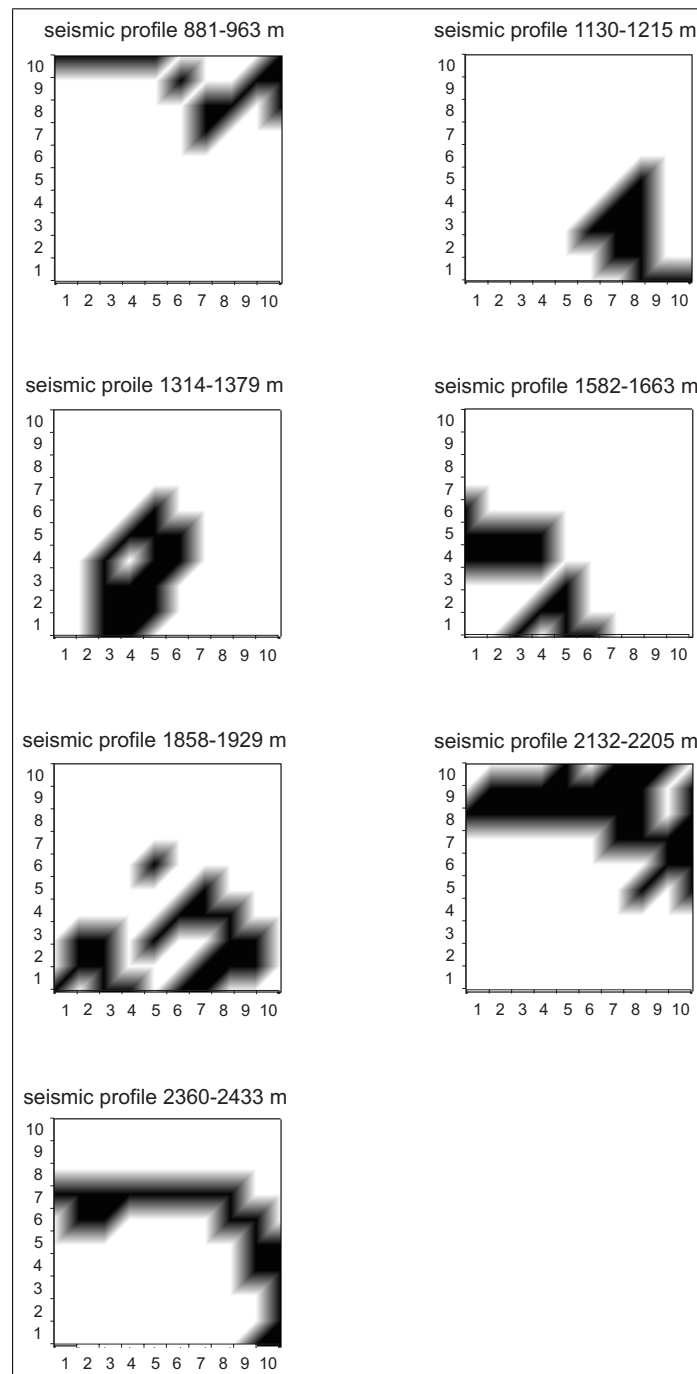


Figure 4.4: *SOM-classification results in the Kohonen lattice based on the profile locations along the Faido tunnel. Neurons become active (black) within the feature map when seismic feature vectors simulate the Kohonen neurons. The white areas exemplify inactive regions and the gray boundaries result from imaging process.*

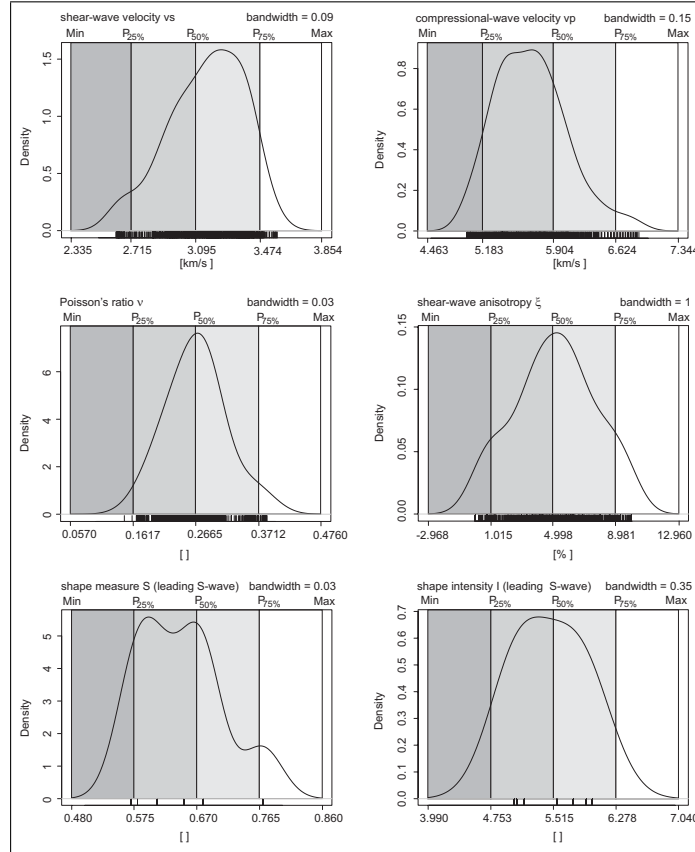


Figure 4.5: *Distribution of the probability densities (kernels) of the 6 seismic parameters. The linguistic classes "very low" (dark gray), "low" (gray), "high" (light gray) and "very high" (white).*

Compression-wave velocities v_P : The feature map of the v_P shows a non-linear and partially arc shaped structure of the class distribution.

Shear-wave velocities v_S : The feature map of v_S is more dispersed than the map of v_P .

Poisson's ratio ν : The feature map of ν shows a similar arc shaped structure of the class distribution like the velocities (ν is a function of v_P and v_S).

Shear-wave velocity anisotropy ξ : The feature map of ξ shows continuously ordered areas $\xi^{v.l.}$, ξ^l , ξ^h , and $\xi^{v.h.}$ and a regular linear distribution of the class boundaries, which are totally different from all other seismic properties, especially to the v_P , v_S , and ν . Thus, ξ is independent from v_P , v_S , and ν .

Shear-wave shape measure S : The feature map of the S -values shows an arc shaped structure with a dispersed class distribution similar to the velocities.

Shear-wave shape intensity I : The feature map of the I -values shows only two classes with an arc shaped structure of the class boundary similar to the v_P .

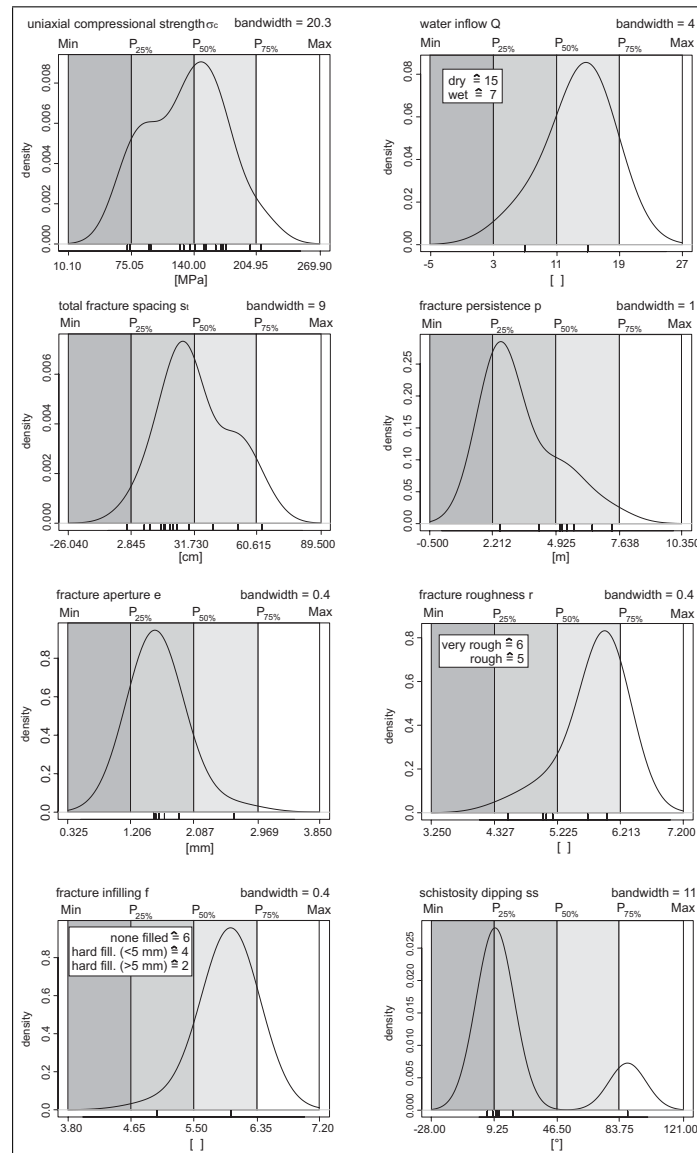


Figure 4.6: *Distribution of the probability densities (kernels) of the 8 geological parameters. The linguistic classes "very low" (dark gray), "low" (gray), "high" (light gray) and "very high" (white). w , r , and f can only be subjectively measured and are determined after the classification scheme of Bieniawski (1989).*

Geological feature maps

Each geological rock mass property can be visualised as a function of all seismic rock mass properties within the 2-dimensional SOM lattice. SOM is a function approximator that transforms the 6-dimensional seismic feature space into a 2-dimensional space where active neurons can be plotted. An active neuron is stimulated by a seismic

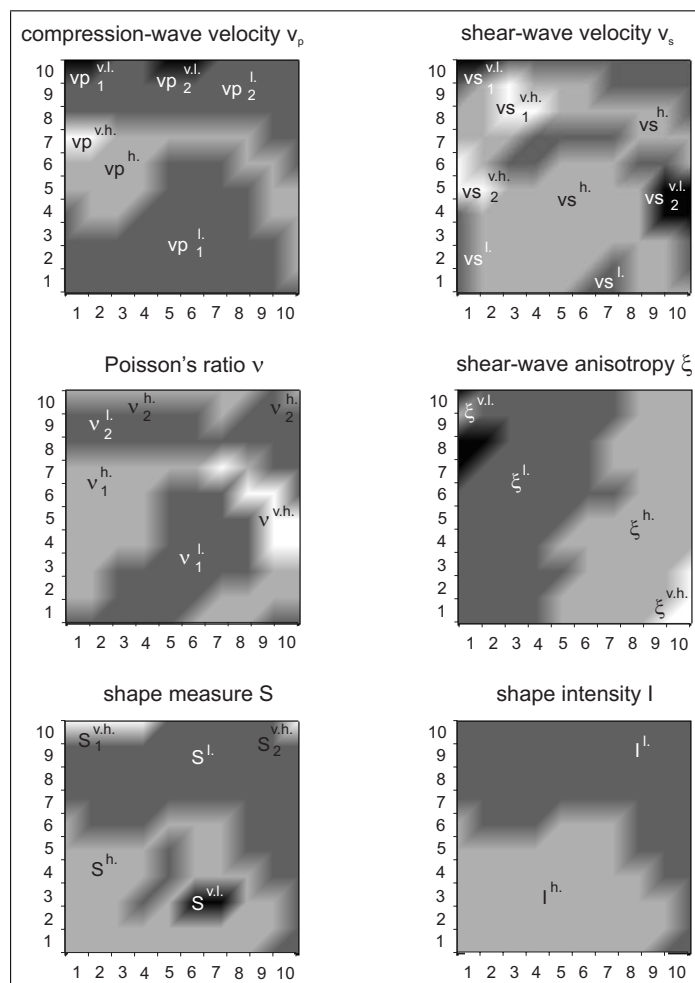


Figure 4.7: *SOM-classification results in the Kohonen lattice based on the 6 seismic feature classes. The classes are derived from quantiles of the probability density distributions in figure 4.5: "very low - v.l." (dark gray), "low - l." (gray), "high - h." (light gray) and "very high - v.h." (white).*

feature vector drawn from a seismic profile on a specific location. At this location geological feature vectors exist as well. Hence, instead of an active neuron (black, see figure 4.4) the geological rock mass properties can be plotted with their true or semi-quantitative class values (i.e. gray scale).

Figure 4.8 shows the feature maps of the geological rock mass properties: uniaxial compressive strength of the rock σ_c , water flow Q into the tunnel, total fracture spacing s_t , fracture persistence p , fracture aperture e , fracture roughness r , fracture infilling f , and schistosity dipping ss . The classes of the geological parameters are derived as aforementioned.

The comparison of the class distributions of the geological features with those of

the seismic features can lead to characterisations of low quality, because the class boundaries are subjectively derived. The SOM in figure 4.8 should be read only in the context, that all geological rock mass properties are either qualitatively and quantitatively indefinite. They influence the seismic features which are also partially indefinite. Thus, all observations are only approximations with many uncertainties of the true, but unknown, rock mass. The following summary describes the SOM classification results of the 8 geological features. Single characteristics and remarkable areas of the SOM are discussed. Classification rules can be created with respect to the physical reliability and the distribution within the SOM.

Uniaxial compressive strength σ_c : The feature map of the σ_c -values shows a very undulating irregular shape.

Water inflow Q : The feature map of the Q -values shows an even shape distribution with several clustered areas.

Total fracture spacing s_t : The feature map of the s_t -values shows a very regular shape distribution compared to those of the other parameters. The s_t -values decrease from area $s^{v.h.}$ irregularly to all sides of the lattice.

Fracture persistence p : The feature map of the p -values shows an even shaped distribution with several clustered areas comparable to that of the Q -values.

Fracture aperture e : The feature map of the fracture apertures shows mostly low e -values e^l . Very high and very low e -values do not occur.

Fracture infilling f : The feature map of the fracture infilling shows the same pattern like that of the fracture aperture with mostly "high" f -values f^h (none filling).

Fracture roughness r : The feature map of the fracture roughness consists of a single large closed area r^h ("very rough") and of three small and dispersed areas $r_{1,2,3}^l$ ("rough").

Schistosity dipping ss : Three major areas with some small heterogeneities (outliers) occur in the feature map of the schistosity dipping ss : ss^l , $ss^{v.h.}$, and $ss^{v.l.}$. The three areas show arc shaped geometries and have similarities to the structure in the v_P -feature map.

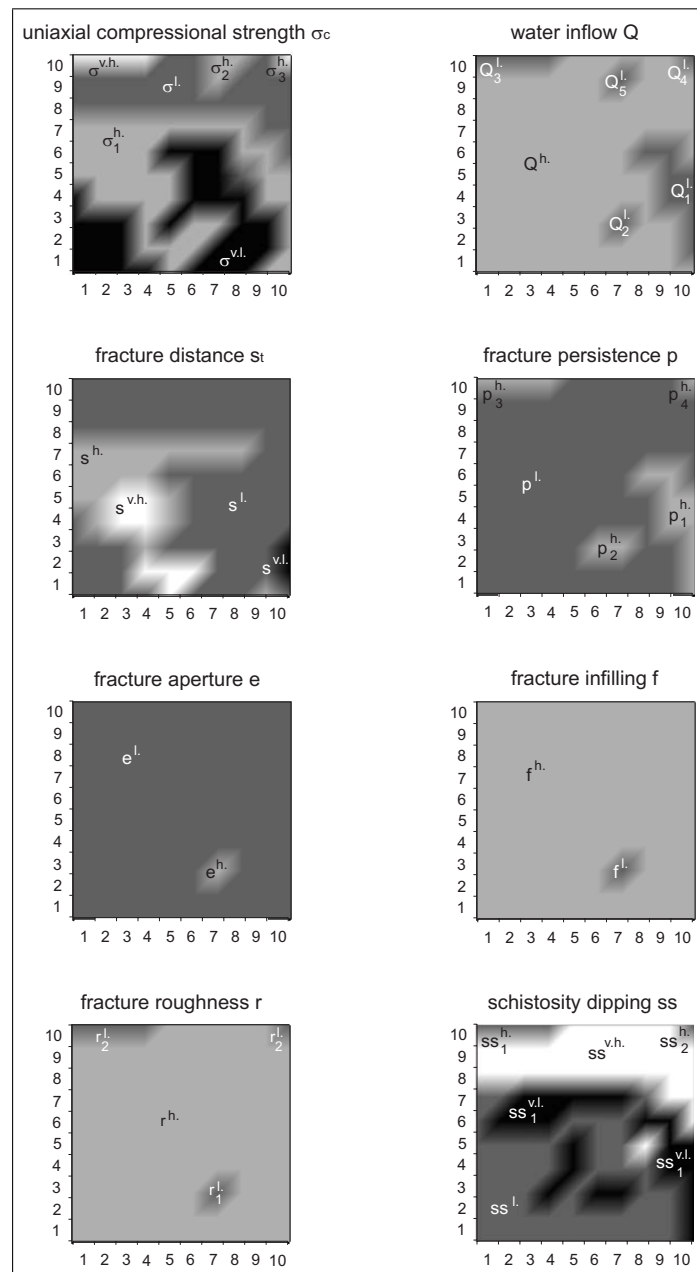


Figure 4.8: *SOM-classification results in the Kohonen lattice based on the 8 geological feature classes. The classes are derived from figure 4.6: "very low - v.l." (dark gray), "low - l." (gray), "high - h." (light gray) and "very high - v.h." (white).*

4.4.2 Characterisation of homogeneous rock mass units

Determination of homogeneous rock mass units

The outlined approach in this section analyses the data manifold of all given properties or features in combination. Homogeneous rock mass units can be described by clusters (sub-sets) that result from an objective partitioning process called clustering. Data interpretations by these clusters differ from those by logical classes (see section 4.4.1) in the point that clusters describe phenomenological homogeneous units in the data manifold based on all combined features, whereas logical classes describes the data manifold based on single features independent from other features. Classes result from subjective and logic descriptions, whereas the clusters result from objective partitioning methods.

Rock mass can be described by the combined seismic and geological features that built up vectors $\vec{\mathbf{R}} = \{v_S, v_P, \nu, \xi, S, I, \sigma_c, Q, s_t, p, e, r, f, ss\}$ in a 14-dimensional feature space. It can be assumed that all features are equally important for rock mass characterisation. Hence, each feature has to be preprocessed, e.g. normalised, so that its mean value, averaged over the entire feature vectors $\vec{\mathbf{R}}_i, i = 1, \dots, 729$, is close to zero, or else it is small compared to its standard deviation (LeCun, 1993). Once all $\vec{\mathbf{R}}$ are normalised, they can be partitioned into a preferred number of clusters. Two constrains can be formulated to find a representative number of clusters:

- high average quality of separation of all clusters
- high quality of separation of each single cluster

The partitioning method used to separate k homogeneous sub-groups of the entire 14-dimensional feature space is called "pam" (Rousseeuw 1987 and Kaufman and Rousseeuw 1990). The pam-algorithm searches for k representative clusters among the feature vectors $\vec{\mathbf{R}}(i), i = 1, \dots, 729$. After defining a set of k clusters, the clusters are constructed by assigning each feature vector to the nearest cluster. The goal is to find k representative cluster mean values or representants that minimise the sum of dissimilarities of the vectors to their closest representant. For each vector $\vec{\mathbf{R}}(i)$, a silhouette width $s(i)$ is defined as follows:

- Calculate the average dissimilarity $a(i)$ between $\vec{\mathbf{R}}(i)$ and all other vectors of a cluster to which $\vec{\mathbf{R}}(i)$ belongs.
- Calculate for all other clusters C the average dissimilarity $d(i, C)$ of $\vec{\mathbf{R}}(i)$ with respect to all vectors of C .
- The smallest of these $d(i, C)$ is $b(i) = \min_C d(i, C)$, and can be seen as the dissimilarity between $\vec{\mathbf{R}}(i)$ and its "neighbour" cluster, i.e., the nearest cluster to which it does not belong.
- Finally, calculate the silhouette width $s(i) = \frac{b(i) - a(i)}{\max(a(i), b(i))}$, as an indicator for the separation quality of a $\vec{\mathbf{R}}(i)$.

Feature vectors with a large $s(i)$ (almost 1) are very well separated, a small $s(i)$ (around 0) means that the observation lies between two clusters, and observations with a negative $s(i)$ are probably placed in the wrong cluster.

Feature maps of homogeneous rock mass regions

The data manifolds can be analysed by describing homogeneous units (clusters) of the seismic-geological feature space. The number of clusters depends on the observers precision, the interpretation overview, and the separation quality of the clusters. With an increasing cluster number, the precision and separation quality increases, whereas the overview decreases.

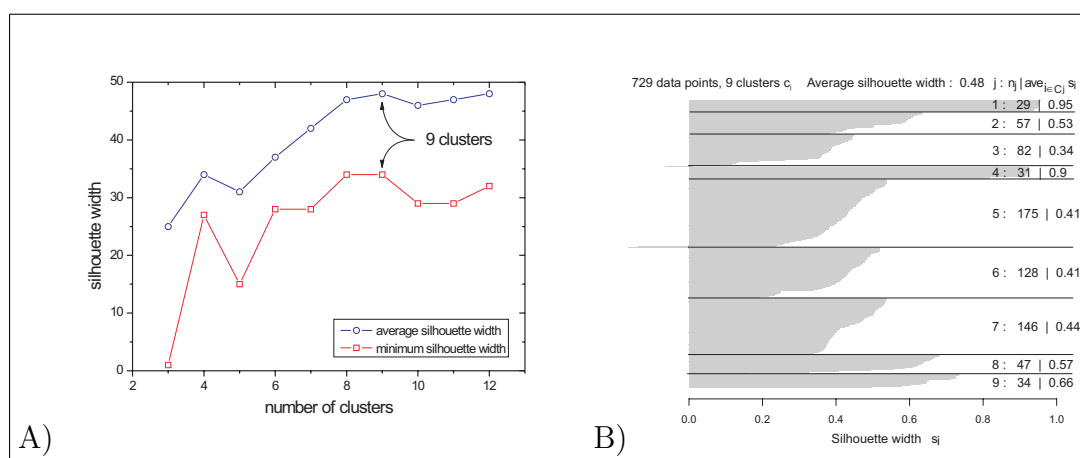


Figure 4.9: *Silhouette width s as a function of the cluster numbers j with $s \cdot 100\%$ is illustrated in picture A). The average silhouette width $ave_{C_j} s_i$ of all clusters, the minimum silhouette width $\min_{i \in C_j} s_i$ of a single cluster, and a representative number of clusters to diversify the seismic-geological feature space, are shown in picture A). 9 clusters (see table 4.1) represent the feature space well. Picture B) shows the clustering result: the average silhouette width $ave_{i \in C_j} s_i$ of the 9 clusters, the number and the plotted s_i of the cluster members, the number of the cluster members and the silhouette width s_i of each cluster.*

Figure 4.9 shows the cluster separation quality using the grouping method "pam" (Rousseeuw 1987 and Kaufman and Rousseeuw 1990) as described before. The average and the minimum cluster silhouette width increase strongly until the number of clusters is 9. The average silhouette width is nearly stable for more than 9 clusters, whereas the minimum silhouette width decreases slightly. The overview about the clusters is lost, when the number of clusters becomes too large. A cluster number of 9 is preferred, because of the aforementioned constraints. Table 4.1 outlines the cluster mean vectors, as representants. Each feature is equally important from the classification point of view, due the normalisation of the vectors. It can be seen in table 4.1 that some features of different clusters remain nearly unchanged. Hence, their influence to the separation is unimportant.

The cluster labels can be plotted along the tunnel profiles, which are shown in figure 4.10. It shows that the noise along the profile compared to single seismic or geological features is reduced tremendously. The clusters approximate the seismic-geological feature space and more general structures become apparent. Such approximations can be beneficial for practical use, when general statements about the rock mass are

Table 4.1: Homogeneous rock mass units, to describe the rock mass quantitatively by using all seismic and all geological features in combination. The 9 clusters are represented by the 14 mean values. Figure 4.5 and 4.6 show the semantic understanding of the parameters, especially for the ordinal variables w , r , and f .

	1	2	3	4	5	6	7	8	9
v_P [$\frac{km}{s}$]	5.36	5.19	5.37	5.65	5.81	5.60	5.32	6.65	6.03
v_S [$\frac{km}{s}$]	2.93	2.83	3.20	3.35	3.37	3.07	3.17	3.16	2.72
ν []	0.286	0.288	0.225	0.228	0.245	0.286	0.225	0.354	0.372
ξ [%]	6.2	1.7	8.0	6.6	3.7	3.0	4.9	3.2	8.8
S []	0.77	0.77	0.57	0.57	0.65	0.68	0.61	0.58	0.58
I []	5.04	5.04	5.56	5.56	5.99	5.76	5.07	5.16	5.16
σ_c [MPa]	209	209	170	173	162	71	93	168	162
Q []	dry	wet	dry	dry	dry	dry	dry	dry	wet
s_t [cm]	21.8	11.0	29.2	17.6	51.5	29.2	29.2	51.6	0.6
p [m]	4.2	5.2	5.1	7.4	2.5	2.5	2.5	2.5	6.5
e [mm]	1.60	1.55	1.53	2.65	1.53	1.53	1.53	1.53	1.88
r []	rough	rough	rough	rough	very r.	very r.	very r.	very r.	very r.
f []	no	no	no	hard	no	no	no	no	no
ss [°]	10	10	5	5	8	20	88	12	8

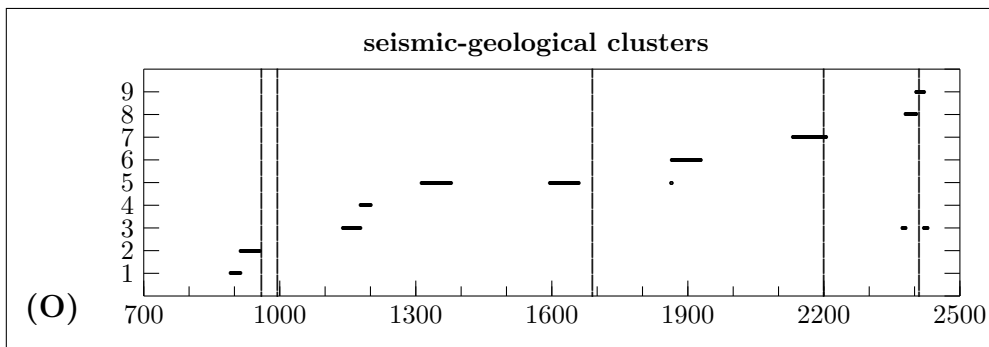


Figure 4.10: Spatial distribution of 9 clusters along in the Faido tunnel that represent phenomenological homogeneous rock mass units of the 6 seismic and the 8 geological features in combination. Table 4.1 outlines the 14 mean values of the 9 clusters. The vertical lines indicate fault zones between 960-995 m and at 2410 m and fractured zones at 1690 m and 2200 m.

required. On the other hand, this approach takes into account that all (measurable) rock mass properties describe the rock mass better than single properties, because they exist together and should be described together.

Figure 4.11 shows the active neurons for each cluster within the SOM. Feature vectors of similar clusters are related to active neurons in similar regions. Partially, they show the same arc shaped structures like the feature maps of the logical classes (figure 4.7 and 4.8). The similarities between the clusters are determined over all 14 features (see table 4.1) compared to the feature maps of the clusters in figure 4.11, which are based only on the 6 seismic features. Hence, the 14-dimensional feature space shows similar structures like the seismic feature space.

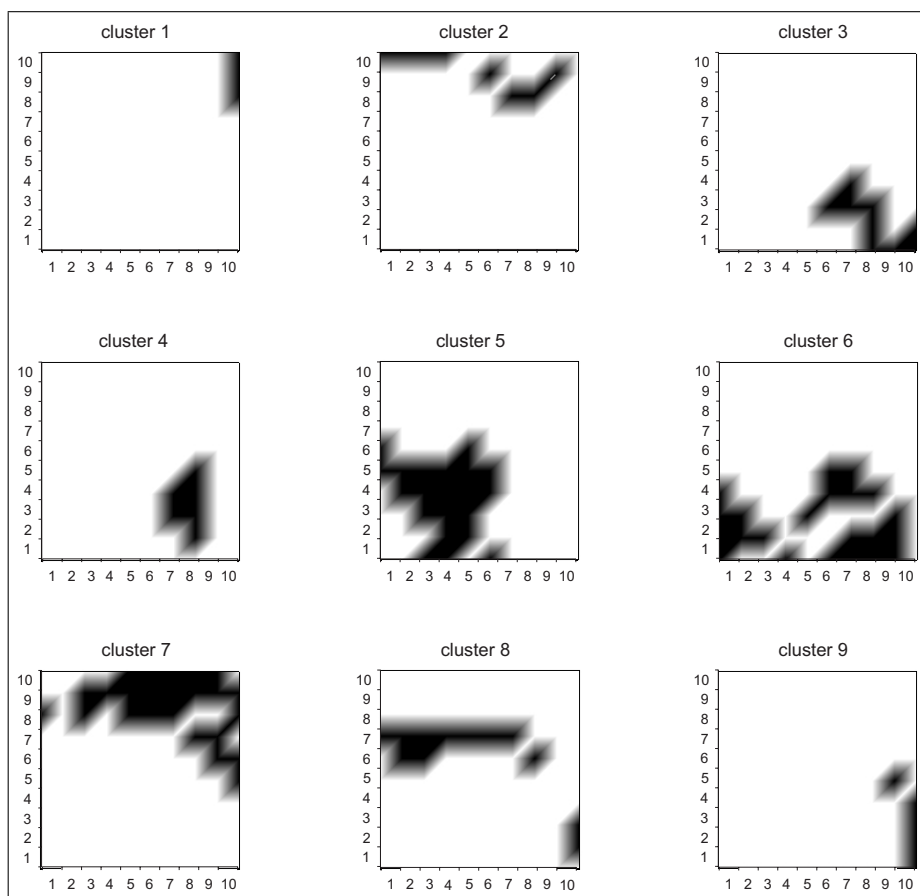


Figure 4.11: *SOM-classification results based on 9 homogeneous seismic-geological rock mass units (clusters). Neurons become active (black) within the SOM when the seismic feature vectors, that belong to one of the units, stimulate the Kohonen lattice. The white areas exemplify inactive regions and the gray boundaries result from imaging process. General characteristics of the homogeneous rock mass units of table 4.1 can be seen in the feature maps: distant black areas represent differences between the clusters.*

The active neuron areas of each cluster are polymorphic and have partially dispersed distributions with small overlaps. But they are still separated from the regions of the other clusters. The silhouette width of the clusters are lower than 1 and partially below 0 (figure 4.9 B). It indicates that vectors belong to two clusters or some vectors are probably placed within the "wrong" cluster. Further, it can be seen in figure 4.11, the feature maps of the clusters are similar to the feature maps of the seismic profiles in figure 4.4. SOM classification that is based on all seismic features makes it possible to characterise seismic-geological homogeneous rock mass regions.

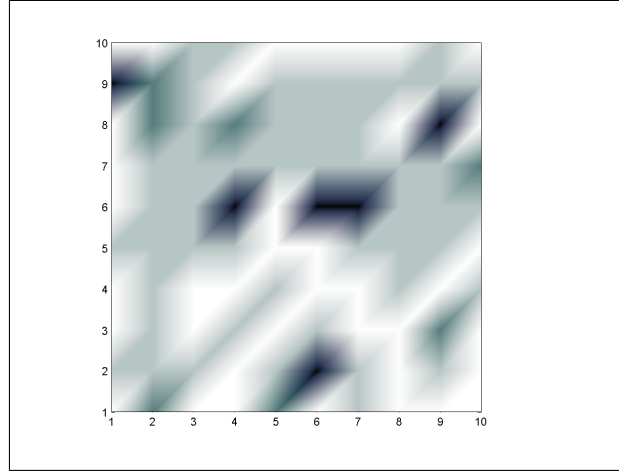


Figure 4.12: *The uncertainty map illustrates how certain the characterisation of the geology would be if a new classification of the trained SOM network is performed with a memory of 729 6-dimensional seismic feature vectors. The map can be read as follows: "very uncertain" (dark gray), "uncertain" (gray), "certain" (light gray) and "very certain" (white).*

An uncertainty value can also be assigned for a classification of a seismic feature vector. A classification of geological rock mass properties based on frequently or rarely measured seismic feature vectors is certain or uncertain. The uncertainty U can be derived from the probability of occurrence (property 3 and 4 in section 4.3.1)

$$p_i = P(\vec{x}_i) \quad | \quad i = 1, 2, \dots, 729, \quad (4.7)$$

whereas the occurrence describes the frequency of stimulated neurons during the training of the SOM network by the 729 given feature vectors. 'Uncertainty' is a synonym for 'information' or 'surprise'. In the 'information theory', U is defined as follows (Shannon, 1948 and Gray, 1990):

$$\begin{aligned} U_i(\vec{x}_i) &= \ln \left(\frac{1}{p_i} \right) \\ &= -\ln(p_i) \end{aligned} \quad (4.8)$$

A classification is certain if $U_i = 0$ and it decreases with increasing U_i . The SOM can be used to image U in a feature map. Figure 4.12 shows how certain the characterisation of the geology would be if a new classification of the trained SOM network is performed with a memory of 729 6-dimensional seismic feature vectors.

4.5 Discussion and conclusion

Several reasons exist why classification, especially conventional methods, are limited to characterise geological rock mass properties from seismic measurements under in-situ conditions:

- noise of the seismic data due to the varying geology,
- integral character of seismic waves to image the geology due to their wave length,
- numerical limitations of the tomographic imaging techniques,
- inaccuracies and subjective uncertainties of measured geological rock mass properties,
- the general fact that data in the high-dimensional seismic feature space are a function of the high-dimensional geological features space,
- complexity and nonlinearity between seismic and geological features and
- pairwise correlations show relationships between two features; they do not show the total amount of information in the observed feature spaces

The last point makes it necessary to use methods that show the total information. The application of the new statistical approach for the classification task, called self-Organising Maps (SOM), considers at each instance the interdependencies between all seismic features. The results of the SOM-classification are stored in a 2-dimensional lattice of neurons. SOM image the complexity and the inter-relations between single rock mass features. Seismic feature classes, geological feature classes, and seismic-geological clusters occur as polymorphic shaped and partially dispersed structures (areas of active neurons).

SOM classifications based on pairwise class comparisons uncover detailed relationships between the rock mass properties but they can lead to complicated classification schemes. For that reason, it is easier to describe and interpret specific areas of the SOM visually. The SOM has to be read with respect to the precision and confidence of measured properties. Many of the geological features like Q , r , and f are subjectively measured, whereas others like e and p are inaccurately acquired.

The feature maps of the seismic classes show remarkable characteristics. In figure 4.7 can be seen two areas $vp_{1,2}^l$. Both areas represent "low" v_P -values, but the feature vectors, they are related to, are different, because the neurons are distant. The area with $vp_1^{v.l.}$ and $vp^{v.h.}$ are, with respect to the topological order (Property 2 in section

4.3.1), more or less similar, although both classes are different. σ_c can be seen as a reason for the distribution of v_P . σ_c can be mostly described by the distribution of v_P and partially by ν . The area with the lattice coordinates (1,10) shows $vp_1^{v.l.}$ although σ_c is "v.h.". At these measurement locations s_t influences v_P more than σ_c .

The v_S -feature map shows two separated areas $vs_{1,2}^{v.h.}$ and two extremely distant areas $vs_{1,2}^{v.l.}$. The influences of the other features within the seismic feature space cause the differences between single feature classes, like $vs_{1,2}^{v.h.}$, within the Kohonen lattice. As stated above, the seismic feature space is a function of the geological feature space. The geology might be responsible for the class distributions i.e. for the two areas at the lattice node (1,10) (945 - 956 m in figure 4.10) and 10,2 (2377 - 2382 m). The measurements between 945 - 956 m were performed within a disturbed zone in front of an approx. 10 m thick cataclastic zone with $6 \leq s_t \leq 10$ cm ("low"). The seismic profile between 2377 - 2382 m crossed an approx. 30 cm thick cataclastic zone with $s_t=1$ cm ("very low"). The seismic feature maps in figure 4.7 detected both fractured rock mass regions and indicate, that both regions with the same $vs_{1,2}^{v.l.}$ -classes are seismically different. The reason can be seen that the regions underly different histories of formation and hence are characterised by different geological and seismic features.

The ν -feature map shows that the influence of v_S dominates for "very low" v_S -values. The influence of v_P to the ν -values dominates for "high" to "very high" v_P -values. The fracture distance s_t and the existence of water Q can be responsible for the seismic feature vectors. The results confirm the analyses of O'Connell and Budianski (1974) and Henyey and Pomphrey (1982). For dry rock the P-wave velocity decreases more rapidly with the crack density than the S-wave velocity. In contrast, for a completely saturated rock, v_S and v_P decrease uniformly with the crack density, but v_S initially decreases about twice as fast than v_P .

Q_1^l ("wet") corresponds to $\nu^{v.h.}$ and $vs_2^{v.l.}$. The small area Q_2^l is linked to area $S^{v.l.}$. The link is statistically and physically not reliable and hence uncertain. The two areas $Q_{3,4}^l$ are characterised by $vs_1^{v.l.}$ and $vp_{1,2}^{v.l.}$ and by ν_2^h . The feature maps of p and Q in figure 4.8 show physically reliable relationships. High persistent fractures increase the hydraulic conductivity and hence the water flow into the tunnel. The feature maps between p and Q where independently generated by the SOM network.

SOM interpretations based on seismic or geological feature classes are advantageous if relationships between single features are required. For general characteristics about homogeneous rock mass units, SOM interpretations should base on seismic-geological feature clusters. The Kohonen lattice of figure 4.11 shows the rock mass units with their qualitative similarities and differences. These differences can be seen in table 4.1. The similar clusters 1 and 2, which occur along profile 945 - 956 m (see figure 4.10), are different from cluster 9 and partially from cluster 8, which occur along profile 2377 - 2382 m (see figure 4.10). Another example is the difference between cluster 5, which occurs along the profiles 1314 - 1379 m and 1582 - 1663 m (see figure 4.10), and cluster 7, which occurs along profile 2132 - 2205 m (see figure 4.10).

It could be shown, that it is possible to automatically classify engineering geological rock mass properties from in-situ seismic measurements performed during tunnel ex-

cavations. The classifications were performed by a new method, called Self-Organising Maps (SOM). This method is based on neural information processing and is more powerful compared to conventional methods, such as correlations and spatial profile descriptions. The reason is, that all seismic features are jointly used for the classification. Their inter-relationships as well as their relationships to the geological features are visualised in 2-dimensional images. These feature maps can be visually described and easily interpreted. Hence, the overview of all features and all relationships can be retained for the interpretation. Although the geological properties are qualitatively and quantitatively low and the seismic properties are physically and numerically limited, classifications can still be performed, when all seismic properties are used simultaneously. For interpretations of seismic in-situ measurements, the quantity of the involved properties is more important than the quantity and precision of the measurements.

5 Final Conclusions

Geological interpretations of the seismic in-situ measurements in granitic gneisses in southern Switzerland confirm the knowledge about the theoretical relationships between geological and seismic rock mass properties. It is possible to classify engineering geological rock mass properties from in-situ seismic measurements with subject to the following facts: integral character of seismic waves and seismic dependency. The integral character of seismic waves shows that small heterogeneities like single fracture sets can not be imaged in detail, when their extension is smaller than the seismic wave length. The seismic dependency describes that seismic properties dependent on the geology. A logical reasoning from seismic to geological parameters can lead to ambiguous conclusions. For that reason it is necessary to use as much as possible seismic parameters in combination for a classification.

In the first chapter, new seismic parameters are derived from polarisation ellipsoids of leading shear-waves: shape measure S and shape intensity I . The shape measure S is an essential feature that characterises the shape of the polarisation ellipsoids and additionally the geological-physical reason of the polarisation. S shows whether shear-waves are fabric-induced polarised with stretched ellipsoids (orthotropy) or crack induced-polarised with flattened ellipsoids (transverse isotropy). The stretched ellipsoids show in direction to the well oriented minerals in the rock mass. The flattened ellipsoids orient in direction parallel to the cracks and fractures. The variability of crack-induced S_1 -polarisation ellipsoids is much higher than of fabric-induced ellipsoids. The more homogeneous the rock mass occurs the higher is the shape intensity I . I is an indicator for the fracturing of a rock mass region in which the waves propagate. The existence of fractures and cracks disturb the wave motion and hence the intensity of the polarisation ellipsoids.

In the second chapter, the seismic data are interpreted by conventional comparison methods. The seismic feature vectors $\{v_P, v_S, \nu, \xi, S, I\}$ contain the following seismic attributes: compression-wave velocity v_P , velocity of the first shear-wave v_S , Poisson's ratio ν respectively velocity ratio v_P/v_S , shear-wave velocity anisotropy $\xi_{(v_{S_1}, v_{S_2})}$ and the mean values of the shape measure S and shape intensity I of the S_1 -waves polarisation ellipsoids along each seismic profiles. The geological feature vectors $\{\sigma_c, Q, s_t, p, e, r, f, ss\}$ contain the following geological attributes: uniaxial compressional strength σ_c perpendicular to the schistosity, water inflow into the tunnel Q , total fracture spacing s_t , fracture persistence p , fracture aperture e , fracture roughness r , fracture infilling f , and schistosity dip angle ss . The results show that interpretations are possible but partially of poor quality, when seismic and geological properties are compared pairwise. The most correlations between the properties are very weak. Pairwise feature comparisons do not show the total information that can be necessary

for a classification. The measured seismic rock mass properties vary in combination at the same time, when acoustic waves propagate through the interior of the rock mass. Hence, the seismic interpretation should base on all properties. For that reason, the third chapter describes a new classification method, called self-organising maps (SOM), that images the seismic and geological relationships in 2-dimensional images. The images, called feature maps, give an overview about all features and all relationships. They can be visually described and easily interpreted. SOM-classification considers at each time the interdependencies between all seismic features. The quality of the classification results are higher compared to conventional methods. Hence, the feature maps show those different property states, which normally lead to ambiguous seismic interpretations.

The classifications show the following results briefly. v_S is the most robust seismic parameter to characterise the fracture spacing, especially when the rock mass is "wet". The importance of v_P to characterise the rock mass fracturing increases when the rock mass gets "dry". It could be qualitatively shown that fracturing and water influence the shear-wave anisotropy ξ and the Poisson's ratio ν . "Dry" low fractured rock mass shows medium ξ and ν -values, whereas "dry" high fractured rock mass shows high ξ and low ν -values. In "wet" rock mass ξ is low and ν -values are high. A SOM neural network is advantageous, because it is an automatic interpretation system that can be used for online classifications, when seismic in-situ measurements are performed during the tunnel excavation.

Two research projects are being prepared. In the first project, finite difference modelling based on seismic wave propagation should show the theoretical evidence for the correctness of the new ellipsoid shape parameters S and I . In the second study, the SOM "expert system" should be used for classifications during the excavation of the Gotthard Base Tunnel. The neural network has to be validated in unknown rock mass regions along the tunnel and the automatism should be modified to support decisions during tunnel excavation.

6 References

- Anderberg, M. R., 1973. Cluster analysis for applications, Academic Press, New York.
- Barruol, D., Mainprice, H., Kent, D., de Saint Blanquat, M., and Compté, P., 1992. 3D seismic study of a ductile shear zone from laboratory and petrofabric data (Saint Barthémély Massif, Northern Pyrénées, France). *Terra Nova*, 4, 63-76.
- Barton C. A. and Zoback M. D., 1992. Self-similar distribution and properties of macroscopic fractures at depth in crystalline rock in the Cajon Pass scientific drill hole, *J. Geophys. Res.*, 97, 5181-5200.
- Bieniawski, Z. T., 1989. Engineering rock mass classification, Wiley, New York, 251pp.
- Bishop, C. M., 1995. Neural Networks for Pattern Recognition. Oxford University Press, Oxford.
- Boadu, F.K., 1997. Relating the Hydraulic Properties of a Fractured Rock Mass to the Seismic Attributes: Theory and Numerical Experiments. *Int. J. Rock. Mech. Science*, 34(6), pp885-895.
- Borm, G., Giese, R., Otto, P., Dickmann, Th., and Amberg, F., 2001. Integrated Seismic Imaging System for geological prediction ahead in underground construction, Rapid Excavation and Tunneling Conference (RETC), 11. - 13. June, San Diego USA.
- Bossart, P., Meier, P.M., Moeri, A., Trick, T., Mayor, J-C., 2002. Geological and hydraulic characterisation of the excavation disturbed zone in the Opalinus Clay of the Mont Terri Rock Laboratory, *Engineering Geology*, 66, pp19-38.
- Buhmann J., 1998. Empirical Risk Approximation: An Induction Principle for Unsupervised Learning. Institut für Informatik III, University of Bonn, IAI-TR-98-3.
- Caine, J. S., Evans, J. P., and Forster, C. B., 1996. Fault zone architecture and permeability structure, *Geology*, 24 (11), 1025-1028.
- Casasopra, S., 1939. Studio petrografico dello gneis granitico Leventina, Valle Riviera e Valle Leventina (Canton Ticino). *Schweiz. Mineral. Petrogr. Mitt.*, Vol. 19, pp. 449-717.
- Christensen, N., 1966. Shear wave velocities in metamorphic rocks at pressures to 10 kilobars. *J. Geophys. Res.*, 71(14), 3549-3556.
- Christensen, N., 1971. Shear wave propagation in rocks. *Nature*, 229, 549-550.
- Cliet, C. and Dubesset, M., 1988. Polarization analysis in three-component seismics, *Geophysical Transactions*, 34(1), 101-119.
- Chester, F. M. and Logan, J. M., 1986. Implication for mechanical properties of brittle faults from observations of the Punchbowl fault zone, California, *Pure and Appl. Geophys.*, 124, 79-106.
- Chester, F. M. and Logan, J. M., 1987. Composite planar fabric of gouge from the Punchbowl fault, California, *J. Structural Geol.*, 9, 621-634.

- Crampin, S., 1981. A review of wave motion in anisotropic and cracked elastic-media, *Geophysics, Wave Motion*, 3, 343-391.
- Crampin, S., 1985. Evaluation of anisotropy by shear-wave splitting, *J. Geophys. Res.*, 95, 11143-11150.
- Crampin, S., 1987. Geological and industrial implications of extensive dilatancy anisotropy, *Nature* 328, 491-496.
- Crampin, S., 1989. Suggestions for a consistent terminology for seismic anisotropy, *Geophysical Prospecting*, 37, 753-770.
- Crampin, S., 1990. The scattering of shear waves in the crust, *Pure Appl. Geophys.*, 132, 67-91, 1990.
- Darot, M. and Bouchez, J. L., 1976. Study of directional data distributions from principal preferred orientation axes, *Jour. Geol.* 84 (2), pp. 239-247.
- Dershowitz, W., Busse, R., Geier, J., Uchida, M., 1996. A stochastic approach for fracture set definition. In: Aubertin, M., Hassani. F., Mitri, H., (eds.), *Proc., 2nd NARMS, Rock Mechanics Tools and Techniques*, Montreal, Balkema, Rotterdam, pp. 1809-1813.
- Duda, R. O. and Hart, P. E., 2000. *Pattern classification and scene analysis*. Wiley, New York.
- Emsley, S.J., Olsson, O., Stanfors, R., Stenberg, L., Cosma, C., Tunbridge, L., 1996. Integrated characterisation of rock volume at Äspö HRL utilised for EDZ experiment. In: Barla, G. (ed.), *Eurock '96*, Balkema, Rotterdam, pp1329-1336.
- Ettner, U., 1999. Die Strukturgeologie des Gebietes Lukmanierpass - Piora - Leventina, In: Loew, S. and Wyss, R., (Eds), *Vorerkundung und Prognose der Basistunnels am Gotthard und am Lötschberg*, Balkema, Rotterdam. 404pp.
- Fisher, N. I., Lewis, T., and Embleton, B. J., 1987. *Statistical analysis of spherical data*, Cambridge University Press, New York.
- Fukunaga, K., 1990. *Introduction to statistical pattern recognition*, 2nd ed, Academic Press, Boston.
- Garbin, H.D. and Knopoff, L., 1973. The Compressional Modulus of a Material Permeated by a Random Distribution of Circular Cracks. *Quart. Appl. Math.*, 30, 453-464.
- Garbin, H.D. and Knopoff, L., 1975. The Shear Modulus of a Material Permeated by a Random Distribution of Free Circular Cracks. *Quart. Appl. Math.*, 33, 296-300.
- Giese, R., Klose, C.D., Otto, P., Selke, C. and Borm, G., 2003. In situ seismic investigations of fault zones in the Leventina Gneiss Complex of Swiss Central Alps, (submitted and accepted, *Journal of the Geological Society (UK)*).
- Gray, R.M., 1984. Vector Quantization, *IEEE ASSP*. 1 (2), pp. 4-29.
- Gray, R.M., 1990. *Entropy and Information Theory*, New York, Springer.
- Greenhalgh, S.A., Manson, I.M., and Sinadinovski, C., 2000. In-mine seismic delineation of mineralization and rock structure. *Geophysics*, 65(6), pp1908-1919.
- Hammah, R. E., Curran, J. H., 1998. Fuzzy cluster algorithm for the automatic delineation of joint sets. *Int. J. Rock Mech. Min. Sci.* 35 (7), pp. 889-905.
- Henye, T.H. and Pomphrey, R.J., 1982. Self-consistent moduli of a cracked soil. *Geophys. Res. Lett.* 9, 903-906.
- Hoagland, R.G., Hahn, G.T., and Rosenfield, A.R., 1973. Influence of micorstructure on fracture propagation in rock, *Rock Mechanics*, 5, 77-106.
- Hudson, J.A., 1981. Wave speeds and attenuation of elastic waves in material

- containing cracks, *Geophys. J. R. astr. Soc.*, 64, 133-150.
- Ji, S. and Salisbury, M., 1993. Shear-wave velocities, anisotropy and splitting in high-grade mylonites, *Tectonophysics*, 221, 453-473.
- Kaufman, L. and Rousseeuw, P.J., 1990. Finding groups in data: An introduction to cluster analysis. John Wiley & Sons Inc., New York, pp.340.
- Kern, H. and Wenk, H. R., 1990. Fabric-related velocity anisotropy and shear wave splitting in rocks from the Santa Rosa mylonite zone, California. *J. Geophys. Res.*, 95(B7), 11213-11223.
- Kiraly, L., 1969. Statistical analysis (orientation and density), *Geol. Rundschau* 59 (1), pp. 125-151.
- Kohonen, T., 2001. Self-Organizing Maps. Springer, Berlin, pp.501
- Kuwahara, Y., Ito, H., Ohminato, T., Nakao, S., and Kiguchi T., 1995. Size characterization of in situ fractures by high frequency s-wave vertical seismic profiling (VSP) and Borehole logging, *Geotherm. Sci. & Tech.*, vol. 5, 71-78.
- Lange T. Braun M. Roth V. and Buhmann J., 2003. Stability-Based Model Selection. In: NIPS. 15. in press.
- LeCun, Y., 1993. Effective Learning and Second-order Methods, A Tutorial at NIPS 93. Denver.
- Marshall, P., Fein, E., Kull, H., Lanyon, W., Liedtke, L., Müller-Lyda, I., Shao, H., 1999. Conclusions of the tunnel near-field programme. Nagra Technical Report 99-07, Nagra, Baden, Switzerland.
- Mooney, W.D. and Ginzburg, A., 1986, Seismic Measurements of the Internal Properties of Fault Zones. *PAGEOPH*, 124(12), 141-157.
- Moos, D., Zoback, M. D., 1983. In situ studies of velocity in fractured crystalline rocks, *Journal of Geophysical Research*, 88 (B3), 2345-2358.
- O'Connell, R. J. and Budiansky, B., 1974. Seismic velocities in dry and saturated cracked solids, *Journal of Geophysical Research*, 79 (35), 5412-5426.
- Passchier, C.W., Trouw, R.A.J., 1996. *Microtectonics*, Berlin, 289pp.
- Pecher A., 1989. SchmidtMac - A program to display and analyze directional data, *Computers & Geosciences*. 15 (8), 1315-1326.
- Pettke, T. and Klaper, E., 1992. Zur Petrographie und Deformationsgeschichte des südöstlichen Gotthardmassivs. *Schweizer mineral. petrogr. Mitt.*, 72, 197-211.
- Priest S. D., 1994. *Discontinuity Analysis for Rock Engineering*. Chapman & Hall.
- Rabbal, W., 1994. Seismic anisotropy at the Continental Deep Drilling Site (Germany), *Tectonophysics*, 232, 329-341.
- Ripley B.D., 1996. *Pattern recognition and neural networks*. Cambridge University Press.
- Robbins, H. and Monro, S., 1951. A stochastic approximation method, *Ann. Math. Stat.*, vol. 22, pp. 400-407.
- Rousseeuw, P.J., 1987. Silhouettes: a Graphical Aid to the Interpretation and Validation of Cluster Analysis, *Journal of Computational and Applied Mathematics*, 20, 53-65.
- Samson, J.C., 1973. Description of the polarization states of vector processes: Application of ULF magnetic fields. *Geophys. J. R. Astr. Soc.*, 34(4), 403-419.

- Samson, J.C., 1977. Matrix and Stokes vector representation of detectors for polarized waveforms: theory, with some applications to teleseismic waves. *Geophys. J. R. Astr. Soc.*, 55, 583-603.
- Scheidegger A.E., 1965. On the statistics of the orientation of bedding planes, grain axes and similar geological data, U.S. Geol. Survey Prof. Paper. 525-C.
- Schneider, T.R., 1993. Schweizerische Bundesbahn, Bauabteilung der Generaldirektion, Gotthard-Basistunnel: Auswertung der Detailkartierungen 1991/1992. Bericht 425aa.
- Schneider, T.R., 1997. Schweizerische Bundesbahn, Bauabteilung der Generaldirektion, Gotthard-Basistunnel - Sondiersystem Piora-Mulde: Schlussbericht Sondierstollen Piora-Mulde, Phase 1, Geologie/Geotechnik/Hydrogeologie/Geothermie. Bericht 425cs.
- Schmidt, W., 1925. Gefügestatistik, *Tschermaks Mineral. Petrol. Mitt.* 38, pp. 392-423.
- Schulz, S. E. and Evans, J. P., 2000. Mesoscopic structure of Punchbowl fault, southern California and geologic and geophysical structure of active strike slip faults, *J. of Struct. Geol.*, 22, 913-930.
- Shanley, R. J. and Mahtab M. A., 1976. Delineation and analysis of clusters in orientation data, *Mathematical Geology* 8 (1), pp. 9 - 23.
- Shannon, C.E., 1948. A mathematical theory of communication. *Bell System Technical Journal*, vol. 27, pp. 379-423, 623-656.
- Silverman, B.W., 1986. *Density Estimation*, London, 175pp.
- Sjögren, B., Ofsthus, A., Sandberg, J., 1979. Seismic classification of rock mass qualities. *Geophys. Prospect.*, 27, 409-442.
- Stierman, D. J., 1984. Geophysical and geological evidence for fracturing, water circulation and chemical alteration in granitic rocks adjacent to major strike slip faults, *Journal of Geophysical Research*, 89 (B7), 5849-5857.
- Wallbrecher E., 1978. Ein Cluster-Verfahren zur richtungsstatistischen Analyse tektonischer Daten, *Geologische Rundschau*. 67 (3), 840-857.
- Whittaker, B.N., Sigh, R.N. and Sun, G., 1992. *Rock Fracture Mechanics*. Elsevier, Amsterdam, 570pp.
- Wright, C., Walls, E.J., and de J. Carneiro, D., 2000. The seismic velocity distribution in the vicinity of a mine tunnel at Thabazimbi, South Africa. *Journal of Applied Geophysics*, 44, 369-382.
- Zangerl, C., Eberhardt, E., Loew, S., 2001. Analysis of ground settlement above tunnels in fractured crystalline rocks. *Proc. of the ISRM Regional Symposium Eurock, Espoo*, pp 717-722.
- Zappone, A., Sciesa, E., Rutter, E. H., 1996. Caratterizzazione sperimentale dei parametri elastici dello Gneiss granitico Lenventina (Canton Ticino, Svizzera), *Geologia Insubrica*, vol. 1, 1-2.
- Zell, A., Mamier, G., Vogt, M., Mache, N., Hübner, R., Döring, S., Herrmann, K.-U., Soyez, T., Schmalzl, M., Sommer, T., Hatzigeorgiou, A., Posselt, D., Schreiner, T., Kett, B., Clemente, G., Wieland, J., Gatter, J., 1998: SNNS - Stuttgart Neural Network Simulator User Manual, Version 4.2. University of Stuttgart, Institute for Parallel And Distributed High Performance Systems University of Tübingen, Wilhelm Schickard Institute for Computer Science. <http://www-ra.informatik.uni-tuebingen.de/SNNS/>.

A A New Clustering Method for Partitioning Directional Data

Ein Mangel an Phantasie
bedeutet den Tod der
Wissenschaft.

(Johannes Kepler)

Klose, C.⁽¹⁾, Seo, S.⁽²⁾, Obermayer, K.⁽²⁾

⁽¹⁾ GFZ Potsdam, Geoengineering, Telegrafenberg, 14473 Potsdam, Germany

⁽²⁾ Electrical Engineering and Computer Science, Technical University of Berlin, FR 2-1, Franklinstr. 28/29, 10587 Berlin, Germany

Article submitted to
International Journal of Rock Mechanics and Mining Sciences

A.1 Abstract

We present a new clustering method for the partitioning of directional data which is based on vector quantization. Directional data are grouped into disjunct clusters and - at the same time - the average dip direction and the average dip angle are calculated for each group. Grouping is achieved by minimizing the average distance between the data points and the average values which characterize the cluster to which the data points belong to. The distance between directional data is measured by the arc length between the corresponding poles on the unit sphere. The new algorithm is fast and compares well with the expert-supervised grouping method developed by Pecher. No heuristics is being used, because the grouping of data points, the assignment of new data points to clusters, and the calculation of the average cluster values are based on the same, intuitive cost function. Furthermore, the new method minimizes manual interactions and does not require the calculation of a contour density plot.

A.2 Introduction

Classification respectively clustering problems of directional data are fundamental problems in all geological disciplines. Fracture analysis in applied geology and geomechanics, strain and stress analysis in structural geology and seismology, or spatial classifications in geomonitoring are only some examples. Geologists measure and analyze directional data in rocks or sediments and try to cluster the orientations of the structural elements, i.e. fractures, into homogeneous subgroups as good as possible. At this stage, clustering methods (Ripley, 1996) can be of an essential help.

Several methods have been proposed to help geologists finding groups of directional data. Counting methods for visually partitioning the orientation data in stereographic plots were already introduced by (Schmidt, 1925). First a kernel density estimate (Duda and Hart, 2000) of the density of directional data is constructed for every dip direction and angle by counting the number of data points which fall into a small circle around every value. Then a contour density plot is computed and its maxima are interpreted as the parameters of potential subsets measured from the noisy data.

If measurements of example fractures can only be done in one dimension (borehole, scanline) or two dimensions (sampling windows), however, values for dip angle and dip direction of fractures which correspond almost parallel to the dimension directions occur much less frequent. This sampling bias leads to a strongly varying density in the stereographic plot and may make it necessary to adjust the radius of the circles or to weight the values with a heuristic factor in order to obtain a good density estimate (Priest, 1994).

Shanley and Mathab (1976) and Wallbrecher (1978) developed different counting techniques to identify clusters of orientation data. The parameters of the counting methods have to be optimized by comparing the clustering result with a given probability distribution on the sphere in order to obtain a good partitioning result. Counting methods, however, depend strongly on the density of data points and their results are

prone to the aforementioned sampling bias. In addition, counting methods are time-consuming, may lead to incorrect results for clusters with a large dip angle, and may lead to solutions which an expert would rate suboptimal.

More recently, Pecher (1989) developed an expert-supervised method for the grouping of directional data distributions, which is now widely used. First, a contour density plot is calculated, for example by the counting method. Then an observer picks initial values for the average dip directions and dip angles of one to a maximum of seven clusters. The initial guesses are then refined using the fitting method for cluster and griddle distributions derived by Kiraly (1969) and Darot and Bouchez (1976). Both methods are based on assigning data points to the clusters using a suitable distance measure followed by a principal component analysis of the orientation matrices (Scheidegger, 1965). The eigenvectors which correspond to the largest eigenvalues (the "principal" eigenvectors) are calculated for every cluster, and their dip directions and dip angles are used to characterize the properties of the clusters. The Pecher method is a preferred grouping technique and provides excellent results. However, it has the conceptual disadvantage, that it uses two different distance measures, one measure for the assignment of data points to clusters (sometimes this assignment is performed manually) and another measure to calculate the refined values for dip direction and dip angle. Therefore, average values and cluster assignments are not determined in a self-consistent way.

Dershowitz et al. (1996) developed a partitioning method which is based on an iterative, stochastic reassignment of orientation vectors to clusters. Assignment probabilities are calculated using selected probability distributions on the sphere, which are centered on the average orientation vector characterizing the cluster. The average orientation vector is then re-estimated using principal component analysis of the orientation matrices. Probability distributions on the sphere were developed by several authors and are summarized in Fisher et al. (1987). Hammah and Curran (1998) describe a related approach which is based on fuzzy sets and on a similarity measure $d(\vec{x}, \vec{w}) = 1 - (\vec{x}^T \vec{w})^2$, where \vec{x} is the orientation vector of a data point and \vec{w} is the average orientation vector of the cluster. This similarity measure is normally used for the analysis of orientation data (Anderberg, 1973 and Fisher et al. 1987). Similar to the Pecher method, however, two different distance measures are used, hence average values and cluster assignments are not determined in a self-consistent way either.

In this paper we introduce a clustering method which is based on vector quantization (Gray, 1984), and which improves on several of the abovementioned problems. The quality of a clustering solution is measured by the average distance between data points and the cluster to which they belong, the latter being characterized by its average pole vector. The optimal solution is obtained by minimizing this cost function with respect to both the assignments of data points to clusters and their average pole vectors in a self-consistent way. We suggest the arc length $d(\vec{x}, \vec{w}) = \arccos(|\vec{x}^T \vec{w}|)$ as a distance measure, but other distance measures, for example measures derived from probability distributions on the sphere, may be used as well. The new method has the additional advantages that it is fully automatic, that it does not require the construction of a contour density plot, and that it does not contain additional free parameters which have to be optimized.

The paper is organized as follows. The new method is described in section A.3. In section A.4 we apply the method to data obtained from the Gotthard area in Switzerland (Zangerl et al., 2001) and compare it to the results obtained with the Pecher method. Section A.5 ends with a brief conclusion.

A.3 Clustering of Directional Data

Geologists record the dip direction α and the dip angle θ of linear or planar structures in order to determine their spatial orientation. Usually, dip angle and dip direction are measured in degrees ($^\circ$), where $0^\circ \leq \alpha \leq 360^\circ$ and $0^\circ \leq \theta \leq 90^\circ$. A linear structure (axis of a fold, direction of stress or strain) is directly described by a normalized orientation vector, whereas a planar structure (surface like a fracture) is described by its normal vector that is normalized as well. For both, linear structures and normal vectors of planar structures, "pole vectors" $\vec{\Theta} = (\alpha, \theta)^T$ can be defined, which are then used for further analyses. By convention, pole vectors point towards the lower hemisphere of the unit sphere (figure A.1). The orientation $\vec{\Theta}^A = (\alpha^A, \theta^A)^T$ of a pole vector A can be described by its Cartesian coordinates $\vec{x}^A = (x_1, x_2, x_3)^T$ as well (figure A.1), where

$$\begin{aligned} x_1 &= \cos(\alpha) \cos(\theta) && \text{North direction} \\ x_2 &= \sin(\alpha) \cos(\theta) && \text{East direction} \\ x_3 &= \sin(\theta) && \text{downward.} \end{aligned} \tag{A.1}$$

The projections A' of the endpoints A of the pole vectors onto the x_1 - x_2 plane is called a stereographic plot (figure A.1) and is commonly used for visualisation.

A.3.1 Derivation of the Clustering Method

We now consider a set of N pole vectors \vec{x}_k , $k = 1, \dots, N$ whose components are given by eq. (A.1). These pole vectors correspond to N noisy measurements taken from M orientation discontinuities whose spatial orientations are described by their (yet unknown) average pole vectors \vec{w}_l , $l = 1, \dots, M$. For every partition l of the orientation data, there exists one average pole vector \vec{w}_l . The dissimilarity between a data point \vec{x}_k and an average pole vector \vec{w}_l is denoted by $d(\vec{x}_k, \vec{w}_l)$.

We now describe the assignment of a pole vector \vec{x}_k to a partition, i.e. a potential orientation discontinuity, by the binary assignment variables

$$m_{lk} = \begin{cases} 1, & \text{if data point } k \text{ belongs to cluster } l \\ 0, & \text{otherwise.} \end{cases} \tag{A.2}$$

Here we assume, that one data point \vec{x}_k belongs to only one orientation discontinuity \vec{w}_l . The average dissimilarity between the data points and the pole vectors of the

directional data they belong to is given by

$$E = \frac{1}{N} \sum_{k=1}^N \sum_{l=1}^M m_{lk} d(\vec{x}_k, \vec{w}_l), \quad (\text{A.3})$$

from which we calculate the optimal partition by minimizing the cost function E , i.e.

$$E \stackrel{!}{=} \min_{\{m_{lk}\}, \{\vec{w}_l\}}. \quad (\text{A.4})$$

Minimization is performed iteratively in two steps. In the first step, the cost function E is minimized w.r.t. the assignment variables $\{m_{lk}\}$ using

$$m_{lk} = \begin{cases} 1, & \text{if } l = \arg \min_q d(\vec{x}_k, \vec{w}_q) \\ 0, & \text{else.} \end{cases} \quad (\text{A.5})$$

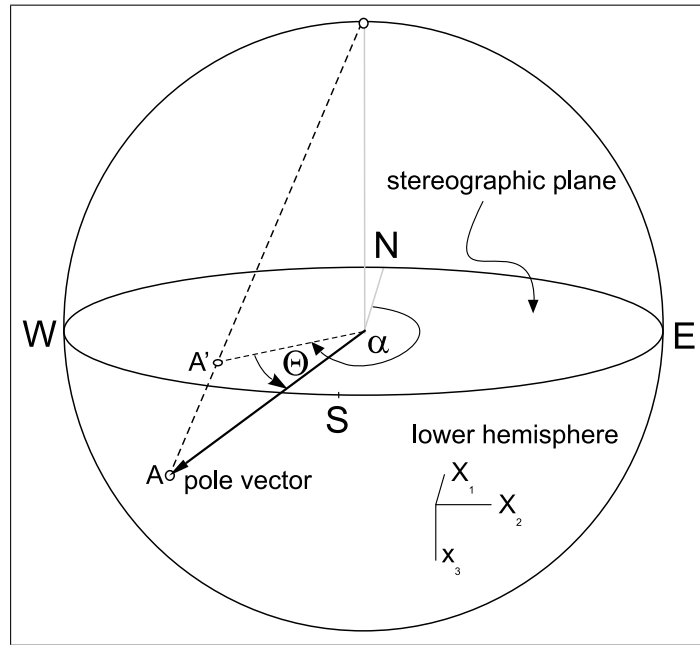


Figure A.1: The orientation of a fracture is measured by its dip angle θ and its dip direction α , and the data is summarized by a vector of unit length which is normal to the fracture plane (solid arrow pointing to point A on the unit sphere). The vector is called pole vector and points to the lower hemisphere by convention. In order to visualize the fracture data, a line is drawn between the tip A of the pole vector (Cartesian coordinates (x_1, x_2, x_3)) and the upper pole of the unit sphere. The point A' , where this line intersects the horizontal plane is marked. The marked plane is used for visualisation and is called stereographic plot. N , E , S and W denote North, East, South and West.

In the second step, cost E is minimized w.r.t. the angles $\vec{\Theta}_l = (\alpha_l, \theta_l)^T$ which describe the average pole vectors \vec{w}_l (see eq. (A.1)). This is done by evaluating the expression

$$\frac{\partial E}{\partial \vec{\Theta}_l} = \vec{0}, \quad (\text{A.6})$$

where $\vec{0}$ is a zero vector with respect to $\vec{\Theta}_l = (\alpha_l, \theta_l)^T$. This iterative procedure is called batch learning and converges to a minimum of the cost because E can never increase and is bounded from below. In most cases, however, a stochastic learning procedure called on-line learning is used which is more robust:

BEGIN Loop

Select a data point \vec{x}_k .

Assign data point \vec{x}_k to cluster l by:

$$l = \arg \min_q d(\vec{x}_k, \vec{w}_q) \quad (\text{A.7})$$

Change the average pole vector of this cluster by:

$$\Delta \vec{\Theta}_l = -\gamma \frac{\partial d(\vec{x}_k, \vec{w}_l(\vec{\Theta}_l))}{\partial \vec{\Theta}_l} \quad (\text{A.8})$$

END Loop

The learning rate γ should decrease with iteration number t , such that the conditions (Robbins and Monro, 1951, Fukunaga, 1990)

$$\sum_{t=1}^{\infty} \gamma(t) = \infty, \quad \text{and} \quad \sum_{t=1}^{\infty} \gamma^2(t) < \infty \quad (\text{A.9})$$

are fulfilled.

The geometrical data set should be partitioned in a way, that all average pole vectors point to the lower hemisphere of the unit sphere (see figure A.1). The distance measure $d(\vec{x}, \vec{w})$ between two pole vectors \vec{x} and \vec{w} must then satisfy the following conditions:

1. $d(\vec{x}, \vec{w}) = \min \Leftrightarrow \vec{x}$ and \vec{w} are equally directed parallel vectors, i.e. $\vec{x}^T \vec{w} = 1$.
2. $d(\vec{x}, \vec{w}) = \max \Leftrightarrow \vec{x}$ and \vec{w} are orthogonal vectors, i.e. $\vec{x}^T \vec{w} = 0$.
3. $d(\vec{x}, \vec{w}_1) = d(\vec{x}, \vec{w}_2)$ if \vec{w}_1 and \vec{w}_2 are antiparallel vectors, i.e. $\vec{w}_2 = -\vec{w}_1$.

Here, we propose the arc length between the projection points of the pole vectors on the unit sphere as the distance measure, i.e.

$$d(\vec{x}, \vec{w}) = \arccos(|\vec{x}^T \vec{w}|), \quad (\text{A.10})$$

where $|\cdot|$ denotes the absolute value. We then obtain for the derivative in eq. (A.8)

$$\frac{\partial d(\vec{x}_k, \vec{w}_l)}{\partial \vec{\Theta}_l} = \frac{\partial \arccos(|\vec{x}_k^T \vec{w}_l|)}{\partial \vec{\Theta}_l} = \frac{\text{sign}(\vec{x}_k^T \vec{w}_l)}{\sqrt{1 - (\vec{x}_k^T \vec{w}_l)^2}} \vec{x}_k^T \frac{\partial \vec{w}_l}{\partial \vec{\Theta}_l}, \quad (\text{A.11})$$

where $\frac{\partial \vec{w}_l}{\partial \vec{\Theta}_l}$ is

$$\frac{\partial \vec{w}_l}{\partial \alpha_l} = \begin{pmatrix} -\sin(\alpha_l) \cos(\theta_l) \\ \cos(\alpha_l) \cos(\theta_l) \\ 0 \end{pmatrix} \quad \text{and} \quad \frac{\partial \vec{w}_l}{\partial \theta_l} = \begin{pmatrix} -\cos(\alpha_l) \sin(\theta_l) \\ -\sin(\alpha_l) \sin(\theta_l) \\ \cos(\theta_l) \end{pmatrix}, \quad (\text{A.12})$$

and $\text{sign}(\cdot)$ is the sign function. Due to the binary assignments, only the nearest average pole vector \vec{w}_l from a given data point \vec{x}_k is modified in one iteration. The other average pole vectors remain unchanged, i.e. $\alpha_r(t+1) = \alpha_r(t)$, $\theta_r(t+1) = \theta_r(t)$, $\forall r \neq l$. The learning rule eq. (A.8) becomes:

$$\Delta \alpha_l = -\gamma^* \text{sign}(\vec{x}_k^T \vec{w}_l) \left[\vec{x}_k^T \frac{\partial \vec{w}_l}{\partial \alpha_l} \right], \quad (\text{A.13})$$

$$\Delta \theta_l = -\gamma^* \text{sign}(\vec{x}_k^T \vec{w}_l) \left[\vec{x}_k^T \frac{\partial \vec{w}_l}{\partial \theta_l} \right]. \quad (\text{A.14})$$

l is the index of the nearest prototypes from given data point, and the square root in the denominator of eq. (A.11) has been absorbed into the learning constants,

$$\gamma^* = \gamma / \sqrt{1 - (\vec{x}_k^T \vec{w}_l)^2}, \quad (\text{A.15})$$

because it is equal for $\Delta \alpha_l$ and $\Delta \theta_l$. If the learning constants are scaled, above learning rule corresponds to the learning rule obtained for the distance measure $d(\vec{x}, \vec{w}) = 1 - |\vec{x}^T \vec{w}|$ (see appendix A.6).

A.3.2 Summary of the Clustering Algorithm

Given: Data set $\{\vec{x}_k\}_{k=1}^N$ and number M of clusters $\{\vec{w}_q\}_{q=1}^M$.

Find: Average pole vectors \vec{w}_q , $q = 1, \dots, M$, and binary assignments m_{qk} of data points \vec{x}_k to clusters q , which minimize the average distance between data points and average pole vectors.

Initialize: Dip angles of the pole vectors $\alpha_q(0)$, $\theta_q(0)$, $\forall q = 1, \dots, M$, annealing schedule for learning rate $\gamma(t)$, and maximum number t_F of iterations.

Compute: $\vec{w}_q(0) = \vec{w}_q(\alpha_q(0), \theta_q(0))^T$ according to eq. (A.1).

Set: Iteration number $t = 0$.

Repeat

1. Draw \vec{x}_k randomly from the data set.
2. Compute $d(\vec{x}_k, \vec{w}_q(t)) = \arccos |\vec{x}_k^T \vec{w}_q(t)|$ for all $q = 1, \dots, M$.
3. Find index $l = \arg \min_q d(\vec{x}_k, \vec{w}_q(t))$ of the pole vector $\vec{w}_l(t)$ closest to \vec{x}_k .
4. Compute the parameters $\alpha_l(t+1)$ and $\theta_l(t+1)$ according to eqs. (A.13, A.14).

5. Compute the pole vector $\vec{w}_l(t+1) = \vec{w}_l(\alpha_l(t+1), \theta_l(t+1))$ according to eqs. (A.1).
6. Compute new learning rate $\gamma(t+1)$.
7. $t \leftarrow t+1$.

Until: $t > t_F$.

Project all \vec{w}_q , $q = 1, \dots, M$ to the lower hemisphere (as defined).

If the third component of the pole vectors $(\vec{w}_q)_3 > 0$, then

$$\begin{aligned}\vec{w}_q &= -\vec{w}_q, \\ \theta_q &= -\theta_q, \\ \alpha_q &= \begin{cases} \alpha_q + \pi & \text{if } \alpha_q < \pi \\ 2\pi - \alpha_q & \text{if } \alpha_q \geq \pi. \end{cases}\end{aligned}$$

A.4 Results

We now apply the new method to measurements from the Gotthard area in Switzerland (Zangerl et al., 2001). 1025 fractures were sampled along sampling scanlines and the dip angles and directions are visualized in figure A.2 (A) using a stereographic plot. Figure A.2 (B) shows the corresponding density contour plot, that result from the Fisher function (Fisher et al., 1987) with an extra-fine 1% fractional area of the lower hemisphere. The Fisher function is used as one option in the commercial software "Spheristat", where the Pecher method is implemented for cluster analysis, to fit the contour plot.

The stereographic plot is difficult to interpret, however. The 1025 fractures were sampled along different scanline orientations with directions between NE-SW and SE-NW, i.e. between 45° - 225° and 135° - 315° (see figure A.2 (A)). Fractures that are oriented parallel to the scanlines are under-represented due to the sampling bias, which leads to a low density with no maxima along directions between NE-SW and SE-NW (figure A.2 (B)). Additionally, many measurements were taken from small fractures, which introduces noise in the distribution of the pole vectors and increases variability. Using expert knowledge and information of the fieldwork (Zangerl et al., 2001), six fracture sets were identified in the contour plot of the dataset shown in figure A.2 (B). There are two areas (319/18 and 165/24) where the fracture density is very high and a third and a fourth area (53/2 and 202/4) describe a medium density. A fifth (197/43) and a sixth (270/1) area is characterized by a very low density.

The expert assessments are now compared with the results of our clustering method and the results obtained with the method of Pecher (Pecher, 1989). Six clusters were chosen and the Pecher method was initialized with the values given above. Then the mean orientations were computed using the fitting method derived from Kiraly (1969) and by Darot and Bouchez (1976). The results are summarized in table A.1 and the average pole vectors of the six clusters are shown as open squares in figure A.2 (C). Table A.2 summarizes the results obtained using our clustering method, and

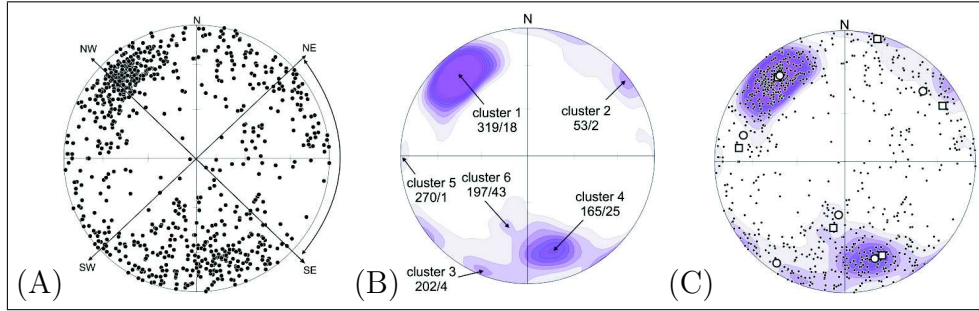
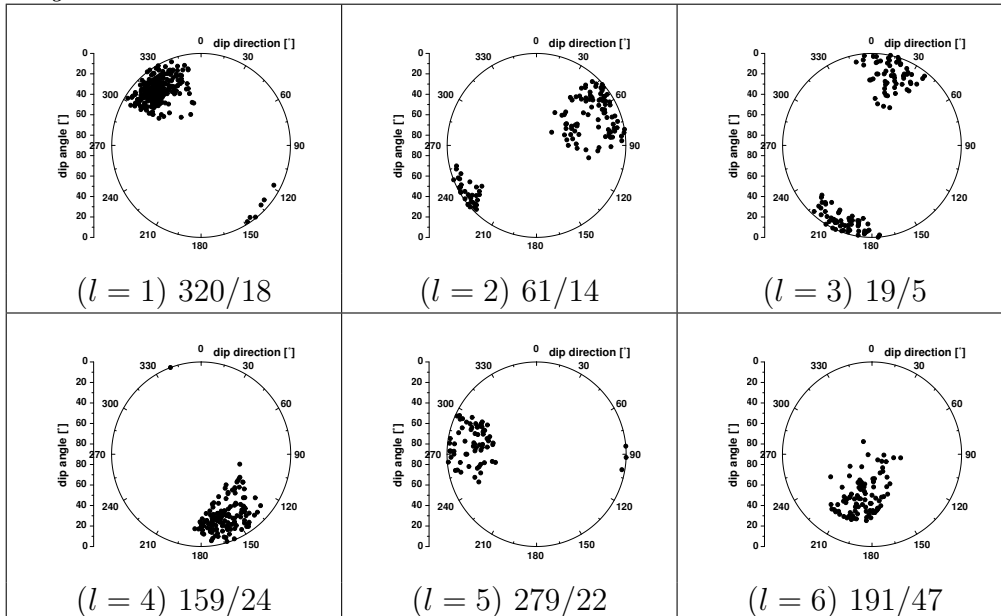


Figure A.2: Fracture pattern of the scanline dataset of Zangerl et al. (2001), which has been collected from the Gotthard area in Switzerland. (A) Visualization of the dataset using a stereographic plot. (B) Contour density plot with the six density maxima marked by arrows. Pairs of numbers denote the average dip direction / dip angle. Darker gray values denote areas of higher probability density. (C) Contour density plot (gray values), overlaid with the data points (small black dots) and the six prototypes, calculated by the Pecher method (open squares, see table A.1) and by our new method described in section A.3 (open circles, see table A.2). N denotes North.

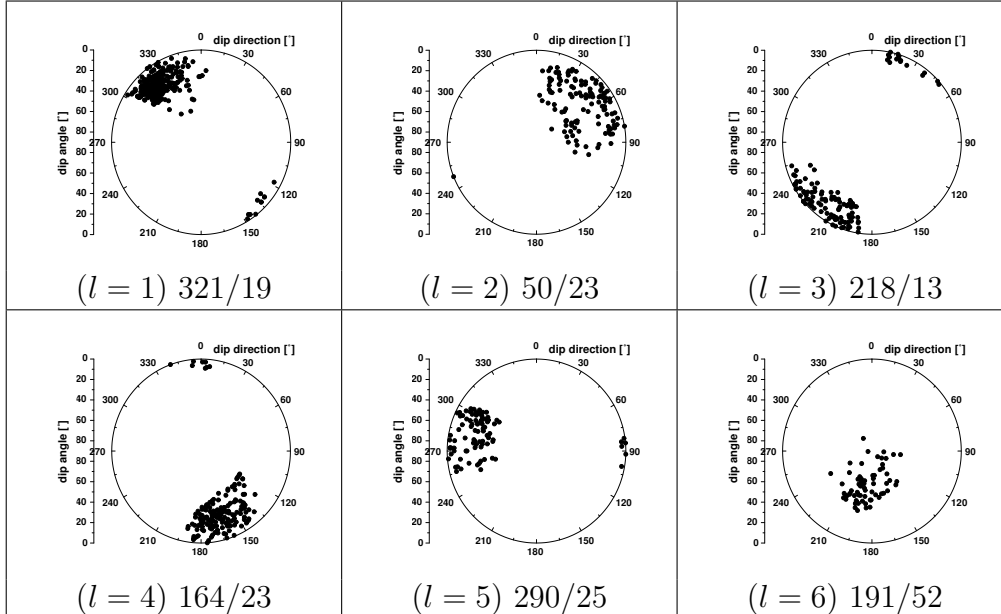
Table A.1: Application of the Pecher grouping method to the scanline dataset of Zangerl et al. (2001). The figure shows the data points (black dots) assigned to the six clusters ($l = 1, \dots, 6$) separately in six stereographic plots. Pairs of numbers denote the average dip direction / dip angle.



the average pole vectors are plotted as open circles in figure A.2 (C). The new method separates all six clusters very well - given the problematic density contour plot. The

average values differ a bit from the maxima of the density especially for fracture sets with medium ($l = 2$ and $l = 3$) or low ($l = 5$ and $l = 6$) densities. This can be explained by the fact, that minimizing the average distance between data points and the mean cluster values is not equivalent to finding the maxima of a kernel density estimate. The results obtained by the new method and the results of the method by Pecher are similar, but the Pecher method requires the construction of a density contour plot which is not necessary for our clustering method. Additionally, a maximum within the density contour plot does not necessarily describes the mean value of the cluster of directional data and a cluster that does not show a density maximum has anyhow a mean value.

Table A.2: Application of the new grouping method described in section A.3 to the scanline dataset of Zangerl et al. (2001). The figure shows the data points (black dots) assigned to the six clusters ($l = 1, \dots, 6$) separately in six stereographic plots. Pairs of numbers denote the average dip direction / dip angle.



A.5 Conclusion

The clustering algorithm outlined in this paper is a new, principled approach for the partitioning of directional data and for the analysis of their average spatial orientation. It is based on the minimization of a cost function, which has an intuitive interpretation, namely the average distance between the data points and the average values which characterize the group they belong to. Here we suggest a distance measure based on the arc length between pole vectors. The method, however, can in principle be extended to other distance measures, to probabilistic assignments, and to grouping problems which involve non-spherical clusters.

The new method leads to results which are similar (though not equal) to the results obtained with the Pecher method (Pecher, 1989) under expert guidance (Zangerl, 2001). The new method, however, is consistent in the determination of clusters and their properties, and it does not require special preprocessing like the construction of a density contour plot. Manual interaction is reduced to the selection of the number of clusters, which - so far - needs to be done by an expert comparing the different clustering results. Automatic methods have been suggested in the clustering literature (Buhmann, 1998, Lange et al., 2003), but whether these methods provide good results for geological data remains to be seen.

A.6 Appendix

The derivative of the distance measure

$$d(\vec{x}, \vec{w}) = 1 - |\vec{x}^T \vec{w}| \quad (\text{A.16})$$

is given by:

$$\frac{\partial 1 - |\vec{x}^T \vec{w}|}{\partial \vec{\Theta}} = -\text{sign}(\vec{x}^T \vec{w}) \frac{\partial(\vec{x}^T \vec{w})}{\partial \vec{\Theta}} = \text{sign}(\vec{x}^T \vec{w}) \vec{x}^T \frac{\partial \vec{w}}{\partial \vec{\Theta}}. \quad (\text{A.17})$$

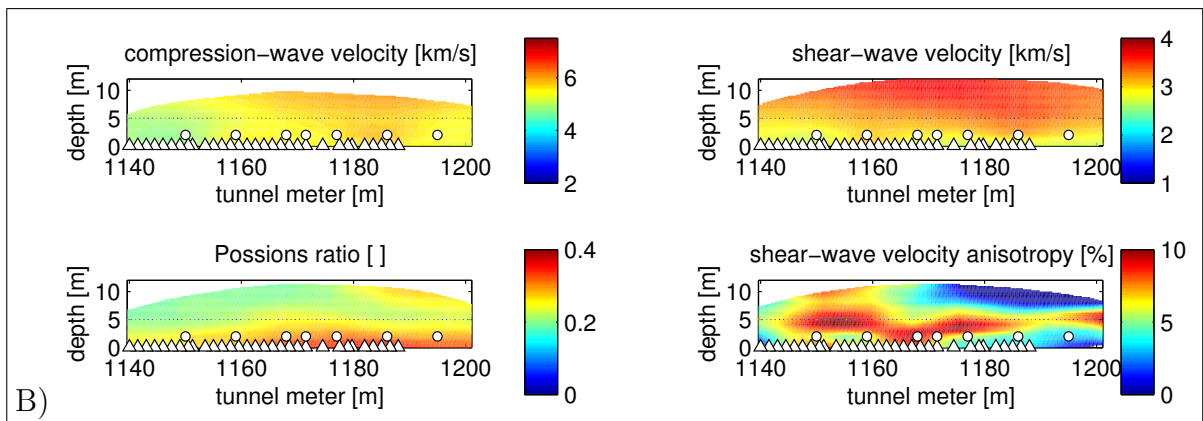
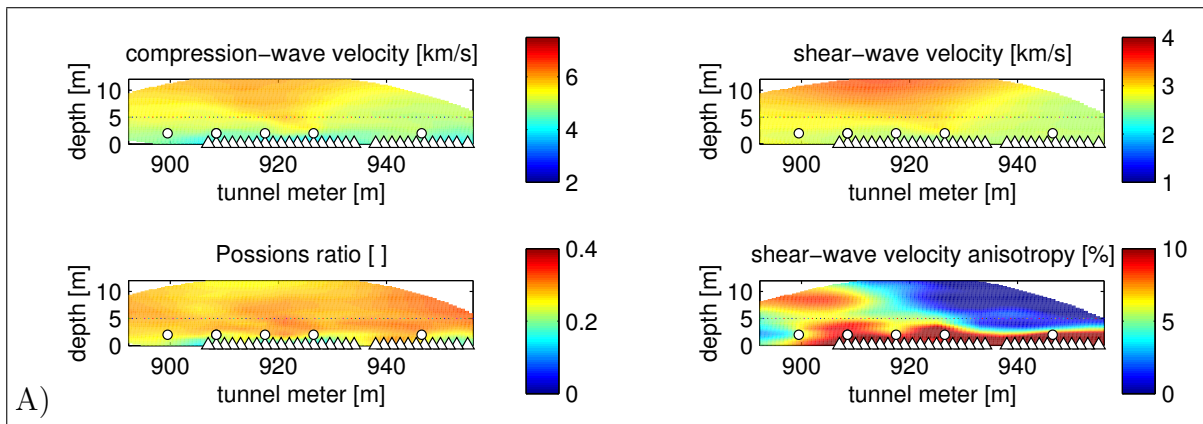
Inserting eq. (A.17) and eqs. (A.12) into eq. (A.8) yields the learning rule eqs. (A.13,A.14).

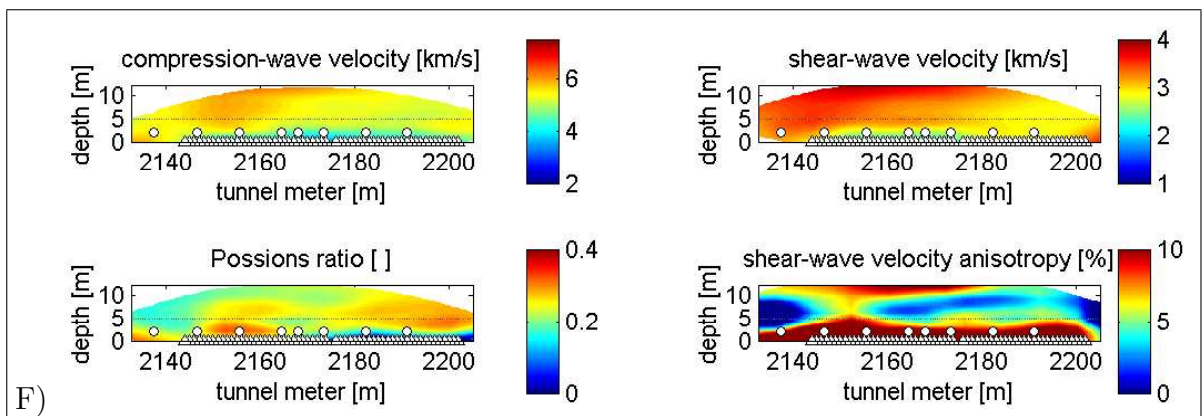
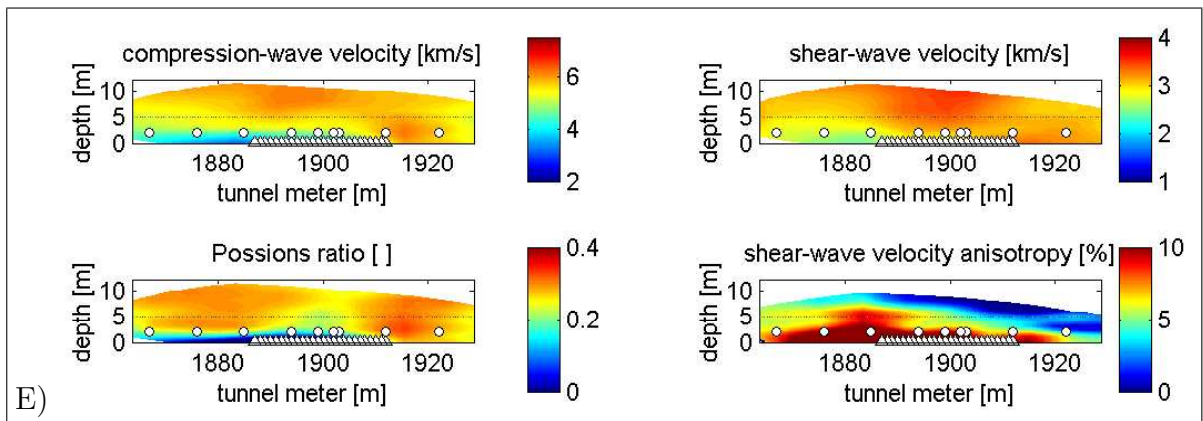
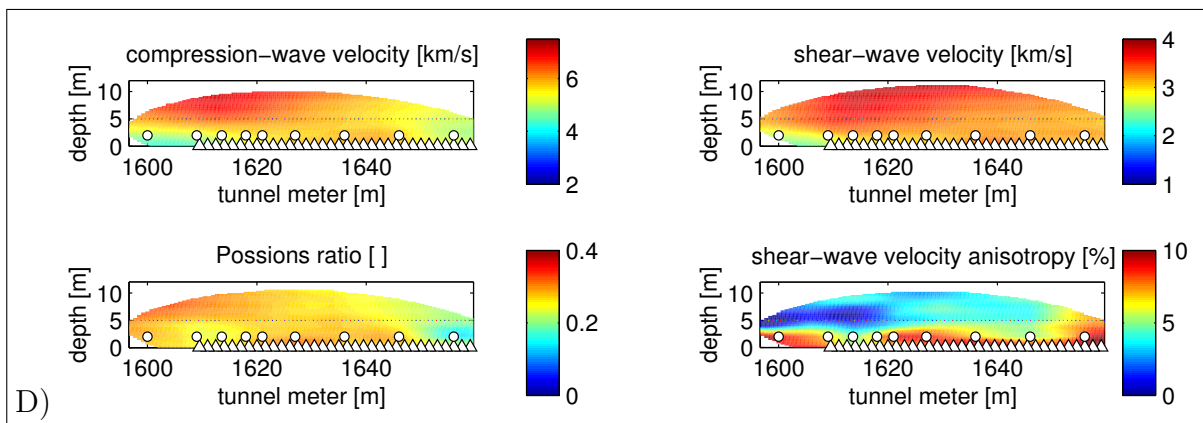
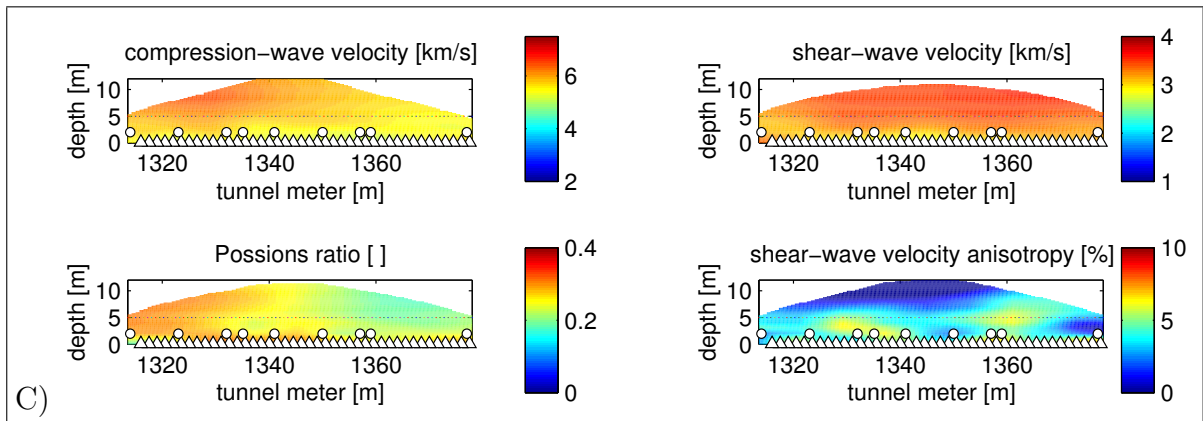
Since the distance measures eqs. (A.10) and (A.16) are both monotonous in $|\vec{x}^T \vec{w}|$ they induce the same partition of directional data for fixed average pole vectors.

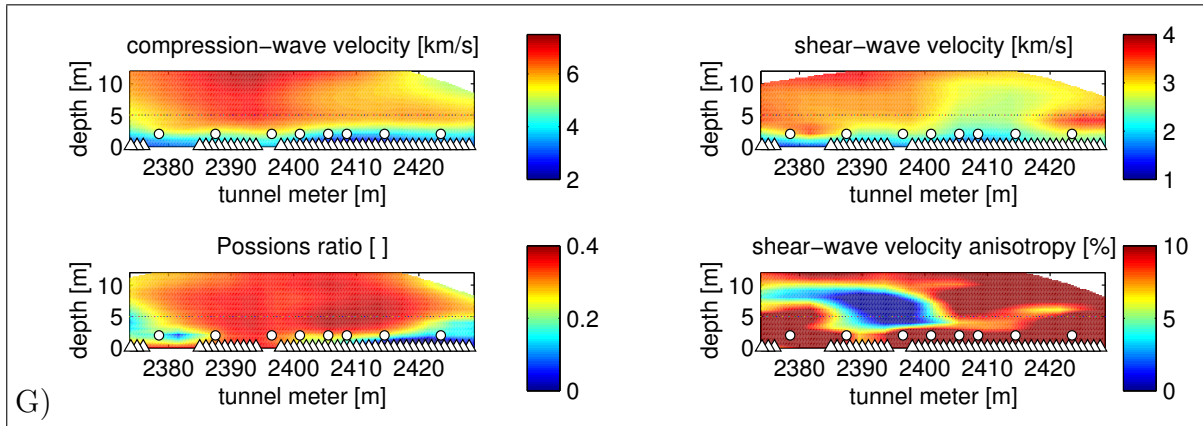
B Seismic Tomograms

This documentation outlines the seismic tomograms of the compression-wave velocity v_P , shear-wave velocity v_S , Poisson's ratio μ and shear-wave velocity anisotropy ξ . The tomograms are shown along the 7 seismic profiles, with source points (white triangles), receiver locations (white circles), and the seismic scanline at 5 m depth to sample the feature vectors for the classification task. The grid size of a tomogram is 50×20 cm.

- A) seismic tomograms at 892-956 m
- B) seismic tomograms at 1140-1201 m
- C) seismic tomograms at 1314-1378 m
- D) seismic tomograms at 1597-1660 m
- E) seismic tomograms at 1864-1929 m
- F) seismic tomograms at 2133-2205 m
- G) seismic tomograms at 2374-2429 m







Curriculum Vitae

Personal Details

Name: Christian Klose
Date of birth: November 4 1974
Place of birth: Quedlinburg, Germany
Nationality: German

Education

1993 - 1999 Studies at the Technical University of Berlin, Germany
1990 - 1993 "Wilhelm von Humboldt" High School, Nordhausen, Germany
1981 - 1990 "Bertolt Brecht" Polytechnical High School, Nordhausen, Germany

Diploma thesis

Development of a fuzzy-rule based expert system for seismic prediction ahead the Piora exploratory tunnel (southern Switzerland).

Diploma mapping

Geological report on Triassic sedimentary rocks and Quarternary sediments to the geological map 1:10'000 Waltershausen (Area 5, northern Thuringia, Germany); generated for the Geological Survey of Thuringia, Germany.